

**Computational Continua for Heterogeneous Solids:
Studies on Unstructured Finite Element Meshes and on Wave
Propagation**

Dimitrios Fafalis

Submitted in partial fulfillment of the
requirements for the degree of
Doctor of Philosophy
in the Graduate School of Arts and Sciences

Columbia University
2017

This page intentionally left blank.

This page intentionally left blank.

ABSTRACT

Computational Continua for Heterogeneous Solids: Studies on Unstructured Finite Element Meshes and on Wave Propagation

Dimitrios Fafalis

The computational continua (C^2) framework, which is the focus of the present thesis, is a coarse-scale continuum description coupled with an underlying fine-scale description of material heterogeneity of finite size. It is intended to account for a variation of the coarse-scale stresses (strains) over a unit cell (UC) domain. It was originally developed to overcome the theoretical and computational limitations of higher order homogenization models and generalized continuum theories, namely the need for higher order finite element continuity, additional degrees-of-freedom, and non-classical boundary conditions. The key feature of the C^2 is so-called nonlocal quadrature scheme (NLQS) defined over a computational continua domain consisting of a disjoint union of so-called *computational unit cells* (CUC). The CUCs, which are merely computational entities, have a shape and size of the physical periodic microstructure, but their positions depend on the size of the unit cell domain and is determined to reproduce the weak form of the governing equations on the fine scale.

In the original C^2 formulation the unit cell domains when mapped onto the parent element domains preserved their original shape. Thus, the nonlocal quadrature scheme was limited to structured meshes or meshes with slightly distorted elements. In the present thesis, it is accounted for that the CUCs when mapped onto the parent element domain, may no longer preserve their initial shape.

Towards this end, an exact nonlocal quadrature scheme for distorted elements, which matches the two-dimensional monomials of the element, and an approximate tensor-product based nonlocal quadrature that eliminates the need for costly evaluation of the quadrature points for each element

were developed. The performance of both nonlocal quadrature schemes is demonstrated in two-dimensional linear elasticity problems on several meshes and microstructures and compared with the classical first-order ($O(1)$) homogenization theory and the direct numerical simulation (DNS). The error in the overall behavior (total strain energy stored and L_2 norm error in von Mises stress) of the C^2 formulations offers a 10-20% improvement over the $O(1)$ theory. More substantial is the gain of the C^2 formulations over the $O(1)$ theory in the accuracy of the local stresses in critical locations. Finally, the performance of the tensor-product based approximate quadrature is comparable to that of the computationally costly exact nonlocal quadrature in terms of both the global and local error measures making it more attractive.

In the wave propagation regime, the computational continua formulation showed strikingly accurate dispersion curves. Unlike classical dispersive methods pioneered more than a half a century ago where the unit cell is quasi-static and provides effective mechanical and dispersive properties to the coarse-scale problem, the dispersive C^2 gives rise to transient problems at all scales and for all microphases involved. An efficient block time-integration scheme is proposed that takes advantage of the fact that the transient unit cell problems are not coupled to each other, but rather to a single coarse-scale finite element they are positioned in. It is showed that the computational cost of the method is comparable to the classical dispersive methods for short load durations. The scheme is proved to be stable. Finally, accuracy analysis on a wave propagation model problem demonstrates that the proposed scheme is substantially more accurate when compared with a $O(1)$ homogenization scheme with microinertia effects.

Contents

List of Tables	iii
List of Figures	v
1 Introduction	1
1.1 Computational continua on unstructured FE meshes	3
1.2 Dispersive computational continua and wave propagation	3
1.3 Thesis outline	6
2 Review of Computational Continua Formulation	9
2.1 The Boundary Value Problem	9
2.2 Additive Decomposition of Solution Fields	12
2.3 The weak form of the coarse-scale problem	13
2.4 The weak form of the fine-scale problem	14
2.5 Discretization of the coarse-scale and fine-scale problems	17
2.5.1 Discrete coarse-scale problem	18
2.5.2 Discrete unit cell problem	19
2.6 Solution of the coupled system	19
3 Computational Continua and Non-local Quadrature Scheme for Unstructured Finite Element Meshes	21
3.1 Introduction	21
3.2 General formulation of nonlocal quadrature scheme	22
3.3 Non-local quadrature for structured meshes	25
3.4 Nonlocal quadrature for unstructured meshes	27
3.5 Approximate tensor-product based NLQS	35

3.6	Nonlocal quadrature for triangular elements	36
3.7	Numerical studies	41
3.7.1	Global error measures	44
3.7.2	Local error measures	49
4	Dispersive Computational Continua and Wave Propagation	63
4.1	Introduction	63
4.2	Dispersive Computational Continua	64
4.2.1	The Initial-Boundary Value Problem	64
4.2.2	The weak form of the coarse-scale problem	66
4.2.3	The weak form of the fine-scale problem	67
4.2.4	Discretization of the coarse-scale and perturbation problems	68
4.3	Solution of the coupled transient-transient system	72
4.3.1	The unit cell problem	73
4.3.2	The coarse-scale problem	75
4.3.3	Computational Cost	78
4.4	Model problem	81
4.4.1	Accuracy studies	81
4.4.2	Stability Analysis	84
5	Conclusion	93
5.1	Scope and contribution of the thesis	93
5.2	Future Work	95
	Bibliography	97

List of Tables

3.1	Monomials for the 2D standard Q8 Serendipity element	28
3.2	Quality measures for Q8 elements	35
3.3	Monomials for the 2D standard T6 element	38
3.4	Relative error in global measures for problem A.	45
3.5	Relative error in global measures for problem B.	46
4.1	Computational cost for scenarios a and b	81
4.2	Material properties and model parameters for model problem	83
4.3	Wave lengths λ , wave numbers k , natural frequencies ω and the wave length to unit cell ratio λ/Θ	83

This page intentionally left blank.

List of Figures

2.1	Composite domain of a model boundary value problem (BVP).	10
2.2	Surrogate computational continua domain.	12
2.3	Periodic unit cell with edges parallel to the global reference axes.	15
3.1	Consecutive isoparametric mappings of computational unit cell (CUC) domain in 2D.	23
3.2	Positions of nonlocal quadrature points in quadratic and cubic 1D elements.	26
3.3	Tensor product rule for rectangular quadrilaterals.	27
3.4	Isoparametric mapping of a general curved-sided 8-node quadrilateral element $Q8$ with the unit cells.	29
3.5	Equivalent rectangular of a general quadrilateral element $Q8$	31
3.6	Incremental transformation of the equivalent rectangular element into the quadrilateral element during the Newton-Raphson solution.	32
3.7	NLQS for a square $Q8$ element.	33
3.8	NLQS for a rectangular $Q8$ element.	33
3.9	NLQS for a rotated rectangular $Q8$ element.	34
3.10	NLQS for a distorted $Q8$ quadrilateral element.	34
3.11	The effect of various quadrilateral quality measures on size ratio reduction factor.	36
3.12	Triangular domain with unit cells.	38
3.13	Geometry of problem A: Perforated dolphin-like plate.	42
3.14	Unit cell mesh used in computational continua and $O(1)$ homogenization for problem A.	43
3.15	Geometry of problem B: plate with a circular hole and continuous fiber microstructure.	43

3.16	Unit cell mesh used in computational continua and $O(1)$ homogenization for problem B.	43
3.17	Coarse-scale Q8 meshes for computational continua and $O(1)$ formulations for problem A.	46
3.18	Coarse-scale Q8 meshes for computational continua and $O(1)$ formulations for problem B.	46
3.19	Location of nonlocal quadrature points for the coarse-scale meshes of problem A.	47
3.20	Location of nonlocal quadrature points for the coarse-scale meshes of problem B.	48
3.21	Total von Mises stress σ_{vM} on DNS cell 1 for problem A.	50
3.22	Total von Mises stress σ_{vM} on DNS cell 2 for problem A.	51
3.23	Total von Mises stress σ_{vM} on DNS cell 3 for problem A.	52
3.24	Total von Mises stress σ_{vM} on DNS cell 4 for problem A.	53
3.25	Total von Mises stress σ_{vM} on DNS cell 5 for problem A.	54
3.26	Total von Mises stress σ_{vM} on DNS cell 1 for problem B.	55
3.27	Total von Mises stress σ_{vM} on DNS cell 2 for problem B.	56
3.28	Total von Mises stress σ_{vM} on DNS cell 3 for problem B.	57
3.29	Total von Mises stress σ_{vM} on DNS cell 4 for problem B.	58
3.30	Total von Mises stress σ_{vM} on DNS cell 5 for problem B.	59
3.31	Displacement contours for problem A.	60
3.32	Displacement contours for problem B.	61
4.1	Sinusoidal pulse excitation of one-dimensional rod.	81
4.2	Geometry configuration of a one-dimensional unit cell with fiber inclusion.	83
4.3	Wave propagation of the model problem at various time instances.	85
4.4	Eigenvalues chart for amplification matrix \mathbf{A} , for the model problem.	88

Acknowledgements

To God, for the Faith, the Hope, the Love ...

To St. Demetrius, for being a sleepless Guard ...

To my family, for their sincere love and support ...

To Mario, for his honest friendship and support ...

To Professor Jacob Fish, for his patience and his unique teaching and mentoring style ...

To Columbia University, for the unprecedented and unrepeatable experience ...

To New York City, for accepting everyone ...

To the USA, for the freedom, the peace, and the greatest opportunities ...

To Life, that has no beginning and no end

This page intentionally left blank.

Chapter 1

Introduction

The [computational continua](#) (C^2) framework [23, 26, 28] is intended to account for a variation of the coarse-scale stresses (strains) over a unit cell (UC) domain. It was originally developed to overcome the theoretical and computational limitations of higher order homogenization models and generalized continuum theories, namely the need for higher order finite element continuity, additional degrees-of-freedom, and non-classical boundary conditions.

Generalized continuum theories introduce either higher order spatial derivatives of the displacement field in what is often referred to as the higher grade continua [18, 31, 46, 50] or additional degrees of freedom (known as the higher order continua) independent of the usual translational degrees of freedom, such as the Cosserat media [11], the micromorphic continua [16], etc. These theories require consideration of higher order boundary conditions due to the introduction of higher order moments and tractions.

Higher order homogenization theories were developed to alleviate the strict limitation of first-order homogenization theory [45, 48, 49, 66] in which the unit cell “sees” a constant macroscopic deformation gradient independent of the unit cell size. As the coarse-scale strain gradients become sufficiently large, the hypothesis of the constant deformation gradient fails to account for the variation of the coarse-scale solution gradients over the unit cell domain. In higher order

theories [29, 30, 41, 56], the unit cell is subjected to non-constant coarse-scale deformation gradients. For instance, in second-order theories, the coarse-scale deformation gradient is assumed to vary linearly over the unit cell domain. However, similarly to the generalized continuum theories, higher order homogenization formulations introduce higher order moments and tractions and require higher order finite element continuity. Rather than having higher order continuity, mixed or multi-field formulations can be employed instead, but computational overhead remains.

The computational continua (C^2) framework, which is the focus of the present thesis, is a coarse-scale continuum description coupled with an underlying fine-scale description of material heterogeneity of finite size. The key feature of the C^2 is so-called *nonlocal quadrature scheme (NLQS)* defined over a computational continua domain consisting of a disjoint union of so-called *computational unit cells (CUC)*. The CUCs, which are merely computational entities, have a shape and size of the physical periodic microstructure, but their positions depend on the size of the unit cell domain and is determined to reproduce the weak form of the governing equations on the fine scale. The disjoint union means that the CUCs may overlap and possibly extend beyond the external boundary of the coarse-scale domain.

Another key feature of the C^2 formulation is an additive decomposition of the tensorial solution fields defined over disjoint union of CUCs. The additive decomposition of tensor fields has been also employed in the Variational Multiscale Method (VMS) [17, 35] and the s-version of the finite element method [22]. However, in both the VMS and the s-version, unit cells are positioned in physical locations of the source fine-scale problem and the additive decomposition of the displacement field is defined over the whole domain.

The present thesis focuses on two topics of the C^2 formulation: (i) the generalization of the NLQS on unstructured finite element (FE) meshes, [20] and (ii) computational aspects of the dispersive C^2 with applications in high frequency wave propagation [19, 21].

1.1 Computational continua on unstructured FE meshes

The **NLQS**, one of the key features of the C^2 formulation, has been generalized to distorted coarse-scale elements on unstructured meshes, [20].

In our previous work [23, 26, 28], the unit cell domains when mapped onto the parent element domains preserved their original shape (rectangular in 2D and cubic in 3D). Thus, the nonlocal quadrature scheme was limited to structured meshes or meshes with slightly distorted elements. In the present thesis, it is accounted for that **CUCs** when mapped onto the parent element domain, may no longer preserve their initial shape.

Solving for the nonlocal quadrature points on large unstructured meshes may require significant computational cost in the preprocessing stage. As a remedy, an approximate nonlocal quadrature scheme based on the tensor product rule of the one-dimensional nonlocal quadrature, similar to rectangular elements [26], is developed for distorted elements. The tensor-product based nonlocal quadrature selects an appropriate size of the equivalent rectangular element based on its quality and the physical size of the unit cell.

1.2 Dispersive computational continua and wave propagation

The second major contribution of the present thesis refers to the dispersive C^2 and its computational aspects on wave propagation, [19].

The problem of wave propagation in a heterogeneous medium is of great interest in both academia and industry. At high frequency excitations when the wavelength is comparable to a heterogeneity size an exotic dynamic response has been observed in various material systems ranging from three-dimensional woven composites to metamaterials. Such a response includes dispersion, dissipation, refraction and reflection of the propagating waves, as they bounce back and forth from

internal material interfaces, as well as a remarkable interplay between nonlinearity and dispersion that may lead to formation of solitons.

These phenomena cannot be captured by classical first-order ($O(1)$) micromechanics [48, 66] theories since micro-structural effects are not taken into account. To resolve or at least to approximate these effects more refined theories have been developed, which from computational point of view, can be classified into the following four main categories:

- a. Transient steady-state (TSS)
- b. Helmholtz Equation (HE)
- c. Transient semi-transient (TST)
- d. Transient transient (TT)

The transient-steady-state (TSS) is a classical approach aimed at studying dispersive wave propagation in a heterogeneous medium. By this approach only the coarse-scale (macro) problem is considered to be transient, whereas the unit cell (or a representative volume element - RVE) problem is approximated as a steady-state problem from where both the overall mechanical and dispersive properties are computed. The effective stiffness theory developed by [3] is one of the first dispersive continuum models falling into the TSS category. Several higher-order homogenization-based theories [4, 6, 7, 33, 52] give also rise to steady-state RVE problem. Various self-consistent schemes developed by [40, 53, 58, 59] fall into this category of methods as well. Methods based on higher-order asymptotic expansion in space and time [9, 24, 25, 27] provide a stabilizing effect on otherwise secular higher-order asymptotic expansions, but give rise to a steady-state unit cell problem. The heterogeneous multiscale method (HMM) [1, 2, 61] has been successfully applied to decompose the wave equation with highly oscillatory coefficients into a steady-state unit cell problem and a transient coarse-scale problem.

Homogenization methods formulated at a fixed frequency for which the balance of linear momentum reduces to the Helmholtz equation [5, 12, 13, 37–39, 55, 62] eliminate the time dependence of unit cell problem giving rise to the solution of the RVE problem in terms of wave traveling frequency. Modal analysis can be subsequently employed to analyze propagation of complex pulse loads. For nonlinear problems, however, modal analysis is no longer trivial and with wide frequency content characteristic to heterogeneous materials, solving directly the space-time multi-scale problem in time domain might be computationally preferential.

Wave propagation in particle-based heterogeneous materials with relatively soft matrices, such as in metamaterials or plastically bonded energetic materials, have for certain wave frequencies unusual properties, such as negative effective mass density [44] or negative effective bulk modulus [14]. For these type of materials, it is critical to resolve transient particle behavior while matrix behavior can be adequately approximated as quasi-static [57]. The coarse-scale first PiolaKirchhoff stress tensor derived by this formulation is similar to the virial formula [10] and [47]. This is not surprising due to the similarity between particles in soft matrix and interacting atoms on one hand, and inertia-free matrix playing the role of interatomic potentials in molecular dynamics on the other hand. It has been shown that this so-called transient-semi-transient (TST) formulation can be derived by introducing additional fast time scale that tracks vibration of particles (or atoms) [8, 9, 29, 42].

There are very few works that fall into the category of fully transient-transient (TT) approaches where initial-boundary value problem is considered at both scales and for each micro-constituent. In the Molecular Dynamics regime an efficient approach was developed by [43, 60] using a space-time integration and complete decoupling of the micro and macro problems. There are two main reasons why this type of methods saw limited popularity in practice, namely:

- Computational complexity. Repeatedly solving time-dependent problem for every unit cell (even for linear solids) is considerably more expensive than precomputing mechanical and

dispersive properties prior to transient coarse-scale analysis.

- Need for generalized continuum, higher order homogenization or nonlocal models to account for microstructures of finite size. Methods, such as the variational multiscale method (VMS) [35] or the multiscale finite element method (MsFEM) [15, 34] possess characteristic length scale as well. While in principle, TT type approaches can be used in the context of infinitesimal unit cells, transient phenomena can be adequately resolved by alternative less computationally demanding methods that, for instance, by precomputing effective dispersive properties.

It has been recently shown that a method possessing the above characteristics coined as the dispersive computational continua (C^2) [21] provides striking accuracy for problems where the wavelength is comparable to the unit cell size. The dispersive curves obtained by the dispersive C^2 formulation have been verified against the classical exact Floquet-Bloch wave solution. The ability of the dispersive C^2 formulation to capture the high frequency dispersive behavior stems from its underlying formulation that is free of scale separation and due to its consideration of fully transient equations at both scales. The computational efficiency of the dispersive variant [21] in comparison to the effective medium theories in the TSS category (see classification above) is the second primary objective of the present thesis, [19].

1.3 Thesis outline

The thesis is organized as follows:

In Chapter 2, the strong and weak form of the BVP and the C^2 formulation is reviewed.

In Chapter 3, the generalization of the nonlocal quadrature to distorted elements and the cost-efficient form of the tensor product based quadrature are presented. The NLQS for the six-node

triangular element is also developed. The chapter concludes with numerical studies on the performance of the C^2 formulation on unstructured finite element meshes.

In Chapter 4, the dispersive C^2 is introduced and the computational aspects are investigated. For the solution of the coupled transient-transient system an efficient block time-integration scheme is proposed. The computational cost of the scheme is analysed along with numerical studies of accuracy and stability of the method.

Finally, in Chapter 5, the conclusions of this thesis, with a summary of the main contributions and a description of future work is presented.

This page intentionally left blank.

Chapter 2

Review of Computational Continua

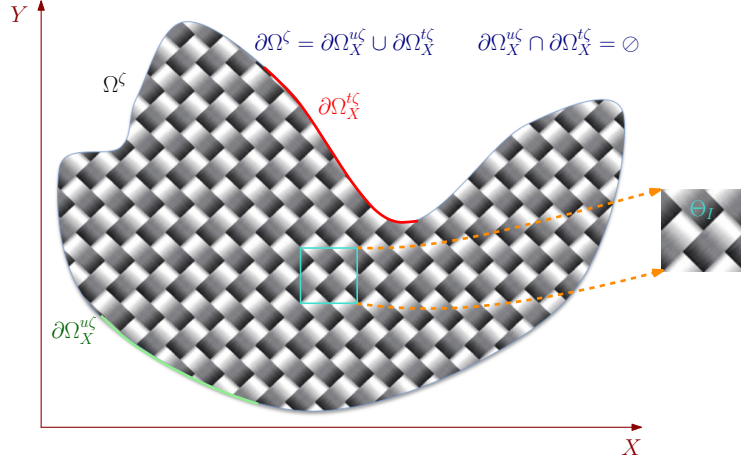
Formulation

2.1 The Boundary Value Problem

Consider a composite domain Ω^ζ with its boundary $\partial\Omega^\zeta$, as shown in Fig. 2.1. The domain is composed by a repetition of a periodic heterogeneous microstructure (or unit cell) (see Fig. 2.1).

The strong form of the **BVP** is stated as follows: Given body force \mathbf{b}^ζ , traction $\bar{\mathbf{T}}^\zeta$ on the Neumann boundary $\partial\Omega_X^{\prime\zeta}$, and prescribed displacement $\bar{\mathbf{u}}_\partial^\zeta$ on the Dirichlet boundary $\partial\Omega_X^{u\zeta}$, find $\mathbf{u}^\zeta : \Omega_X^\zeta \in \mathbb{R}^d, d = \{1, 2, 3\}$ such that:

$$\left\{ \begin{array}{ll} \nabla_{\mathbf{X}} \cdot \boldsymbol{\sigma}^\zeta(\mathbf{X}) + \mathbf{b}^\zeta(\mathbf{X}) = \mathbf{0}, & \text{on } \Omega_X^\zeta \quad (2.1a) \\ \boldsymbol{\varepsilon}^\zeta(\mathbf{X}) = \nabla_{\mathbf{X}}^{\text{Sym}} \mathbf{u}^\zeta(\mathbf{X}), & \text{on } \Omega_X^\zeta \quad (2.1b) \\ \boldsymbol{\sigma}^\zeta(\mathbf{X}) \mathbf{n}^\zeta(\mathbf{X}) = \bar{\mathbf{T}}^\zeta(\mathbf{X}), & \text{on } \partial\Omega_X^{\prime\zeta} \quad (2.1c) \\ \mathbf{u}^\zeta(\mathbf{X}) = \bar{\mathbf{u}}_\partial^\zeta(\mathbf{X}), & \text{on } \partial\Omega_X^{u\zeta} \quad (2.1d) \end{array} \right.$$


 Figure 2.1: Composite domain of a model **BVP** and unit cell Θ .

The weak form of the **BVP** is stated as follows: Given body force \mathbf{b}^ζ , traction $\bar{\mathbf{T}}^\zeta$ on the Neumann boundary $\partial\Omega_X^{t^\zeta}$, and prescribed displacement $\bar{\mathbf{u}}_\partial^\zeta$ on the Dirichlet boundary $\partial\Omega_X^{u^\zeta}$:

Find $\mathbf{u}^\zeta \in W_{\Omega_X^\zeta}$ such that

$$\int_{\Omega_X^\zeta} \left(\nabla_{\mathbf{X}}^{\text{Sym}} \mathbf{w}^\zeta \right)^T \boldsymbol{\sigma}^\zeta(\mathbf{X}) d\Omega = \int_{\partial\Omega_X^{t^\zeta}} \left(\mathbf{w}^\zeta \right)^T \bar{\mathbf{T}}^\zeta d\Gamma + \int_{\Omega_X^\zeta} \left(\mathbf{w}^\zeta \right)^T \mathbf{b}^\zeta d\Omega \quad (2.2)$$

$$\forall \mathbf{w}^\zeta \in W_{\Omega_X^\zeta}^0, \text{ where } W_{\Omega_X^\zeta} = \left\{ \mathbf{u}^\zeta \mid \mathbf{u}^\zeta \in H^1, \mathbf{u}^\zeta = \bar{\mathbf{u}}_\partial^\zeta \text{ on } \partial\Omega_X^{u^\zeta} \right\}$$

$$\text{and } W_{\Omega_X^\zeta}^0 = \left\{ \mathbf{w}^\zeta \mid \mathbf{w}^\zeta \in H^1, \mathbf{w}^\zeta = \mathbf{0} \text{ on } \partial\Omega_X^{u^\zeta} \right\}.$$

where $\mathbf{u}^\zeta, \mathbf{w}^\zeta$ are the trial and test functions for the displacement field, respectively; $\boldsymbol{\sigma}^\zeta$ is the stress field; \mathbf{n}^ζ is the unit normal vector to the boundary; the superscript ζ denotes existence of fine-scale features; $\nabla_{\mathbf{X}}^{\text{Sym}}$ is the symmetric part of the gradient operator with respect to argument \mathbf{X} . The above problem can be discretized at the scale of microconstituents and then Direct Numerical Simulation (DNS), in which case the microstructural geometry and properties are fully resolved.

To approximate the solution of the weak form (2.2) using computational continua (**C**²) formulation, the composite domain of Fig. 2.1 is replaced by a surrogate domain, depicted in Fig. 2.2.

The surrogate domain is discretized by coarse-scale elements with element size typically larger than the unit cell size.

The discretized weak form is integrated using the so-called nonlocal quadrature scheme by which the integration over the composite domain Ω_X^ζ is replaced by an integration over the so-called computational continua domain Ω_X^C , which consists of the disjoint union of \hat{N} computational unit cell domains $\Theta_{\hat{\mathbf{X}}_I}$ denoted as:

$$\Omega_X^C = \bigsqcup_{I=1}^{\hat{N}} \Theta_{\hat{\mathbf{X}}_I} \quad (2.3)$$

where $\hat{\mathbf{X}}_I$ denotes the coordinates of the centroid of so-called computational unit cell (CUC) domain $\Theta_{\hat{\mathbf{X}}_I}$. In the remaining of this manuscript, the notation $\Theta_{\hat{\mathbf{X}}_I}$ will be used interchangeably with Θ_I .

The nonlocal quadrature scheme is then defined as:

$$\int_{\Omega_X^\zeta} \Psi(\mathbf{X}) d\Omega = \sum_{I=1}^{\hat{N}} \frac{\hat{W}_I}{|\Theta_{\hat{\mathbf{X}}_I}|} \int_{\Theta_{\hat{\mathbf{X}}_I}} \Psi(\hat{\mathbf{X}}_I, \chi) d\Theta \quad (2.4)$$

where \hat{W}_I denotes the nonlocal quadrature weight and $|\Theta_{\hat{\mathbf{X}}_I}|$ is the measure (volume in 3D, area in 2D, length in 1D) of the I^{th} CUC domain in Ω_X^ζ . The weights \hat{W}_I and the positions $\hat{\mathbf{X}}_I$ are determined to exactly evaluate the integrals in (2.4) on a composite domain with integrand $\Psi(\mathbf{X})$ approximated by a polynomial of order m . The pair $(\hat{W}_I, \hat{\mathbf{X}}_I)$ depends on the computational unit cell size relative to the coarse-scale finite element size.

Since CUC is of finite size it is necessary to introduce a unit cell local coordinate system χ related to the global or composite reference system \mathbf{X} through the transformation:

$$\mathbf{X} = \chi + \hat{\mathbf{X}}_I \quad \left\{ (\mathbf{X}, \hat{\mathbf{X}}_I) \in \Omega_X^\zeta \quad \text{and} \quad \chi \in \Theta_I \right\} \quad (2.5)$$

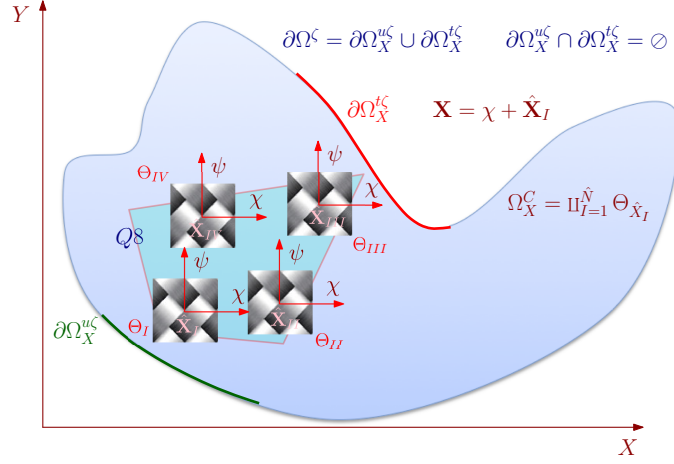


Figure 2.2: Surrogate computational continua domain. The computational unit cells are represented by Θ_I and are positioned at the nonlocal quadrature points $\hat{\mathbf{X}}_I$.

How to determine positions and weights of nonlocal quadrature points $\hat{\mathbf{X}}_I$ on unstructured meshes is one of the two main objectives of the present thesis and is the subject of chapter 3.

2.2 Additive Decomposition of Solution Fields

Following variational multiscale method [35] and the s-version of the finite element method [22], the displacement field \mathbf{u}^ζ in the composite domain is decomposed into a smooth coarse-scale part \mathbf{u}^C and a fine-scale perturbation $\mathbf{u}^{(1)}$:

$$\mathbf{u}^\zeta(\hat{\mathbf{X}}_I, \chi) = \mathbf{u}^C(\hat{\mathbf{X}}_I) + \mathbf{u}^{(1)}(\hat{\mathbf{X}}_I, \chi) \quad (2.6)$$

where the local CUC coordinate system (2.5) has been employed.

The fine-scale perturbation $\mathbf{u}^{(1)}$ is periodic, i.e.:

$$\mathbf{u}^{(1)}(\hat{\mathbf{X}}_I, \chi) = \mathbf{u}^{(1)}(\hat{\mathbf{X}}_I, \chi + \mathbf{c}) \quad (2.7)$$

where \mathbf{c} denotes the period.

Following (2.6), the strain field can be expressed as:

$$\boldsymbol{\varepsilon}^\zeta(\hat{\mathbf{X}}_I, \chi) = \boldsymbol{\varepsilon}^C(\hat{\mathbf{X}}_I, \chi) + \boldsymbol{\varepsilon}^{(1)}(\hat{\mathbf{X}}_I, \chi) \quad (2.8)$$

where $\boldsymbol{\varepsilon}^C$ and $\boldsymbol{\varepsilon}^{(1)}$ are the coarse and perturbation strains, respectively.

Herein we consider linear elastic microconstituents obeying:

$$\boldsymbol{\sigma}^\zeta(\hat{\mathbf{X}}_I, \chi) = L^\zeta(\chi) \boldsymbol{\varepsilon}^\zeta(\hat{\mathbf{X}}_I, \chi) \quad (2.9)$$

where $L^\zeta(\chi)$ is the elastic constitutive tensor. Inserting (2.8) into (2.9) yields

$$\boldsymbol{\sigma}^\zeta(\hat{\mathbf{X}}_I, \chi) = L^\zeta(\chi) \boldsymbol{\varepsilon}^C(\hat{\mathbf{X}}_I, \chi) + L^\zeta(\chi) \boldsymbol{\varepsilon}^{(1)}(\hat{\mathbf{X}}_I, \chi) = \boldsymbol{\sigma}^C(\hat{\mathbf{X}}_I, \chi) + \boldsymbol{\sigma}^{(1)}(\hat{\mathbf{X}}_I, \chi) \quad (2.10)$$

where $\boldsymbol{\sigma}^C$ and $\boldsymbol{\sigma}^{(1)}$ are the coarse and perturbation stresses, respectively.

2.3 The weak form of the coarse-scale problem

The weak form of the coarse-scale problem is derived by considering *coarse-scale test function* $\mathbf{w}^C(\mathbf{X})$ in (2.2), which yields:

$$\int_{\Omega_X} \left(\nabla_X^{\text{Sym}} \mathbf{w}^C \right)^T \boldsymbol{\sigma}^\zeta(\mathbf{X}) d\Omega = \int_{\partial\Omega'_X} \left(\mathbf{w}^C \right)^T \bar{\mathbf{T}}^\zeta d\Gamma + \int_{\Omega_X} \left(\mathbf{w}^C \right)^T \mathbf{b}^\zeta d\Omega \quad (2.11)$$

Employing the displacement decomposition (2.6) and the nonlocal quadrature scheme (2.4), the weak form of the coarse-scale problem is defined as follows:

Find $\mathbf{u}^C \in W_{\Omega_X}$ such that

$$\sum_{I=1}^{\hat{N}} \hat{\omega}_I \int_{\Theta_{\hat{\mathbf{x}}_I}} \left(\nabla_{\chi}^{\text{Sym}} \mathbf{w}^C \right)^T \sigma^{\zeta} (\hat{\mathbf{X}}_I, \chi) d\Theta = \int_{\partial\Omega_X^u} \left(\mathbf{w}^C \right)^T \bar{\mathbf{T}}^{\zeta} d\Gamma + \int_{\Omega_X} \left(\mathbf{w}^C \right)^T \mathbf{b}^{\zeta} d\Omega \quad (2.12)$$

$\forall \mathbf{w}^C \in W_{\Omega_X}^0$, where $W_{\Omega_X} = \left\{ \mathbf{u}^C \mid \mathbf{u}^C \in H^1, \mathbf{u}^C = \bar{\mathbf{u}}_{\partial}^{\zeta} \text{ on } \partial\Omega_X^u \right\}$

and $W_{\Omega_X}^0 = \left\{ \mathbf{w}^C \mid \mathbf{w}^C \in H^1, \mathbf{w}^C = \mathbf{0} \text{ on } \partial\Omega_X^u \right\}$.

2.4 The weak form of the fine-scale problem

The weak form of the fine-scale problem is derived by considering *fine-scale test function* $\mathbf{w}^{(1)}(\chi)$ in (2.2), which yields:

$$\int_{\Theta_{\hat{\mathbf{x}}_I}} \left(\nabla_{\chi}^{\text{Sym}} \mathbf{w}^{(1)} \right)^T \sigma^{\zeta} (\mathbf{X}) d\Theta = \int_{\partial\Theta_{\hat{\mathbf{x}}_I}^u} \left(\mathbf{w}^{(1)} \right)^T \sigma^{\zeta} (\mathbf{X}) \cdot \mathbf{n}^{\Theta} d\Gamma^{\Theta} + \int_{\Theta_{\hat{\mathbf{x}}_I}} \left(\mathbf{w}^{(1)} \right)^T \mathbf{b}^{\zeta} d\Theta \quad (2.13)$$

Consider an additive decomposition of the total stress into linear and periodic terms [26]:

$$\sigma_{ik}^{\zeta} \approx \alpha_{ikj} \chi_j + \sigma_{ik}^{\text{periodic}} \quad \{i, j, k\} = \{1, 2, 3\} \quad (2.14)$$

where α_{ikj} are coefficients that depend on the solution of the problem.

Inserting (2.14) into the boundary term of the right-hand side of eq. (2.13) yields:

$$\int_{\partial\Theta_{\hat{\mathbf{x}}_I}^u} w_i^{(1)} \sigma_{ik}^{\zeta} n_k^{\Theta} d\Gamma^{\Theta} = \int_{\partial\Theta_{\hat{\mathbf{x}}_I}^u} w_i^{(1)} \left(\alpha_{ikj} \chi_j + \sigma_{ik}^{\text{periodic}} \right) n_k^{\Theta} d\Gamma^{\Theta} \quad (2.15)$$

We assume a rectangular unit cell of size $l_{\chi} \times l_{\psi}$, which is parallel to the axes, as shown in Fig.

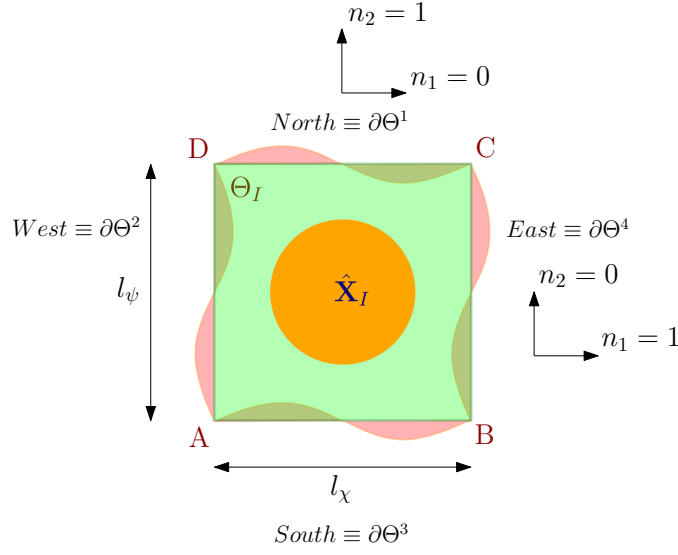


Figure 2.3: Periodic unit cell with edges parallel to the global reference axes.

2.3:

Due to periodicity, the periodic part of the total stress vanishes:

$$\int_{\partial\Theta_{\hat{\mathbf{x}}_I}^u} w_i^{(1)} \sigma_{ik}^{periodic} n_k^\Theta d\Gamma^\Theta = 0 \quad (2.16)$$

Expanding the nonperiodic term in (2.15) and taking into account periodicity of the test functions $w_i^{(1)}$ yields:

$$\begin{aligned} \int_{\partial\Theta_{\hat{\mathbf{x}}_I}^u} w_i^{(1)} \sigma_{ik}^\zeta n_k^\Theta d\Gamma^\Theta &= \alpha_{111} l_\chi \int_{\partial\Theta^{east}} w_1^{(1)} d\Gamma^{east} + \alpha_{211} l_\chi \int_{\partial\Theta^{east}} w_2^{(1)} d\Gamma^{east} \\ &+ \alpha_{122} l_\psi \int_{\partial\Theta^{north}} w_1^{(1)} d\Gamma^{north} + \alpha_{222} l_\psi \int_{\partial\Theta^{north}} w_2^{(1)} d\Gamma^{north} \end{aligned} \quad (2.17)$$

In the C^2 formulation [26] we impose (2.17) to vanish for arbitrary coefficients α_{ikj} which

yields:

$$\int_{\partial\Theta^{north}} w_{\chi}^{(1)} d\Gamma^{north} = 0 \quad (2.18a) \quad \int_{\partial\Theta^{north}} w_{\psi}^{(1)} d\Gamma^{north} = 0 \quad (2.18c)$$

$$\int_{\partial\Theta^{east}} w_{\chi}^{(1)} d\Gamma^{east} = 0 \quad (2.18b) \quad \int_{\partial\Theta^{east}} w_{\psi}^{(1)} d\Gamma^{east} = 0 \quad (2.18d)$$

The above can be represented in compact form as follows:

$$\int_{\partial\Theta_{\hat{\mathbf{x}}_I}^j} w_i^{(1)} d\Gamma_j^{\Theta} = 0 \text{ on } \partial\Theta_{\hat{\mathbf{x}}_I}^j \text{ for } j = \{1, \dots, 4\} \quad (2.19)$$

The boundary constraints (2.19) can be interpreted as a weak compatibility condition between adjacent unit cells.

Using the displacement decomposition (2.6), the strain decomposition (2.8) and the constitutive equation (2.9), the fine-scale weak form (2.13) reads as follows:

Find $\mathbf{u}^{(1)} \in W_{\Theta_{\hat{\mathbf{x}}_I}}$ such that

$$\begin{aligned} & \int_{\Theta_{\hat{\mathbf{x}}_I}} \left(\nabla_{\chi}^{\text{Sym}} \mathbf{w}^{(1)} \right)^{\text{T}} L^{\zeta}(\chi) \varepsilon^{(1)}(\hat{\mathbf{X}}_I, \chi) d\Theta \\ & = - \int_{\Theta_{\hat{\mathbf{x}}_I}} \left(\nabla_{\chi}^{\text{Sym}} \mathbf{w}^{(1)} \right)^{\text{T}} L^{\zeta}(\chi) \varepsilon^{\text{C}}(\hat{\mathbf{X}}_I, \chi) d\Theta + \int_{\Theta_{\hat{\mathbf{x}}_I}} \left(\mathbf{w}^{(1)} \right)^{\text{T}} \mathbf{b}^{\zeta} d\Theta \end{aligned} \quad (2.20)$$

$\forall \mathbf{w}^{(1)} \in W_{\Theta_{\hat{\mathbf{x}}_I}}^0$, where $W_{\Theta_{\hat{\mathbf{x}}_I}} = \left\{ \mathbf{u}^{(1)} \mid \mathbf{u}^{(1)} \in H^1, \chi\text{-periodic on } \partial\Theta_{\hat{\mathbf{x}}_I}^u \right\}$ and

$$W_{\Theta_{\hat{\mathbf{x}}_I}}^0 = \left\{ \mathbf{w}^{(1)} \mid \mathbf{w}^{(1)} \in H^1, \int_{\partial\Theta_{\hat{\mathbf{x}}_I}^j} \mathbf{w}^{(1)} d\Gamma^{\Theta} = 0 \text{ on } \partial\Theta_{\hat{\mathbf{x}}_I}^j \text{ for } j = \{1, \dots, 4\} \right\}$$

where $\bigcup_{j=1}^4 \partial\Theta_{\hat{\mathbf{x}}_I}^j = \partial\Theta_{\hat{\mathbf{x}}_I}$ and $\partial\Theta_{\hat{\mathbf{x}}_I}^i \cap \partial\Theta_{\hat{\mathbf{x}}_I}^j = 0 \forall i \neq j$.

2.5 Discretization of the coarse-scale and fine-scale problems

Galerkin discretization is considered for the trial $\mathbf{u}^{(1)}$ and test $\mathbf{w}^{(1)}$ functions of the perturbation field at the element level

$$\mathbf{u}^{(1)}(\hat{\mathbf{X}}_I, \chi) \approx \mathbf{u}_e^{(1)}(\hat{\mathbf{X}}_I, \chi) = \mathbf{N}^F(\chi) \mathbf{d}_{I,e}^{(1)} \quad (2.21a)$$

$$\mathbf{w}^{(1)}(\hat{\mathbf{X}}_I, \chi) \approx \mathbf{w}_e^{(1)}(\hat{\mathbf{X}}_I, \chi) = \mathbf{N}^F(\chi) \mathbf{c}_{I,e}^{(1)} \quad (2.21b)$$

where $\chi \in \Theta_{\hat{\mathbf{x}}_I}^e$, and for conciseness we denote $\mathbf{d}_{I,e}^{(1)} \equiv \mathbf{d}_e^{(1)}(\hat{\mathbf{X}}_I)$, $\mathbf{c}_{I,e}^{(1)} \equiv \mathbf{c}_e^{(1)}(\hat{\mathbf{X}}_I)$ the nodal values of the trial and test functions, respectively, of the e^{th} element in the I^{th} unit cell. $\mathbf{N}^F(\chi)$ denotes the unit cell shape functions defined on the unit cell element domain $\Theta_{\hat{\mathbf{x}}_I}^e$.

Similarly, Galerkin discretization is employed for the trial \mathbf{u}^C and test \mathbf{w}^C functions of the coarse-scale displacement field

$$\mathbf{u}^C(\mathbf{X}) \approx \mathbf{u}_e^C(\mathbf{X}) = \mathbf{N}^C(\mathbf{X}) \mathbf{d}_e^C \quad (2.22a)$$

$$\mathbf{w}^C(\mathbf{X}) \approx \mathbf{w}_e^C(\mathbf{X}) = \mathbf{N}^C(\mathbf{X}) \mathbf{c}_e^C \quad (2.22b)$$

where $\mathbf{d}_e^C, \mathbf{c}_e^C$ denote the nodal values of the trial and test functions, respectively, of the e^{th} element in the coarse-scale domain $\Omega_{\mathbf{X}}^e$, and $\mathbf{N}^C(\mathbf{X})$ denotes the coarse-scale element shape functions.

2.5.1 Discrete coarse-scale problem

Inserting (2.22a,2.22b), (2.21a) into the coarse-scale weak form (2.12), using (2.10) and requiring the resulting system to hold for arbitrary coefficients \mathbf{c}^C , yields the discrete coarse-scale problem:

$$\mathbb{A}_{e=1}^{n_{el}} \left\{ \mathbf{K}_e^C \mathbf{d}_e^C + \mathbf{K}_e^{CF} + \mathbf{F}_e^{\partial C} - \mathbf{F}_{b,e}^C \right\} = \mathbf{0} \quad (2.23)$$

where \mathbb{A} is the finite element assembly operator, the index e denotes the element count in the coarse-scale mesh and n_{el} is the number of coarse-scale elements. The coarse-scale element matrices are defined as follows:

$$\mathbf{K}_e^C = \sum_{I=1}^{\hat{N}_e} \hat{\omega}_I \mathbf{K}_I^C \quad (2.24a)$$

$$\mathbf{K}_I^C = \int_{\Theta_{\hat{\mathbf{x}}_I}} \left(\nabla_{\chi}^{\text{Sym}} \mathbf{N}^C(\hat{\mathbf{X}}_I, \chi) \right)^T L_e^{\zeta}(\chi) \left(\nabla_{\chi}^{\text{Sym}} \mathbf{N}^C(\hat{\mathbf{X}}_I, \chi) \right) d\Theta \quad (2.24b)$$

$$\mathbf{K}_e^{CF} = \sum_{I=1}^{\hat{N}_e} \hat{\omega}_I \mathbf{K}_I^{CF} \mathbf{d}_I^{(1)} \quad (2.24c)$$

$$\mathbf{K}_I^{CF} = \int_{\Theta_{\hat{\mathbf{x}}_I}} \left(\nabla_{\chi}^{\text{Sym}} \mathbf{N}^C(\hat{\mathbf{X}}_I, \chi) \right)^T L_e^{\zeta}(\chi) \left(\nabla_{\chi}^{\text{Sym}} \mathbf{N}^F(\chi) \right) d\Theta = \left(\mathbf{K}_I^{FC} \right)^T \quad (2.24d)$$

$$\mathbf{F}_e^{\partial C} = \mathbf{K}_{es}^C \mathbf{d}_e^{\partial C} \quad (2.24e)$$

$$\mathbf{F}_{b,e}^C = \int_{\Omega_X^e} \left(\mathbf{N}^C(\mathbf{X}) \right)^T \mathbf{b}^{\zeta} d\Omega^e \quad (2.24f)$$

where \hat{N}_e is the number of unit cells (nonlocal quadrature points) in a coarse-scale element.

2.5.2 Discrete unit cell problem

Substituting the discretizations (2.21a), (2.21b) and (2.22a), and (2.10) into the fine-scale weak form (2.20), and requiring the resulting system to hold for arbitrary coefficients $\mathbf{c}^{(1)}$, the following matrix form of the unit cell problem is obtained:

$$\mathbf{K}_I^F \mathbf{d}_I^{(1)} + \mathbf{K}_I^{FC} \mathbf{d}_e^C = \mathbf{F}_I^b \quad (2.25)$$

where $\mathbf{d}_I^{(1)}$ is the displacement vector of the I^{th} unit cell and \mathbf{d}_e^C is the displacement vector of the coarse-scale element e which serves as forcing term to I^{th} unit cell problem. The matrices in (2.25) are defined over the unit cell domain $\Theta_{\hat{\chi}_I}$ and are expressed as follows:

$$\mathbf{K}_I^F = \bigtriangleup_{e=1}^{n_{el}^{uc}} \int_{\Theta_e} \left(\nabla_{\chi}^{\text{Sym}} \mathbf{N}^F(\chi) \right)^T L_e^{\zeta}(\chi) \left(\nabla_{\chi}^{\text{Sym}} \mathbf{N}^F(\chi) \right) d\Theta \quad (2.26a)$$

$$\mathbf{K}_I^{FC} = \bigtriangleup_{e=1}^{n_{el}^{uc}} \int_{\Theta_e} \left(\nabla_{\chi}^{\text{Sym}} \mathbf{N}^F(\chi) \right)^T L_e^{\zeta}(\chi) \left(\nabla_{\chi}^{\text{Sym}} \mathbf{N}^C(\hat{\mathbf{X}}_I, \chi) \right) d\Theta \quad (2.26b)$$

$$\mathbf{F}_I^b = \bigtriangleup_{e=1}^{n_{el}^{uc}} \int_{\Theta_e} \left(\mathbf{N}^F(\chi) \right)^T \mathbf{b}^{\zeta} d\Theta \quad (2.26c)$$

where the index e denotes element count in the unit cell mesh and n_{el}^{uc} denotes the total number of elements in the unit cell mesh.

2.6 Solution of the coupled system

From eq. (2.25) it can be seen that unit cells are uncoupled from each other; their solution depends only on the coarse-scale problem quantities of the coarse-scale element they are associated with. Moreover, it is possible to derive an explicit expression linking kinematic quantities of the

coarse-scale problem and those of perturbation problem. This can be accomplished through appropriate condensation of the fine-scale problem on the coarse-scale element level. This procedure is summarized below:

1. Solve the unit cell problem, eq. (2.25), for $\mathbf{d}_I^{(1)}$

$$\mathbf{d}_I^{(1)} = -\mathbf{K}_I^{-F} \left(\mathbf{K}_I^{FC} \mathbf{d}_e^C - \mathbf{F}_I^b \right) \quad (2.27)$$

2. Use $\mathbf{d}_I^{(1)}$ to form \mathbf{K}_e^{CF} in eq. (2.24c)

$$\mathbf{K}_e^{CF} = - \left(\sum_{I=1}^{\hat{N}_e} \hat{\omega}_I \mathbf{K}_I^{CF} \mathbf{K}_I^{-F} \mathbf{K}_I^{FC} \right) \mathbf{d}_e^C \quad (2.28)$$

3. Substitute \mathbf{K}_e^{CF} into eq. (2.23) and rearrange to form a system of unknown \mathbf{d}^C :

$$\mathbf{K}_{eff}^C \mathbf{d}^C = -\mathbf{R}_{eff}^{CF} - \mathbf{F}^{\partial C} + \mathbf{F}_b^C \quad (2.29)$$

4. Solve the coarse-scale problem, eq. (2.29), for \mathbf{d}^C
5. Post process by substituting the coarse-scale problem solution \mathbf{d}^C into (2.27) to obtain the perturbation problem solution.

Chapter 3

Computational Continua and Non-local Quadrature Scheme for Unstructured Finite Element Meshes

3.1 Introduction

The computational continua (C^2) framework, which is a variant of higher order computational homogenization theories that is free of scale separation, does not require higher order finite element continuity and is free of higher order boundary conditions, has been generalized to unstructured meshes. The salient features of the proposed generalization are [20]: (i) nonlocal quadrature scheme for distorted elements that accounts for unit cell distortion in the parent element domain, and (ii) an approximate variant of the nonlocal quadrature that eliminates the cost of computing positions of the quadrature points in the pre-processing stage. The performance of the C^2 framework on unstructured meshes has been compared to the first-order homogenization theory and the direct numerical simulation (DNS).

3.2 General formulation of nonlocal quadrature scheme

In this chapter the nonlocal quadrature scheme (2.4) for distorted elements is developed.

The integrals on both sides of eq. (2.4) are evaluated over the standard (or parent) finite element domains $\Omega_d^S, d = \{1, 2, 3\}$. For the **Left-Hand Side (LHS)** of (2.4) the standard domains are defined as:

$$\Omega_1^S : \boldsymbol{\xi} \equiv \xi_1 \equiv \xi \in [-1, +1]; \quad d\Omega_1^S \equiv d\xi \quad \text{for 1D} \quad (3.1a)$$

$$\Omega_2^S : \boldsymbol{\xi} \equiv (\xi_1, \xi_2) \equiv (\xi, \eta) \text{ with } [\xi \times \eta] \in [-1, +1]; \quad d\Omega_2^S \equiv d\xi d\eta \quad \text{for 2D} \quad (3.1b)$$

$$\Omega_3^S : \boldsymbol{\xi} \equiv (\xi_1, \xi_2, \xi_3) \equiv (\xi, \eta, \varsigma) \text{ with } [\xi \times \eta \times \varsigma] \in [-1, +1]; \quad d\Omega_3^S \equiv d\xi d\eta d\varsigma \quad \text{for 3D} \quad (3.1c)$$

Then, using the above definition (3.1), the **LHS** of (2.4) is written as:

$$\int_{\Omega_X^e} \Psi(\mathbf{X}) d\Omega = \int_{\Omega_d^S} \Psi(\boldsymbol{\xi}) \left| J_d^S(\boldsymbol{\xi}) \right| d\Omega_d^S = \int_{\Omega_d^S} \bar{\Psi}(\boldsymbol{\xi}) d\Omega_d^S = \int_{-1}^{+1} \dots \int_{-1}^{+1} \bar{\Psi}(\xi_1, \dots, \xi_d) d\xi_1 \dots d\xi_d \quad (3.2)$$

where $\left| J_d^S(\boldsymbol{\xi}) \right|$ is the determinant of the Jacobian matrix mapping the coarse-scale element $\Omega_X^e \in \mathbb{R}^d$ onto the standard domain Ω_d^S .

Note that the integrand in (3.2) is defined as:

$$\bar{\Psi}(\boldsymbol{\xi}) = \Psi(\boldsymbol{\xi}) \left| J_d^S(\boldsymbol{\xi}) \right| \quad (3.3)$$

For the evaluation of the **Right-Hand Side (RHS)** of (2.4) by nonlocal quadrature consider Fig.3.1. Fig. 3.1(a) shows a physical 2D element domain $\Omega_X^e : [X \times Y] \subset \mathbb{R}^2$ and one representative **CUC** domain $\Theta_I : [\chi \times \psi] \subset [X \times Y]$ with centroid coordinates $(\hat{X}_I, \hat{Y}_I) \in \mathbb{R}^2$. The physical element domain Ω_X^e is mapped onto the standard domain $\Omega_d^S : \boldsymbol{\xi} \in \mathbb{R}^d$, (see Fig.3.1(b)), by the Jacobian

3.2. GENERAL FORMULATION OF NONLOCAL QUADRATURE SCHEME

$J_d^S(\xi)$. Due to the mapping $\Omega_X^e \rightarrow \Omega_d^S$ the **CUC** domain Θ_I is now mapped to the domain $\Theta'_I \subset \Omega_d^S$ with a local centroidal coordinate system $\chi' = [\chi' \times \psi']$ and origin $(\hat{\xi}_I, \hat{\eta}_I) \in \Omega_d^S$. Notice that Θ'_I is in general a quadrilateral with curved edges.

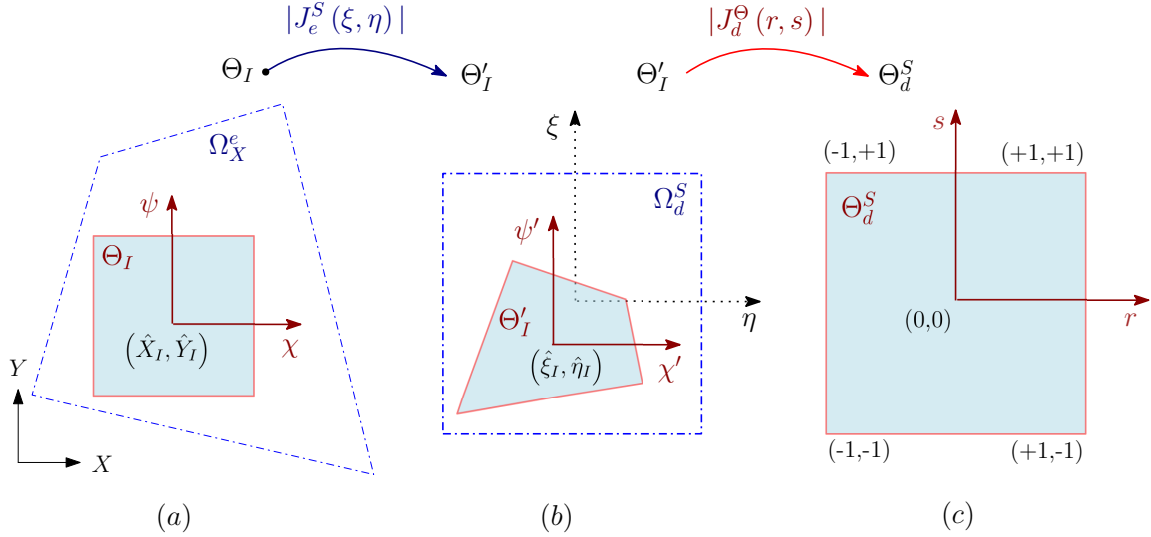


Figure 3.1: Consecutive isoparametric mappings of **CUC** domain in 2D: (a) from $\Theta_I \subset \Omega_X^e$ in the physical domain of the hosting element to (b) $\Theta'_I \subset \Omega_d^S : [\xi \times \eta] \in [-1, +1]$, in the standard 2D element domain, to (c) $\Theta_d^S : [r \times s] \in [-1, +1]$, the standard 2D domain of the distorted **CUC**.

Following the previous discussion, the integral in the **RHS** of (2.4) can be written as follows:

$$\frac{\hat{W}_I}{|\Theta_I|} \int_{\Theta_I} \Psi(\hat{\mathbf{X}}_I, \chi) d\Theta = \frac{\hat{W}_I}{|\Theta'_I|} \int_{\Theta'_I} \Psi(\xi) |J_d^S(\xi)| d\Theta' = \frac{\hat{W}_I}{|\Theta'_I|} \int_{\Theta'_I} \bar{\Psi}(\xi) d\Theta' \quad (3.4)$$

For convenience, we employ the following concise notation for the computational unit cell domains Θ'_I :

$$\Theta'_I \subseteq \Omega_1^S : \xi \in [-1, +1]; \quad d\Theta' \equiv d\xi \quad \text{for 1D} \quad (3.5a)$$

$$\Theta'_I \subseteq \Omega_2^S : [\xi \times \eta] \in [-1, +1]; \quad d\Theta' \equiv d\xi d\eta \quad \text{for 2D} \quad (3.5b)$$

$$\Theta'_I \subseteq \Omega_3^S : [\xi \times \eta \times \zeta] \in [-1, +1]; \quad d\Theta' \equiv d\xi d\eta d\zeta \quad \text{for 3D} \quad (3.5c)$$

and for the standard CUC domains Θ_d^S :

$$\Theta_1^S : \mathbf{r} \equiv r \in [-1, +1]; \quad d\Theta_1^S \equiv dr \quad \text{for 1D} \quad (3.6a)$$

$$\Theta_2^S : \mathbf{r} \equiv (r, s) \text{ with } [r \times s] \in [-1, +1]; \quad d\Theta_2^S \equiv drds \quad \text{for 2D} \quad (3.6b)$$

$$\Theta_3^S : \mathbf{r} \equiv (r, s, t) \text{ with } [r \times s \times t] \in [-1, +1]; \quad d\Theta_3^S \equiv drdsdt \quad \text{for 3D} \quad (3.6c)$$

As a final step towards the evaluation of the RHS of (2.4), the CUC domain Θ'_I is mapped onto the standard element domain Θ_d^S , as shown in Fig.3.1(c). Following this mapping, eq. (3.4) can be expressed as:

$$\frac{\hat{W}_I}{|\Theta'_I|} \int_{\Theta'_I} \bar{\Psi}(\boldsymbol{\xi}) d\Theta' = \frac{\hat{W}_I}{|\Theta'_I|} \int_{\Theta_d^S} \bar{\Psi}(\hat{\boldsymbol{\xi}}_I, \mathbf{r}) \left| J_d^\Theta(\hat{\boldsymbol{\xi}}_I, \mathbf{r}) \right| d\Theta^S \quad (3.7)$$

where $J_d^\Theta(\hat{\boldsymbol{\xi}}_I, \mathbf{r})$ is the Jacobian expressed as a function of the Non-Local Quadrature (NLQ) sampling points $\hat{\boldsymbol{\xi}}_I$.

Evaluation of Θ'_I in Ω_d^S is obtained by integrating the determinant $\det \left[J_d^\Theta(\hat{\boldsymbol{\xi}}_I, \mathbf{r}) \right] \equiv \left| J_d^\Theta(\hat{\boldsymbol{\xi}}_I, \mathbf{r}) \right|$ over the standard domain Θ_d^S :

$$|\Theta'_I| = \int_{\Theta_d^S} \left| J_d^\Theta(\hat{\boldsymbol{\xi}}_I, \mathbf{r}) \right| d\Theta^S \quad (3.8)$$

Note that a closed-form relation between $|\Theta'_I|$ in Ω_d^S and $|\Theta_I|$ in Θ_d^S is possible only for 1D elements, 2D rectangular elements and 3D cubic elements.

The final system of equations from which the positions and weights of nonlocal quadrature points is obtained by combining (3.2), (3.7) and (3.8), which yields:

$$\int_{\Omega_d^S} \bar{\Psi}(\boldsymbol{\xi}) d\Omega_d^S = \sum_{I=1}^{\hat{N}} \hat{W}_I^{\Theta_d^S} \frac{\int_{\Theta_d^S} \bar{\Psi}(\hat{\boldsymbol{\xi}}_I, \mathbf{r}) \left| J_d^{\Theta}(\hat{\boldsymbol{\xi}}_I, \mathbf{r}) \right| d\Theta^S}{\int_{\Theta_d^S} \left| J_d^{\Theta}(\hat{\boldsymbol{\xi}}_I, \mathbf{r}) \right| d\Theta^S} \quad (3.9)$$

The weights \hat{W}_I and coordinates $\hat{\boldsymbol{\xi}}_I$ are chosen to satisfy (3.9) with the integrand $\bar{\Psi}(\boldsymbol{\xi})$ approximated by a polynomial of order m . The pair $(\hat{W}_I, \hat{\boldsymbol{\xi}}_I)$ depends on the CUC size $|\Theta'_I|$ relative to the coarse-scale finite element size.

3.3 Non-local quadrature for structured meshes

For one dimensional domains [26], the NLQS is derived in such a way that polynomials of ξ of a given order m are exactly integrated:

$$\bar{\Psi}(\xi) = \xi^n; \quad m = \{0, 1, 2, \dots, m\} \quad (3.10)$$

The simplest 1D element that can capture gradient effects is the three-node quadratic element, $L3$. For $L3$ the minimum number of non-local integration points is two. Thus, two computational unit cells are centered at \hat{X}_J for $J = \{I, II\}$. For $L3$, the highest polynomial function to be integrated exactly is 3.

The one-dimensional NLQS (3.9) with two non-local quadrature points is expressed as follows:

$$\int_{-1}^{+1} \xi^m d\xi = \sum_{I=1}^{\hat{N}^e} \frac{\hat{W}_I}{\Theta'_I} \frac{1}{m+1} \left[\left(\hat{\xi}_I + \frac{1}{2} \Theta'_I \right)^{m+1} - \left(\hat{\xi}_I - \frac{1}{2} \Theta'_I \right)^{m+1} \right] \quad (3.11)$$

where $\Theta_I = J^e \Theta'_I$, $J^e = L_e/2$ being the Jacobian of the 1D isoparametric mapping and L_e the length of the 1D element.

For $m = \{0, 1, 2, 3\}$ eq. (3.11) yields a system of four nonlinear equations with four unknowns:

$$\begin{bmatrix} 1 & 1 \\ \hat{\xi}_I & \hat{\xi}_{II} \\ \hat{\xi}_I^2 + \frac{1}{12}\Theta_I'^2 & \hat{\xi}_{II}^2 + \frac{1}{12}\Theta_{II}'^2 \\ \hat{\xi}_I \left(\hat{\xi}_I^2 + \frac{1}{4}\Theta_I'^2 \right) & \hat{\xi}_{II} \left(\hat{\xi}_{II}^2 + \frac{1}{4}\Theta_{II}'^2 \right) \end{bmatrix} \begin{bmatrix} \hat{W}_I \\ \hat{W}_{II} \end{bmatrix} = \begin{bmatrix} 2 \\ 0 \\ 2/3 \\ 0 \end{bmatrix} \quad (3.12)$$

The solution of (3.12) is [23, 26]:

$$\hat{\xi}_I = \pm \sqrt{\frac{1}{3} - \frac{\Theta_I'^2}{12}} \quad \hat{W}_I = 1 \quad \Theta_I' \leq 2 \quad (3.13)$$

For a cubic (four-node) 1D element, $L4$, the highest polynomial function to be integrated exactly is 4 which yields.

$$\xi_{I,III} = \pm \frac{1}{10} \sqrt{60 - 35\Theta_I'^2}; \quad \xi_{II} = 0; \quad \hat{W}_{I,III} = \frac{5}{3} \frac{4 - \Theta_I'^2}{12 - 7\Theta_I'^2}; \quad \hat{W}_{II} = 2 - 2\hat{W}_I; \quad \Theta_I' \leq 1 \quad (3.14)$$

Fig. 3.2 depicts the variation of the sampling points for a quadratic (a) and a cubic (b) element as a function of the unit cell size ratio, ζ .

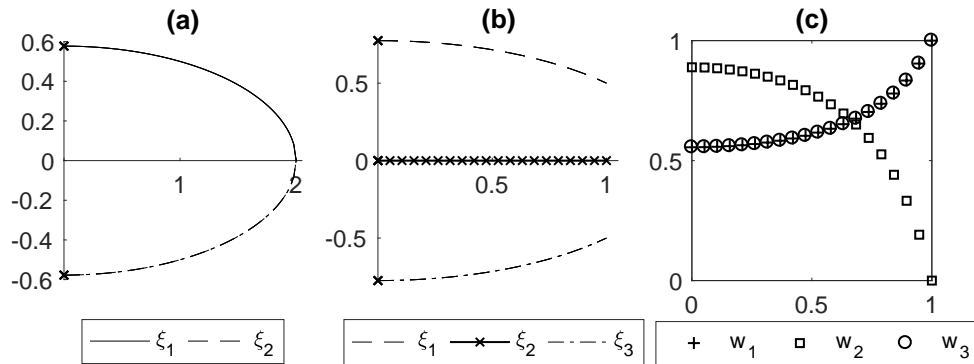


Figure 3.2: (a) Positions of nonlocal quadrature points in quadratic element, (b) Positions of nonlocal quadrature points in cubic element, (c) Weights of nonlocal quadrature points in cubic element.

It is noteworthy that the maximum permissible size of the unit cell is $\Theta_I = L_e$ for the $L3$ element and $\Theta_I = L_e/2$ for the $L4$ element. Increasing the number of non-local integration points reduces the maximum unit cell size that can be considered by \mathbf{C}^2 formulation.

Similarly to Gauss quadrature in multi-dimensions, the NLQS for rectangular elements can be determined by the tensor product rule using the 1D nonlocal quadrature points, as shown in Fig.3.3.

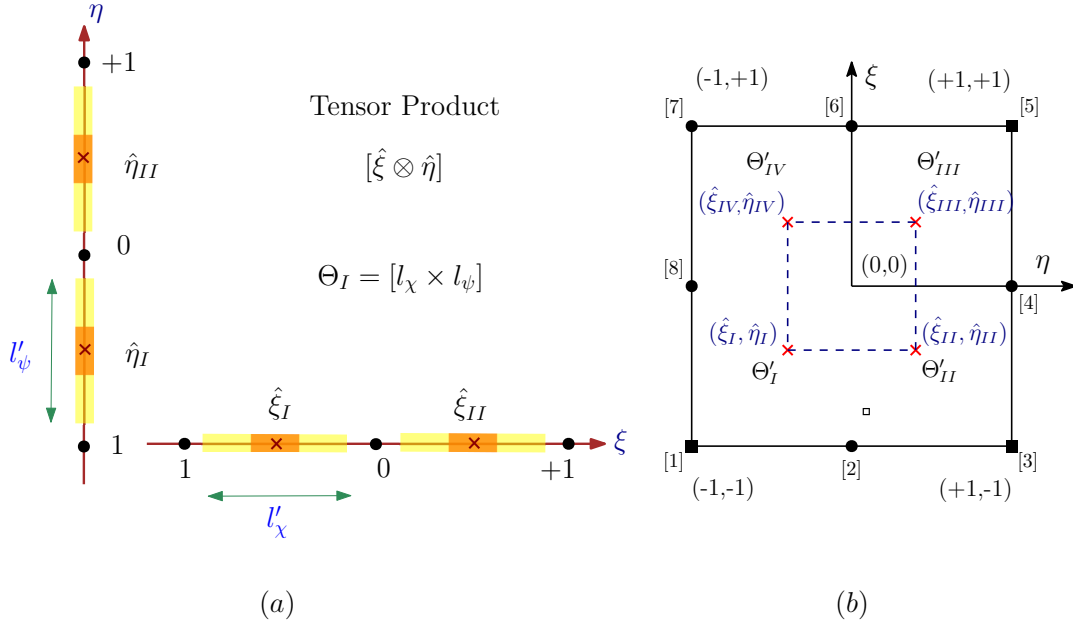


Figure 3.3: Tensor product rule for rectangular quadrilaterals: (a) the 1D NLQ expressed along two dimensions of the unit cell, (b) the standard 2D domain $[\xi \times \eta] \in [-1, +1]$ with the unit cells locations computed by the tensor product rule.

3.4 Nonlocal quadrature for unstructured meshes

In this section, the nonlocal quadrature scheme for a general two dimensional (2D) quadrilateral element is derived by matching two-dimensional monomials, as shown in Table 3.1. The function to be integrated is approximated by a polynomial:

$$\bar{\Psi}(\boldsymbol{\xi}) = \Psi(\boldsymbol{\xi}) \left| J_e^{Q8}(\boldsymbol{\xi}) \right| = \xi^m \eta^n; \quad (m, n) \in \{0, 1, 2, 3\}; \quad m + n \leq 4 \quad (3.15)$$

Table 3.1: Monomials for the 2D standard Q8 Serendipity element

Monomial degree $m+n$	Terms			
0:	1			
1:	ξ	η		
2:	ξ^2	$\xi\eta$	η^2	
3:	ξ^3	$\xi^2\eta$	$\xi\eta^2$	η^3
4:	$\xi^3\eta$		$\xi\eta^3$	

We consider the NLQS for a quadratic **eight-node serendipity element (Q8)**. The computational continua domain consists of the disjoint union of finite-size rectangular **CUC** denoted by $\Theta_I = [l_\chi \times l_\psi]$, as shown in Fig.3.4.

The general eight-node quadrilateral $Q8 \equiv \Omega_X^2 : [X \times Y] \in \mathbb{R}^2$ in Fig.3.4(a) is mapped onto the standard 2D domain $\Omega_2^S : [\xi \times \eta] \in [-1, +1]$, Fig. 3.4(b). Note that in the physical domain $Q8$ the $\Theta_k, k = \{I, II, III, IV\}$ are initially rectangular and parallel to the axes $X \times Y$ of the global reference system, Fig. 3.4(a). They become distorted (with curved sides) $\Theta'_k, k = \{I, II, III, IV\}$ when mapped onto Ω_2^S , Fig. 3.4(b).

The coordinates of the centroids $(\hat{\xi}_I, \hat{\eta}_I)$ and the weights \hat{W}_I for the four **CUC** give 12 unknowns to be determined by the NLQS.

The LHS of eq. (3.9) is evaluated analytically over the standard 2D domain Ω_2^S :

$$\int_{\Omega_2^S} \bar{\Psi}(\boldsymbol{\xi}) d\Omega_2^S = \int_{-1}^{+1} \int_{-1}^{+1} \xi^m \eta^n d\xi d\eta = \begin{cases} 0 & \text{if } (m+n) \text{ odd} \\ \frac{4}{(m+1)(n+1)} & \text{if } (m+n) \text{ even} \end{cases} \quad (3.16)$$

The RHS of eq. (3.9) is evaluated numerically over the local Gauss points (r_i, s_i) of the standard

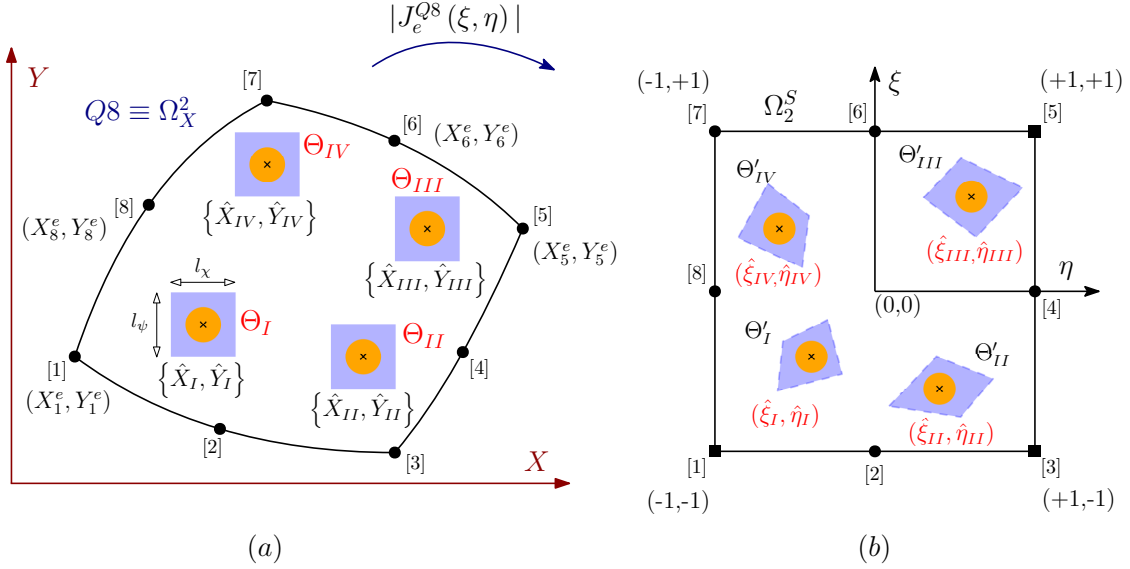


Figure 3.4: (a) The physical domain Ω_X^2 of a general curved-sided 8-node quadrilateral element $Q8$. The unit cells $\Theta_i, i = \{I, II, III, IV\}$ are located at the NLQ points (\hat{X}_k, \hat{Y}_k) . (b) The standard 2D domain $\Omega_2^S : [\xi \times \eta] \in [-1, +1]$ of a quadrilateral element with the centroids of the unit cells Θ'_k at the NLQ points $(\hat{\xi}_k, \hat{\eta}_k), i = \{I, II, III, IV\}$ marked by \times .

unit cell domain Θ_2^S :

$$\begin{aligned}
 \sum_{I=1}^{\hat{N}} \frac{\hat{W}_I}{|\Theta'_I|} \int_{\Theta'_I} \hat{\Psi}(\boldsymbol{\xi}) d\Theta' &= \sum_{I=1}^{\hat{N}} \frac{\hat{W}_I}{|\Theta'_I|} \int_{\Theta_2^S} \hat{\Psi}(\hat{\boldsymbol{\xi}}_I, \mathbf{r}) \left| J_2^\Theta(\hat{\boldsymbol{\xi}}_I, \mathbf{r}) \right| d\Theta^S \\
 &= \sum_{I=1}^{\hat{N}} \frac{\hat{W}_I}{|\Theta'_I|} \int_{-1}^{+1} \int_{-1}^{+1} \hat{\Psi}(\hat{\boldsymbol{\xi}}_I, r, s) \left| J_2^\Theta(\hat{\boldsymbol{\xi}}_I, r, s) \right| dr ds
 \end{aligned} \tag{3.17}$$

Substituting the monomial function $\bar{\Psi}$ from (3.15) and using (3.8) for $|\Theta'_I|$ we get:

$$\begin{aligned}
 \frac{\hat{W}_I}{|\Theta'_I|} \int_{\Theta'_I} (\xi^m \eta^n) d\Theta' &= \hat{W}_I^{-1-1} \frac{\int_{-1}^{+1} \int_{-1}^{+1} [\xi^m \eta^n] (\hat{\xi}_I, \hat{\eta}_I, r, s) \left| J_2^\Theta (\hat{\xi}_I, \hat{\eta}_I, r, s) \right| dr ds}{\int_{-1}^{+1} \int_{-1}^{+1} \left| J_2^\Theta (\hat{\xi}_I, \hat{\eta}_I, r, s) \right| dr ds} \\
 &= \hat{W}_I \frac{\sum_{i=1}^{n_{gp}} \left[w_i (\xi^m \eta^n) (\hat{\xi}_I, \hat{\eta}_I, r_i, s_i) \left| J_2^\Theta (\hat{\xi}_I, \hat{\eta}_I, r_i, s_i) \right| \right]}{\sum_{i=1}^{n_{gp}} \left[w_i \left| J_2^\Theta (\hat{\xi}_I, \hat{\eta}_I, r_i, s_i) \right| \right]}
 \end{aligned} \tag{3.18}$$

Thus, the NLQS for the $Q8$ element is obtained by solving the system of twelve nonlinear equations for the monomials in Table 3.1:

$$\int_{-1}^{+1} \int_{-1}^{+1} \xi^m \eta^n d\xi d\eta = \sum_{I=1}^{\hat{N}} \hat{W}_I \frac{\sum_{i=1}^{n_{gp}} \left[w_i (\xi^m \eta^n) (\hat{\xi}_I, \hat{\eta}_I, r_i, s_i) \left| J_2^\Theta (\hat{\xi}_I, \hat{\eta}_I, r_i, s_i) \right| \right]}{\sum_{i=1}^{n_{gp}} \left[w_i \left| J_2^\Theta (\hat{\xi}_I, \hat{\eta}_I, r_i, s_i) \right| \right]} \tag{3.19}$$

The system of nonlinear equations obtained by (3.9) (or (3.19) for $Q8$) can be solved using the Newton-Raphson method that requires a good initial guess $({}^0\hat{\xi}_I, {}^0\hat{W}_I)$ for every CUC.

If element edges (faces) were parallel to the unit cell edges (faces in 3D), then the solution $(\hat{\xi}_I, \hat{W}_I)$ could be obtained by the tensor product rule, as discussed in the previous section. The extension of the tensor product rule to a general quadrilateral element requires definition of the **equivalent rectangular element** whose edges are parallel to those of the unit cell, Fig. 3.5. The equivalent rectangular element is defined to have the same area and centroid as the original quadrilateral element, and its dimensions L_x, L_y are determined by a least-squares minimization of the second moments of area I_{xx}, I_{yy} of the equivalent rectangular element and the original quadrilateral.

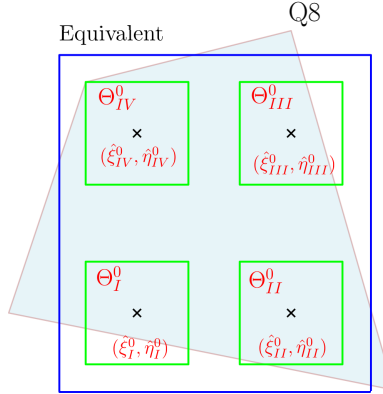


Figure 3.5: Equivalent rectangular of a general quadrilateral element Q8; Θ_J^0 are the CUC of the initial guess $({}^0\hat{\xi}_J, {}^0\hat{\eta}_J)$, for $J \in \{I, II, III, IV\}$.

Moreover, the nonlocal quadrature scheme in one dimension depends on the ratio of the unit cell length l_χ and the element size L_X . Consequently, the initial guess of the nonlocal quadrature points in a general quadrilateral element is defined as:

$${}^0\hat{\xi}_J = \pm \sqrt{\frac{1}{3} - \frac{\hat{\theta}_\xi^2}{12}}; \quad {}^0\hat{\eta}_J = \pm \sqrt{\frac{1}{3} - \frac{\hat{\theta}_\eta^2}{12}}; \quad {}^0\hat{W}_J = 1 \quad J = \{I, II, III, IV\} \quad (3.20)$$

where $\hat{\theta}_\xi, \hat{\theta}_\eta$ are the normalized unit cell dimensions defined as:

$$\hat{\theta}_\xi = 2 \frac{l_\chi}{L_x} = 2\zeta_x; \quad \hat{\theta}_\eta = 2 \frac{l_\psi}{L_y} = 2\zeta_y \quad (3.21)$$

where l_χ, l_ψ are the unit cell dimensions in the physical domain and ζ_x, ζ_y the corresponding size ratios.

Given the initial positions of nonlocal quadrature points (3.20) in the equivalent rectangular element, the equivalent rectangular element is incrementally transformed into the quadrilateral element (see Fig. 3.6) and in each increment, nonlocal quadrature points are recomputed until the final quadrilateral shape is reached.

For illustration, consider various Q8 elements: a square in Fig. 3.7; a rectangle in Fig. 3.8; a

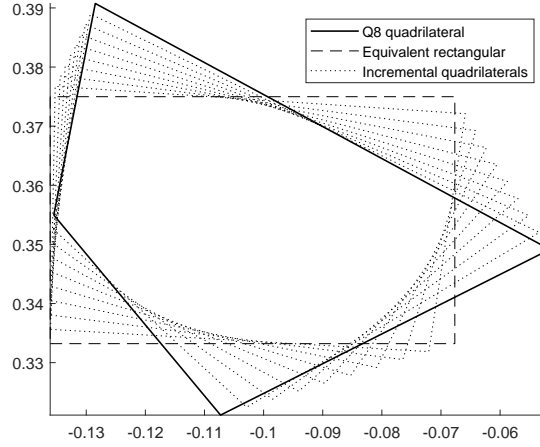


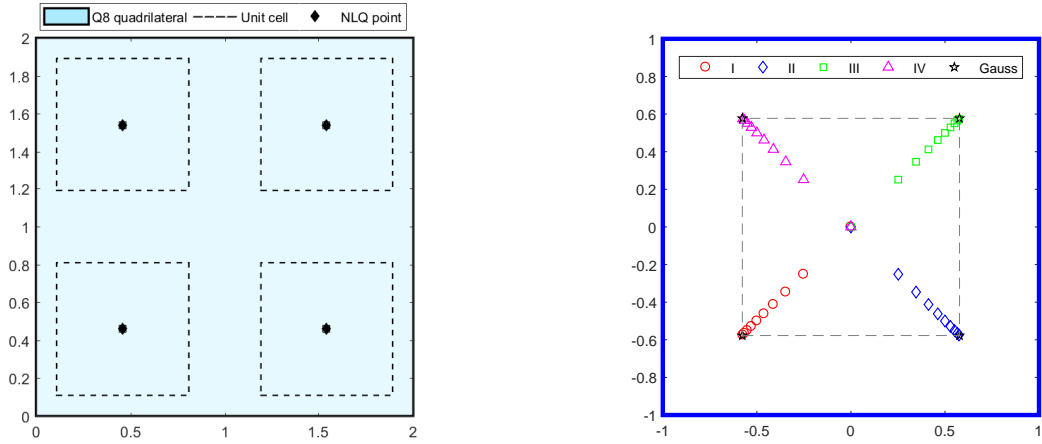
Figure 3.6: Incremental transformation of the equivalent rectangular element into the quadrilateral element during the Newton-Raphson solution.

rectangle rotated by 60° in Fig. 3.9; a general distorted quadrilateral in Fig. 3.10.

The coarse-scale elements in their physical domain are shown in Figs. 3.7a, 3.8a, 3.9a and 3.10a (shaded area with bold boundary). The CUC for a select size ratio ζ are also shown. The maximum unit cell size that can be used with these elements is as follows: $\zeta = 1.0$ for the square element in Fig. 3.7a, $\zeta_x = 0.50$ and $\zeta_y = 1.0$ for the rectangular element in Fig. 3.8a, $\zeta_x = 0.45125$ and $\zeta_y = 0.90250$ for a rotated rectangle in Fig. 3.9a and $\zeta_x = 0.4722$ and $\zeta_y = 0.7738$ for a distorted quadrilateral in Fig. 3.10a.

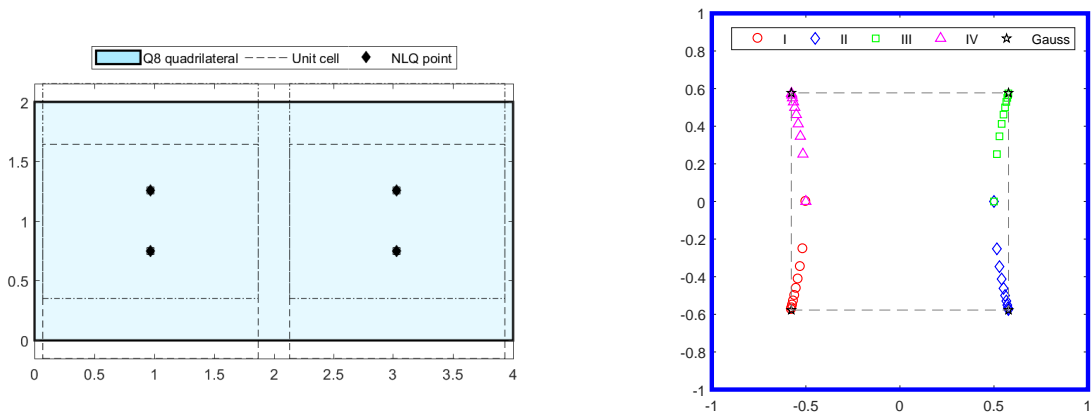
Figs. 3.7b, 3.8b, 3.9b and 3.10b show the NLQ loci for the corresponding elements in Figs. 3.7a, 3.8a, 3.9a and 3.10a, respectively. The loci show how the positions of the NLQ points in the standard 2D isoparametric domain $[\xi \times \eta] \in [-1, +1]$ change with respect to the size ratio ζ . As $\zeta \rightarrow 0$ the NLQ points move towards the Gauss points, located at the corners of the dashed gray frame. As ζ increases the NLQ points move away from the Gauss point locations; positions of which depends on the shape and orientation of the coarse-scale element. The maximum value of the size ratio also depends on the shape and orientation of the original quadrilateral.

3.4. NONLOCAL QUADRATURE FOR UNSTRUCTURED MESHES



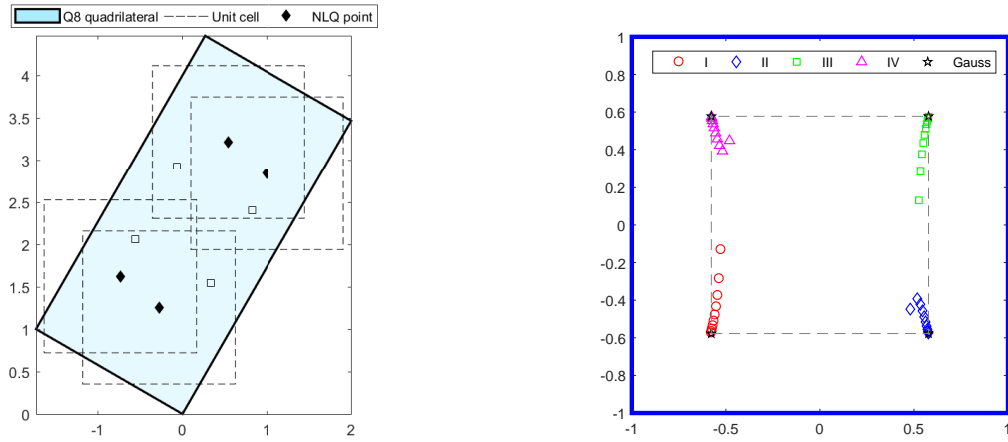
(a) Physical domain and CUC with size ratio $\zeta = 0.35$. (b) Locus of the NLQS points in the standard 2D domain $[\xi \times \eta] \in [-1, +1]$ for various ζ .

Figure 3.7: NLQS for a square Q8 element.



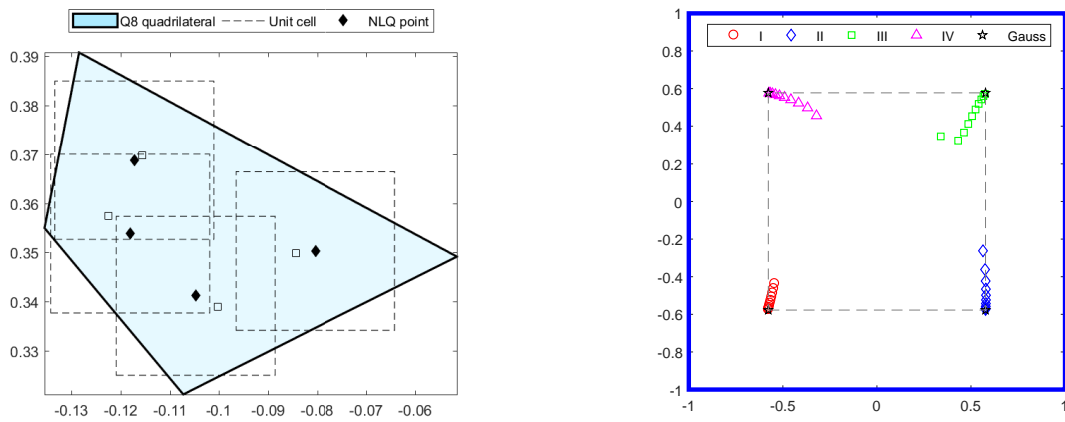
(a) Physical domain and CUC with size ratios $\zeta_x = 0.45$ and $\zeta_y = 0.90$. (b) Locus of the NLQS points in the standard 2D domain $[\xi \times \eta] \in [-1, +1]$ for various ζ .

Figure 3.8: NLQS for a rectangular Q8 element.



(a) Physical domain and **CUC** with maximum size ratios $\zeta_x = 0.45125$ and $\zeta_y = 0.90250$. (b) Locus of the **NLQS** points in the standard 2D domain $[\xi \times \eta] \in [-1, +1]$.

Figure 3.9: **NLQS** for a rotated rectangular Q8 element.



(a) Physical domain and **CUC** with maximum size ratios $\zeta_x = 0.4722$ and $\zeta_y = 0.7738$. (b) Locus of the **NLQS** points in the standard 2D domain $[\xi \times \eta] \in [-1, +1]$.

Figure 3.10: **NLQS** for a distorted Q8 quadrilateral element.

3.5 Approximate tensor-product based nonlocal quadrature on unstructured meshes

In this section we propose a tensor-product based [NLQS](#) that does not require solution of nonlinear system of equations for every element. The approximate nonlocal quadrature is based on the tensor-product rule where the main challenge is to determine the ratio between the unit cell size and the size of equivalent rectangular element as defined in Section [3.4](#). The proposed tensor-product based [NLQS](#) requires first to determine an equivalent rectangular element (as described in the previous section) and then to estimate the size ratio based on the quality measures of the element. We consider the following three quality measures: the skewness (S), the ratio of the minimum and maximum Jacobian values (J) and the taper (T). Table [3.2](#) depicts the ideal and threshold values— S_0, J_0, T_0 —recommended in practice [[54, 63](#)]:

Table 3.2: Quality measures for Q8 elements

	Skewness (S)	Jacobian ratio (J)	Taper (T)
Ideal values	0°	1.0	0
Threshold values	$S < S_0 \equiv 45^\circ$	$J > J_0 \equiv 0.6$	$T < T_0 \equiv 0.5$

If the quality measures for an individual element fall below the threshold values in Table [3.2](#), then the size ratio is reduced. The reduction factor is defined as a product of the above individual

quality measures:

$$f(T, S, J, \zeta) = f(T, \zeta) \times f(S, \zeta) \times f(J, \zeta) \quad (3.22a)$$

$$f(S, \zeta) = \operatorname{sech}[-(S - S_0) \zeta / (2S_0)] \quad (3.22b)$$

$$f(J, \zeta) = \operatorname{sech}[-(J - J_0) \zeta / (J_0/2)] \quad (3.22c)$$

$$f(T, \zeta) = \operatorname{sech}[-(T - T_0) \zeta] \quad (3.22d)$$

The effect of various quality measures on the size ratio reduction factor is depicted in Figs. 3.11a, 3.11b and 3.11c.

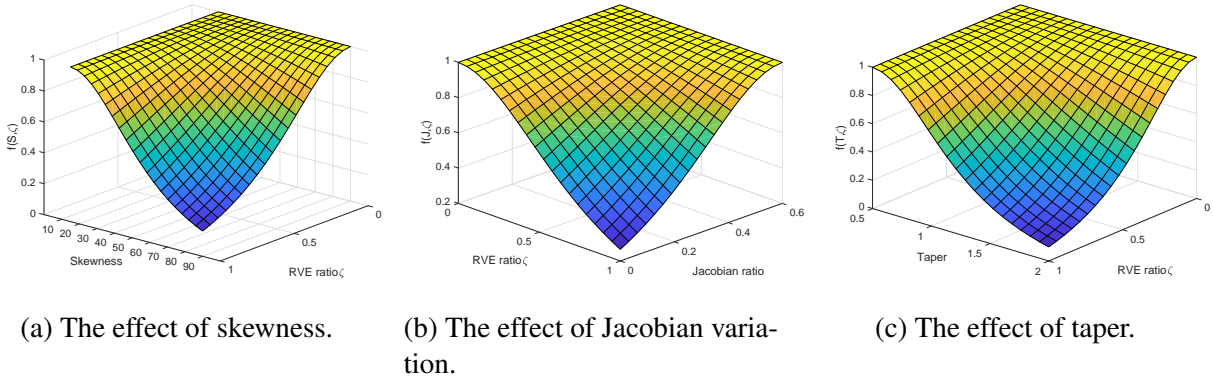


Figure 3.11: The effect of various quadrilateral quality measures on size ratio reduction factor.

3.6 Nonlocal quadrature for triangular elements

The nonlocal quadrature scheme for quadratic six-node straight-sided triangular elements is discussed in this section. The formulation will be performed with respect to the area coordinates (r, s, t) . For the exact integration, the physical domain of the triangle in Cartesian coordinates will be considered. For the nonlocal quadrature scheme, the [computational continua domain \(CCD\)](#) will be employed. The [CCD](#) consists, as mentioned earlier in this chapter, by the disjoint union

3.6. NONLOCAL QUADRATURE FOR TRIANGULAR ELEMENTS

of finite-sized rectangular computational unit cells denoted by $\Theta_I = [l_\chi \times l_\psi]$, as depicted in figure 3.12.

Similarly to (2.4), the integration over the composite domain of a triangle is given by:

$$\int_{\Omega_x^\zeta} \Psi(\mathbf{X}) d\Omega = \Delta \sum_{I=1}^{\hat{N}} \hat{W}_I \frac{1}{|\Theta_{\hat{x}_I}|} \int_{\Theta_{\hat{x}_I}} \Psi(\hat{\mathbf{X}}_I, \chi) d\Theta \quad (3.23)$$

where Δ is the area of the triangle:

$$\Delta = \frac{1}{2} J^\Delta; \quad J^\Delta \equiv \det \left(\frac{\partial(x,y)}{\partial(r,s,t)} \right) = \det \left(\begin{bmatrix} 1 & x_A & y_A \\ 1 & x_B & y_B \\ 1 & x_C & y_C \end{bmatrix} \right) \quad (3.24)$$

and the relationship between area and Cartesian coordinates is given by:

$$\begin{aligned} r + s + t &= 1 \\ r &= \frac{a_r + b_r x + c_r y}{2\Delta} & s &= \frac{a_s + b_s x + c_s y}{2\Delta} & t &= \frac{a_t + b_t x + c_t y}{2\Delta} \\ b_r &= y_B - y_C & b_s &= y_C - y_A & b_t &= y_A - y_B \\ c_r &= x_C - x_B & c_s &= x_A - x_C & c_t &= x_B - x_A \\ a_r &= x_B y_C - x_C y_B & a_s &= x_C y_A - x_A y_C & a_t &= x_A y_B - x_B y_A \end{aligned} \quad (3.25)$$

Consider polynomial functions for the integrand (summarized in Table 3.3):

$$\bar{\Psi}(r,s,t) = r^m s^n; \quad (m,n) \in \{0,1,2\}; \quad m+n \leq 2 \quad (3.26)$$

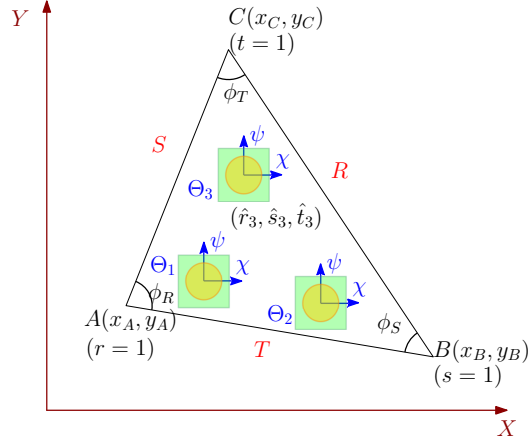


Figure 3.12: A triangular domain with unit cells Θ_I located at the nonlocal quadrature points $(\hat{r}_I, \hat{s}_I, \hat{t}_I)$. R, S, T are the lengths of the three edges and ϕ is the angle between two edges.

Table 3.3: Monomials for the 2D standard T6 element

Monomial degree:	Terms		
$m + n = 0:$	1		
$m + n = 1:$	r	s	
$m + n = 2:$	r^2	rs	s^2

The system of equations to be solved is:

$$\begin{aligned}
 1 &= \sum_{I=1}^3 \hat{W}_I \\
 \frac{1}{3} &= \sum_{I=1}^3 \hat{W}_I r_I \\
 \frac{1}{3} &= \sum_{I=1}^3 \hat{W}_I s_I \\
 \frac{1}{12} \left(1 - \frac{1}{4\Delta^2} (b_r b_s l_\chi^2 + c_r c_s l_\psi^2) \right) &= \sum_{I=1}^3 \hat{W}_I r_I s_I \\
 \frac{1}{12} \left(2 - \frac{1}{4\Delta^2} (b_r^2 l_\chi^2 + c_r^2 l_\psi^2) \right) &= \sum_{I=1}^3 \hat{W}_I r_I^2 \\
 \frac{1}{12} \left(2 - \frac{1}{4\Delta^2} (b_s^2 l_\chi^2 + c_s^2 l_\psi^2) \right) &= \sum_{I=1}^3 \hat{W}_I s_I^2
 \end{aligned} \tag{3.27}$$

3.6. NONLOCAL QUADRATURE FOR TRIANGULAR ELEMENTS

where the unknown position of integration points is expressed in the triangular coordinates as:

$$r_I = \frac{a_r + b_r \hat{X}_I + c_r \hat{Y}_I}{2\Delta} \quad s_I = \frac{a_s + b_s \hat{X}_I + c_s \hat{Y}_I}{2\Delta} \quad (3.28)$$

There are in total nine unknowns, and we have only six equations. To be able to solve the system we further make the following assumptions:

1. equal weights:

$$\hat{W}_1 = \hat{W}_2 = \hat{W}_3 = \frac{1}{3} \quad (3.29)$$

2. partial symmetry of the positions:

$$\hat{r}_1 = \hat{r}_2 \quad (3.30)$$

For a square unit cell $l_x = l_y = l$, the nonlinear system (3.27) has two sets of solutions:

$$\hat{r}_1 = \hat{r}_2 = \frac{4 \pm \sqrt{D_A}}{12} \quad \hat{r}_3 = \frac{2 \mp \sqrt{D_A}}{6} \quad (3.31a)$$

$$\hat{s}_1 = \frac{1 - \hat{s}_3 - \sqrt{D_s}}{2} \quad \hat{s}_2 = \frac{1 - \hat{s}_3 + \sqrt{D_s}}{2} \quad \hat{s}_3 = \frac{\sqrt{D_A} \mp c}{3\sqrt{D_A}} \quad (3.31b)$$

$$\hat{t}_I = 1 - \hat{s}_I - \hat{r}_I \quad I \in \{1, 2, 3\} \quad (3.31c)$$

where

$$D_A = 2(2 - 3\lambda_R^2); \quad D_B = 2(2 - 3\lambda_S^2); \quad D_s = -3\hat{s}_3^2 + 2\hat{s}_3 - \frac{1}{2}\lambda_S^2 \quad (3.32)$$

$$c = 3\lambda_R\lambda_S \cos \phi - 1; \quad \lambda_R = \frac{lR}{2\Delta}; \quad \lambda_S = \frac{lS}{2\Delta}$$

R and S are the lengths of the two edges that are opposite to vertices $r = 1$ and $s = 1$ respectively, and ϕ is the angle between the two edges, figure 3.12.

It would be interesting to investigate the two extreme cases, that is, when the unit cell becomes zero and when it becomes the maximum-optimum.

For the case when the unit cell size is equal to zero, the previous partially symmetric solution returns the regular Gauss quadrature points, as expected:

$$\hat{r}_1 = \hat{r}_2 = \frac{1}{2} \quad \hat{r}_3 = 0 \quad \hat{s}_3 = \frac{1}{2} \quad \hat{s}_1 = 0 \quad \hat{s}_2 = \frac{1}{2} \quad (3.33a)$$

$$\hat{r}_1 = \hat{r}_2 = \frac{1}{6} \quad \hat{r}_3 = \frac{2}{3} \quad \hat{s}_3 = \frac{1}{6} \quad \hat{s}_1 = \frac{2}{3} \quad \hat{s}_2 = \frac{1}{6} \quad (3.33b)$$

The solution (3.31) exists only when the following constraints are satisfied:

$$|2c| \leq \sqrt{D_A D_B} \quad (3.34a)$$

$$\lambda_R < \sqrt{\frac{2}{3}} \quad (3.34b)$$

$$\lambda_S < \sqrt{\frac{2}{3}} \quad (3.34c)$$

The above inequalities imply the following constraints on the unit cell size:

$$\begin{cases} \text{if } l_0 \leq l_2 & \text{then } 0 \leq l < \min\{l_0, l_1\} \\ \text{if } l_0 > l_2 & \text{then } 0 \leq l < l_1 \text{ or } l_2 \leq l \leq l_0 \end{cases} \quad (3.35)$$

where

$$\begin{aligned} l_1 &= \sqrt{\frac{1}{6} (R^2 + S^2 + T^2 - \sqrt{d})} \\ l_2 &= \sqrt{\frac{1}{6} (R^2 + S^2 + T^2 + \sqrt{d})} \\ d &= (R^2 + S^2 + T^2)^2 - 48\Delta^2 \\ l_0 &= \min \left\{ 2\sqrt{\frac{2}{3}} \frac{\Delta}{R}, 2\sqrt{\frac{2}{3}} \frac{\Delta}{S} \right\} \end{aligned} \quad (3.36)$$

where T is the length of the edge opposite to vertex $t = 1$, figure 3.12. When $l = l_1$ then two integration points in (3.31) coincide, $\hat{s}_1 = \hat{s}_2$ and $D_s = 0$. To avoid a unit cell size gap in (3.35), we

choose $0 \leq l < \min \{l_0, l_1\}$.

NLQ for equilateral triangle For an equilateral quadratic triangle with edges $R = S = T = L$ the NLQ scheme is fully symmetric, as can be seen from the following expressions:

$$\begin{aligned}
 \hat{r}_1 &= \hat{r}_2 = \hat{t}_1 = \hat{t}_3 = \hat{s}_2 = \hat{s}_3 = \beta \\
 \hat{s}_1 &= \hat{t}_2 = \hat{r}_3 = \alpha \\
 \alpha &= \frac{1 \mp \sqrt{1 - 2\zeta^2}}{3} \\
 \beta &= \frac{2 \pm \sqrt{1 - 2\zeta^2}}{6} \\
 \zeta &= \frac{1}{L}
 \end{aligned} \tag{3.37}$$

3.7 Numerical studies

In this section the C^2 formulation for unstructured meshes with the two nonlocal quadrature schemes is studied on two examples. The first example shown in Fig. 3.13, consists of a 2×2 plate with a dolphin-shaped hole, and the microstructure of a void of 50% volume fraction, Fig. 3.14. The physical size of the square unit cell is $l_\chi = l_\psi = 2/80$. The first example will be referred to as problem A. The second example shown in Fig. 3.15 consists of a 1×1 plate with a circular hole, and the microstructure of a continuous fiber—with 50% volume fraction, Fig. 3.16. The physical size of the rectangular unit cell is $l_\chi = 1/23, l_\psi = l_\chi/10$. The second example will be referred to as problem B.

In both problems, A and B, the plate is loaded by a uniform load $F_y = 0.1$ at the top boundary, while the motion of the bottom boundary is constrained in the loading direction. For problem A, the material properties of the matrix phase surrounding the voids are: $E = 100$ for Young's modulus and $\nu = 0.1$ for Poisson's ratio. For problem B, the Young's moduli are $E_f = 100$ and $E_m = 10$

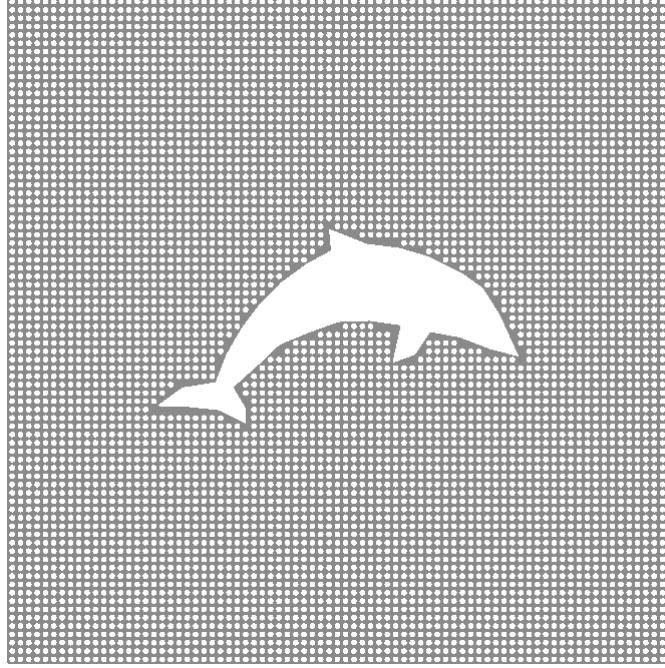


Figure 3.13: Geometry of problem A: Perforated dolphin-like plate.

for the fiber and matrix phases, respectively. Both fiber and matrix have the same Poisson's ratio, $\nu_f = \nu_m = 0.1$. The displacement contours are displayed in Figs. 3.31 and 3.32 for problems A and B, respectively. For brevity, C^2 only the solution from the exact NLQS is displayed; similar results hold for the tensor-product based NLQ.

For C^2 and the classical first-order ($O(1)$) homogenization formulations two coarse-scale meshes were employed for problem A, Fig. 3.17, and three coarse-scale meshes for problem B, Fig. 3.18. In the same figures randomly selected unit cells are depicted where the detailed stresses will be compared to the DNS.

In Figs. 3.19 and 3.20 the NLQ points corresponding to the exact and the tensor-product based quadratures are depicted in the parent finite element domain $[\xi \times \eta] \in [-1, +1]$ for the coarse-scale meshes of problems A and B, respectively. The Gauss points are marked by '*' and encompassed by dashed frame.

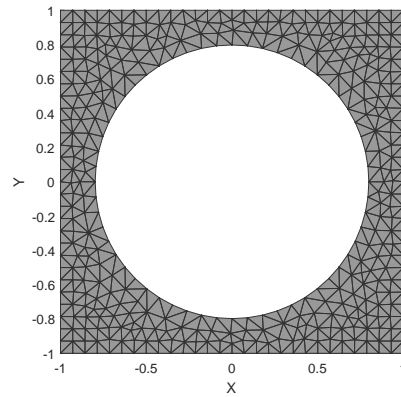


Figure 3.14: Unit cell mesh used in C^2 and $O(1)$ homogenization for problem A.

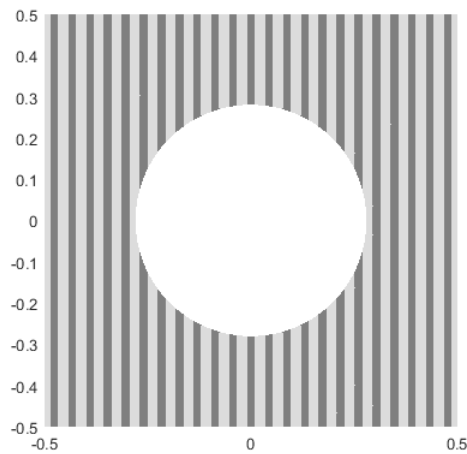


Figure 3.15: Geometry of problem B: plate with a circular hole and continuous fiber microstructure.

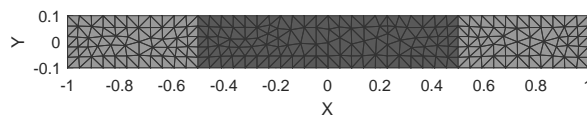


Figure 3.16: Unit cell mesh used in C^2 and $O(1)$ homogenization for problem B.

For the coarse-scale mesh, denoted by A1, of problem A, shown in Fig. 3.17a, the size of the unit cell is relatively small compared to the size of the coarse-scale elements Q8; that is why the majority of the NLQ points are close to the Gauss points (see Figs. 3.19a and 3.19b). For the coarse-scale mesh, A2, of problem A, the size ratio ζ of the unit cell spans a wide spectrum; that is why the NLQ points are spread out over the parent element domain (see Figs. 3.19c and 3.19d).

A similar situation is observed for the NLQ points in problem B, Fig. 3.20. As the coarse-scale mesh becomes finer (Figs. 3.18a-3.18c) the unit cell size ratio increases and the NLQ points move away from the Gauss points. For problem B, noteworthy is a slightly different pattern of the tensor-product based NLQ points, Figs. 3.20b, 3.20d and 3.20f. The fact that the unit cell, Fig. 3.16, has one dimension much smaller than the other, that is $\zeta_x \gg \zeta_y \rightarrow 0$, causes one coordinate of the NLQ to coincide with the corresponding Gauss quadrature points. This is expected according to eq. (3.20).

3.7.1 Global error measures

In this section we investigate the performance of the C^2 formulation with the two NLQ approaches and compare it with the DNS and $O(1)$ solutions. The notations C_{ex}^2 and C_{tp}^2 will be referred to the exact nonlocal quadrature and the tensor-product based approximation.

To quantify the accuracy of the global solution two error measures are considered:

1. the relative error in the total strain energy:

$$|\Delta\Pi| = \frac{|\Pi - \Pi^h|}{\Pi} \times 100; \quad h = \{C^2, O(1)\} \quad (3.38a)$$

$$\Pi(\mathbf{u}^\zeta) = \int_{\Omega^\zeta} U^\zeta(\boldsymbol{\varepsilon}^\zeta) d\Omega = \int_{\Omega^\zeta} \frac{1}{2} \boldsymbol{\sigma}^\zeta : \boldsymbol{\varepsilon}^\zeta d\Omega \quad (3.38b)$$

where $U^\zeta(\boldsymbol{\varepsilon}^\zeta)$ is the strain energy density, and

2. the L_2 norm of error in the von Mises stress σ_{vM} normalized with respect to the maximum L_2 norm of the von Mises stress on DNS cell:

$$|\Delta\sigma| = \left(\frac{\|\mathbf{e}_{\sigma_{vM}}^h\|_{L_2}^2}{\tilde{N} \max_{I=1:\tilde{N}} \{\|\sigma_{vM}\|_{L_2, \Theta_I}^2\}} \right)^{1/2} \times 100 = \left(\frac{\int_{\Omega} (\sigma_{vM} - \sigma_{vM}^h)^T (\sigma_{vM} - \sigma_{vM}^h) d\Omega}{\tilde{N} \max_{I=1:\tilde{N}} \left\{ \int_{\Theta_I} \sigma_{vM}^T \sigma_{vM} d\Theta_I \right\}} \right)^{1/2} \times 100 \quad (3.39)$$

where \tilde{N} is the total number of cells in the physical (DNS) domain Ω^ζ .

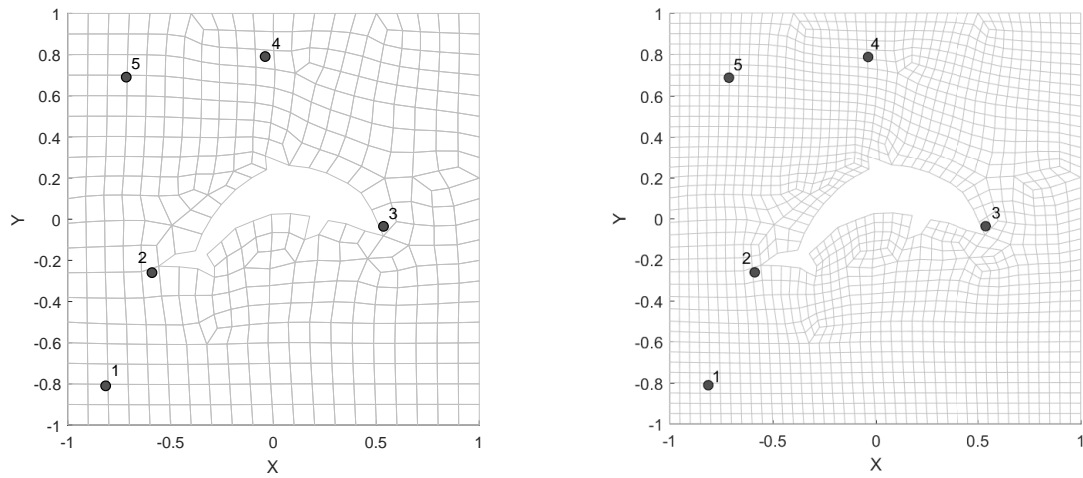
The values of these measures are summarized in Tables 3.4 and 3.5 for problems A and B, respectively. We observe that at the global level both C^2 formulations and $O(1)$ give satisfactory results (both measures are below 5%). However, C^2 formulation is more accurate than $O(1)$ by 15-20%, for the finer coarse-scale meshes. We also observe that the two C^2 formulations differ only by less than 2%. The latter makes the tensor-product based NLQ approach computationally more attractive.

Table 3.4: Relative error in global measures for problem A.

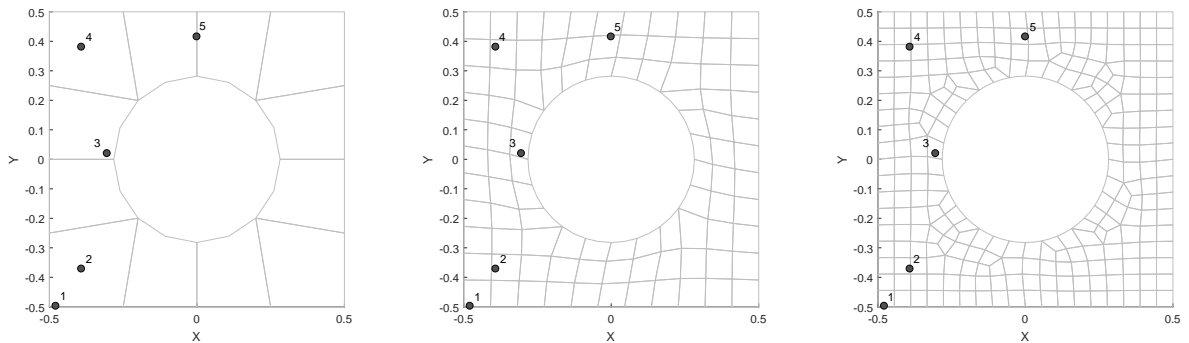
(%)	mesh A1			mesh A2		
	C_{ex}^2	C_{tb}^2	$O(1)$	C_{ex}^2	C_{tb}^2	$O(1)$
$ \Delta\Pi $	4.210	4.448	4.766	3.495	3.574	4.130
$ \Delta\sigma $	2.803	2.826	3.615	2.702	2.664	3.179

Table 3.5: Relative error in global measures for problem B.

(%)	mesh B1			mesh B2			mesh B3		
	C_{ex}^2	C_{tb}^2	$O(1)$	C_{ex}^2	C_{tb}^2	$O(1)$	C_{ex}^2	C_{tb}^2	$O(1)$
$ \Delta\Pi $	8.754	9.068	8.967	2.878	2.241	3.972	2.176	1.539	3.927
$ \Delta\sigma $	8.217	8.287	19.157	4.261	4.263	8.435	4.156	4.053	6.172

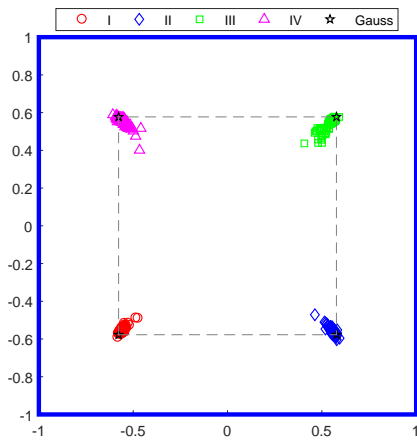


(a) Coarse-scale mesh A1 of 407 Q8 elements. (b) Coarse-scale mesh A2 of 1628 Q8 elements.

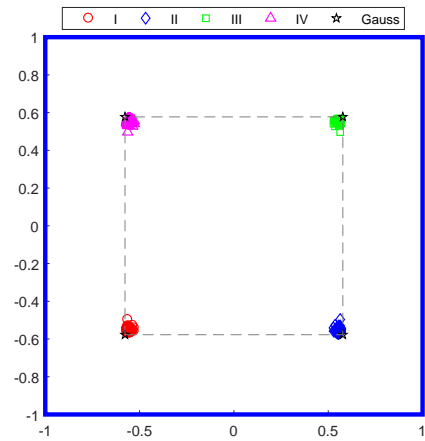
 Figure 3.17: Coarse-scale Q8 meshes for C^2 and $O(1)$ formulations for problem A. Also marked are the unit cells over which detailed stresses are compared.


(a) Coarse-scale mesh B1 of 12 Q8 elements. (b) Coarse-scale mesh B2 of 96 Q8 elements. (c) Coarse-scale mesh B3 of 256 Q8 elements.

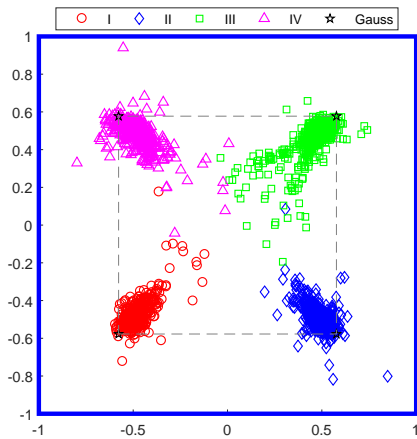
 Figure 3.18: Coarse-scale Q8 meshes for C^2 and $O(1)$ formulations for problem B. Also marked are the unit cells over which detailed stresses are compared.



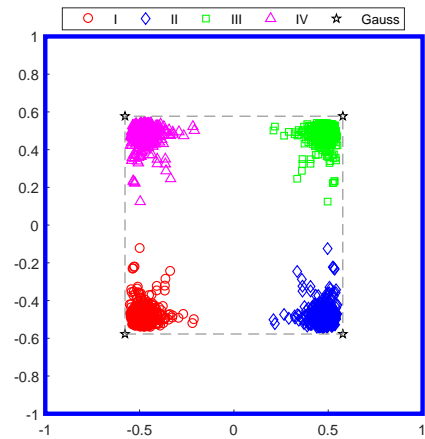
(a) Exact NLQ for mesh A1.



(b) Tensor-product based NLQ for mesh A1.

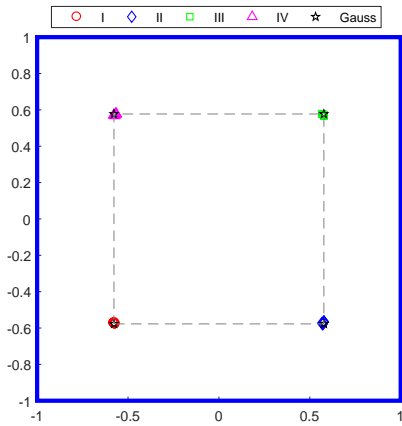


(c) Exact NLQ for mesh A2.

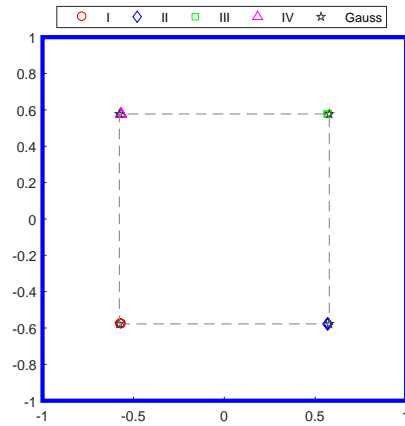


(d) Tensor-product based NLQ for mesh A2.

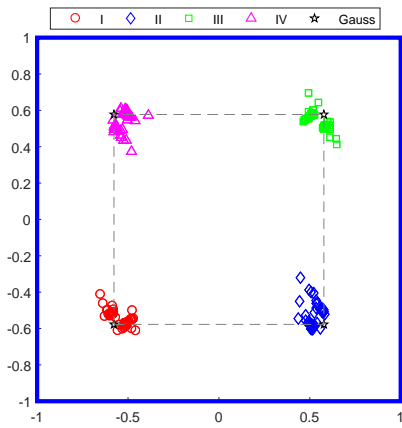
Figure 3.19: Location of nonlocal quadrature points (I-IV) for the coarse-scale meshes of problem A, Fig. 3.17.



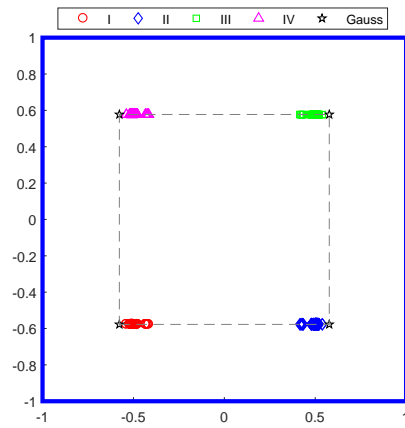
(a) Exact NLQ for mesh B1.



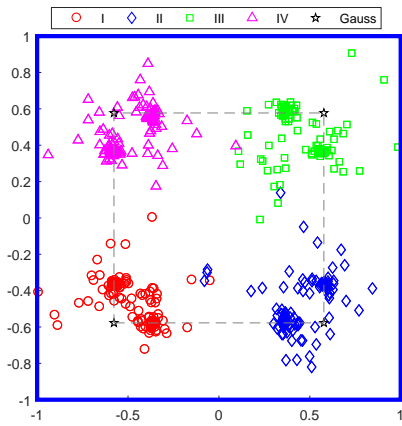
(b) Tensor-product based NLQ for mesh B1.



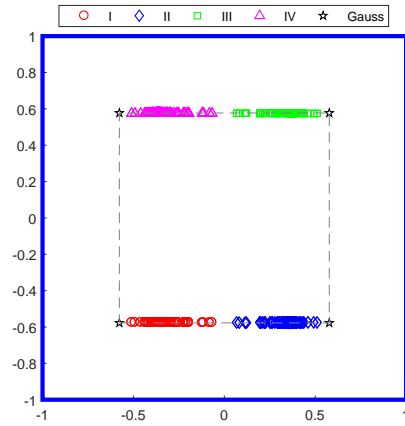
(c) Exact NLQ for mesh B2.



(d) Tensor-product based NLQ for mesh B2.



(e) Exact NLQ for mesh B3.



(f) Tensor-product based NLQ for mesh B3.

Figure 3.20: Location of nonlocal quadrature points (I-IV) for the coarse-scale meshes of problem B, Fig. 3.18.

3.7.2 Local error measures

The advantage of C^2 formulations is clearly demonstrated at the local level, when comparing the stress fields around individual unit cells located in the critical areas of high coarse-scale strain gradients.

Figs. 3.21-3.25 for problem A and Figs. 3.26-3.30 for problem B, show the distribution of the von Mises stress σ_{vM} over selected unit cells—Figs. 3.17 for problem A and Figs. 3.18 for problem B. It can be seen that the C^2 formulation is considerably more accurate than the O(1) formulation for unit cells positioned in the hot spots, that is the areas of high coarse-scale gradients.

Remark 1: In evaluating the global and local error measures, the von Mises stress is computed on a physical DNS microstructure cell. The von Mises stresses for the C^2 and O(1) formulations are interpolated over the physical DNS cell from the nonlocal quadrature points and the Gauss points, respectively. For the interpolation two issues need to be addressed: (i) first, identification of the nearest NLQ and Gauss points to the physical cell using *k-nearest neighbors algorithms*, and (ii) higher order interpolation between random data points. In the present thesis, both issues were addressed using the build-in functions `knnsearch` and `scatteredInterpolant` in MATLAB [64, 65].

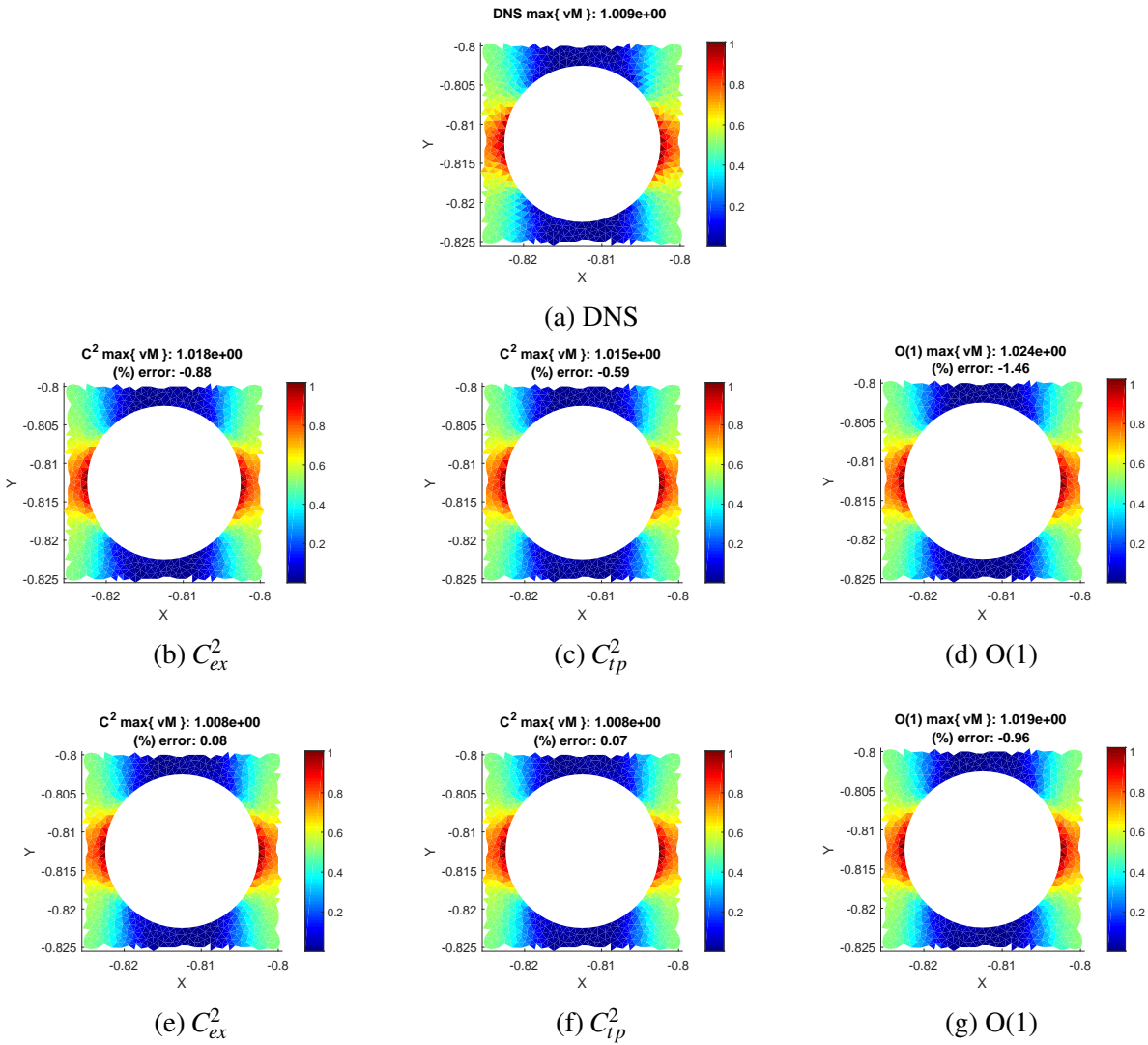


Figure 3.21: Total von Mises stress σ_{vM} on DNS cell 1 for problem A (a); C^2 and O(1) in (b)-(d) for mesh A1 and (e)-(g) for mesh A2.

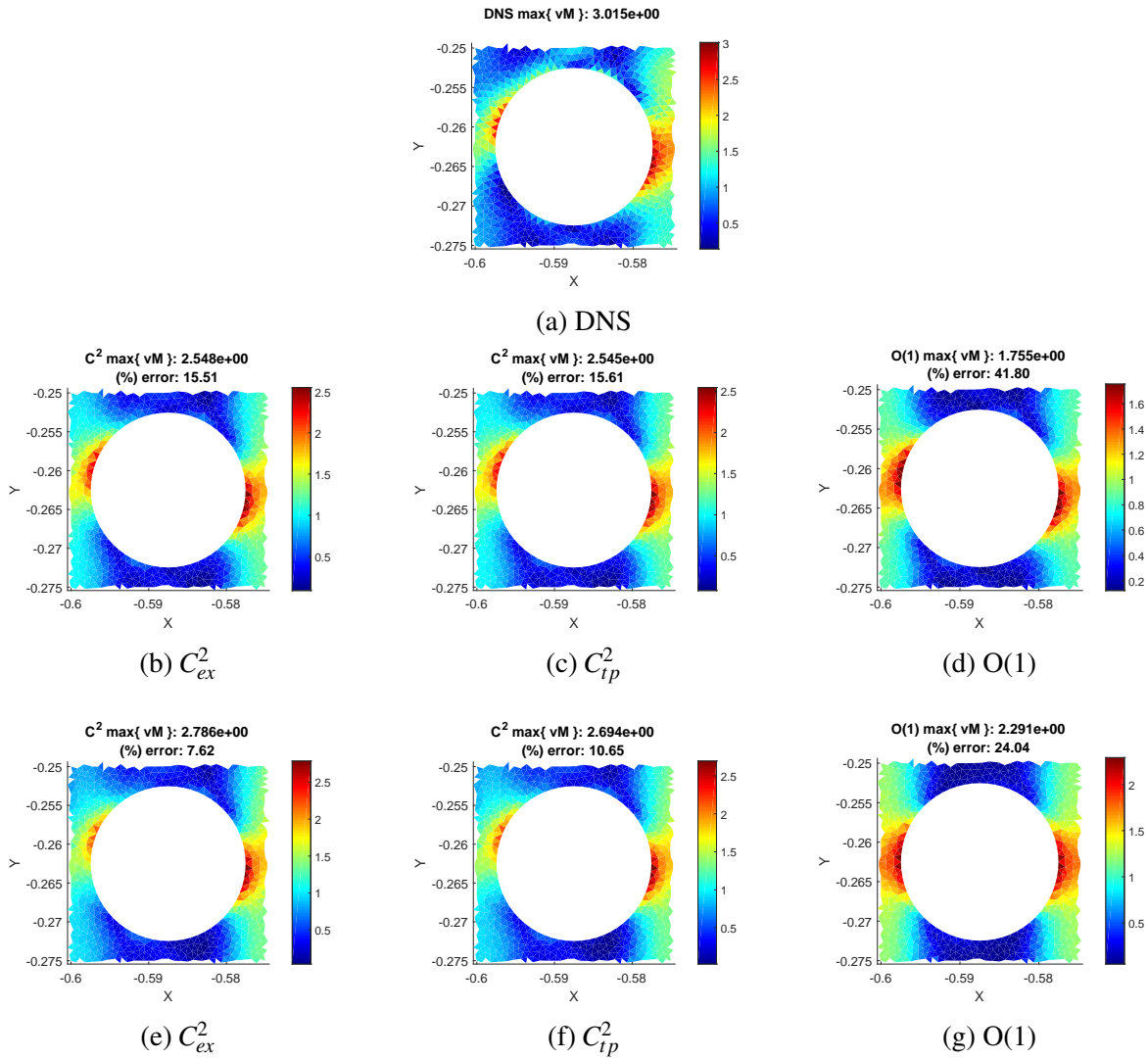


Figure 3.22: Total von Mises stress σ_{vM} on DNS cell 2 for problem A (a); C^2 and O(1) in (b)-(d) for mesh A1 and (e)-(g) for mesh A2.

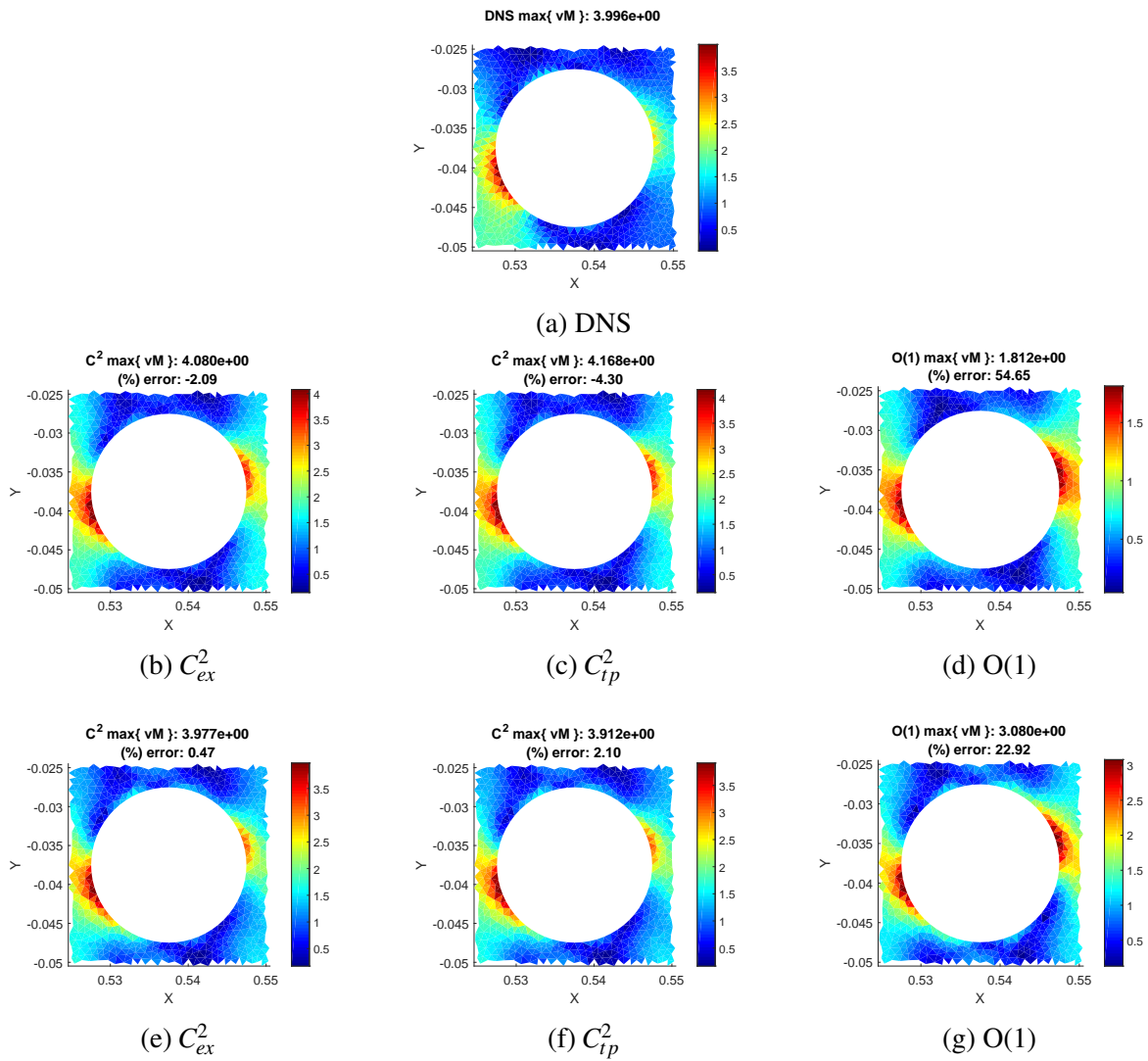


Figure 3.23: Total von Mises stress σ_{vM} on DNS cell 3 for problem A (a); C^2 and $O(1)$ in (b)-(d) for mesh A1 and (e)-(g) for mesh A2.

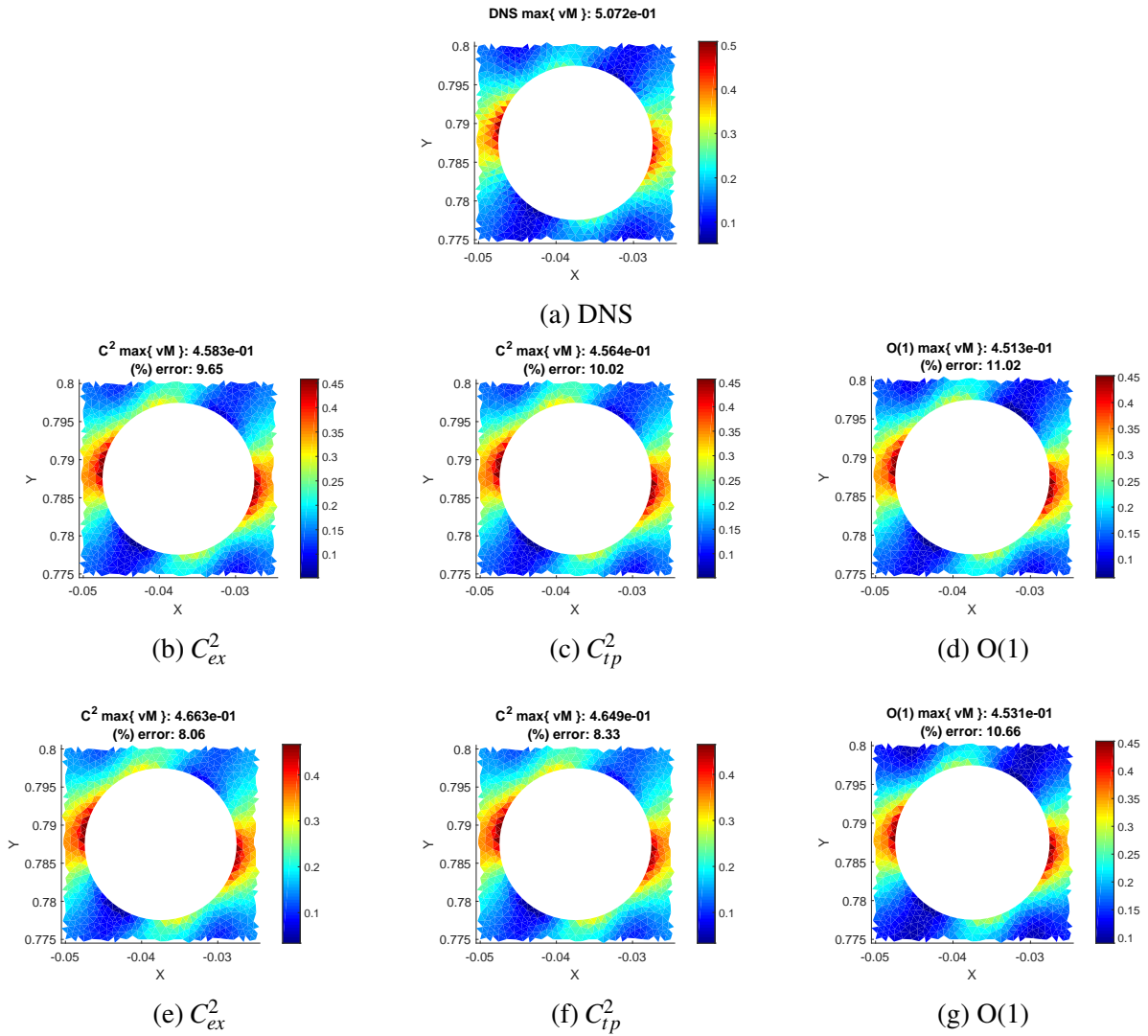


Figure 3.24: Total von Mises stress σ_{vM} on DNS cell 4 for problem A (a); C^2 and O(1) in (b)-(d) for mesh A1 and (e)-(g) for mesh A2.

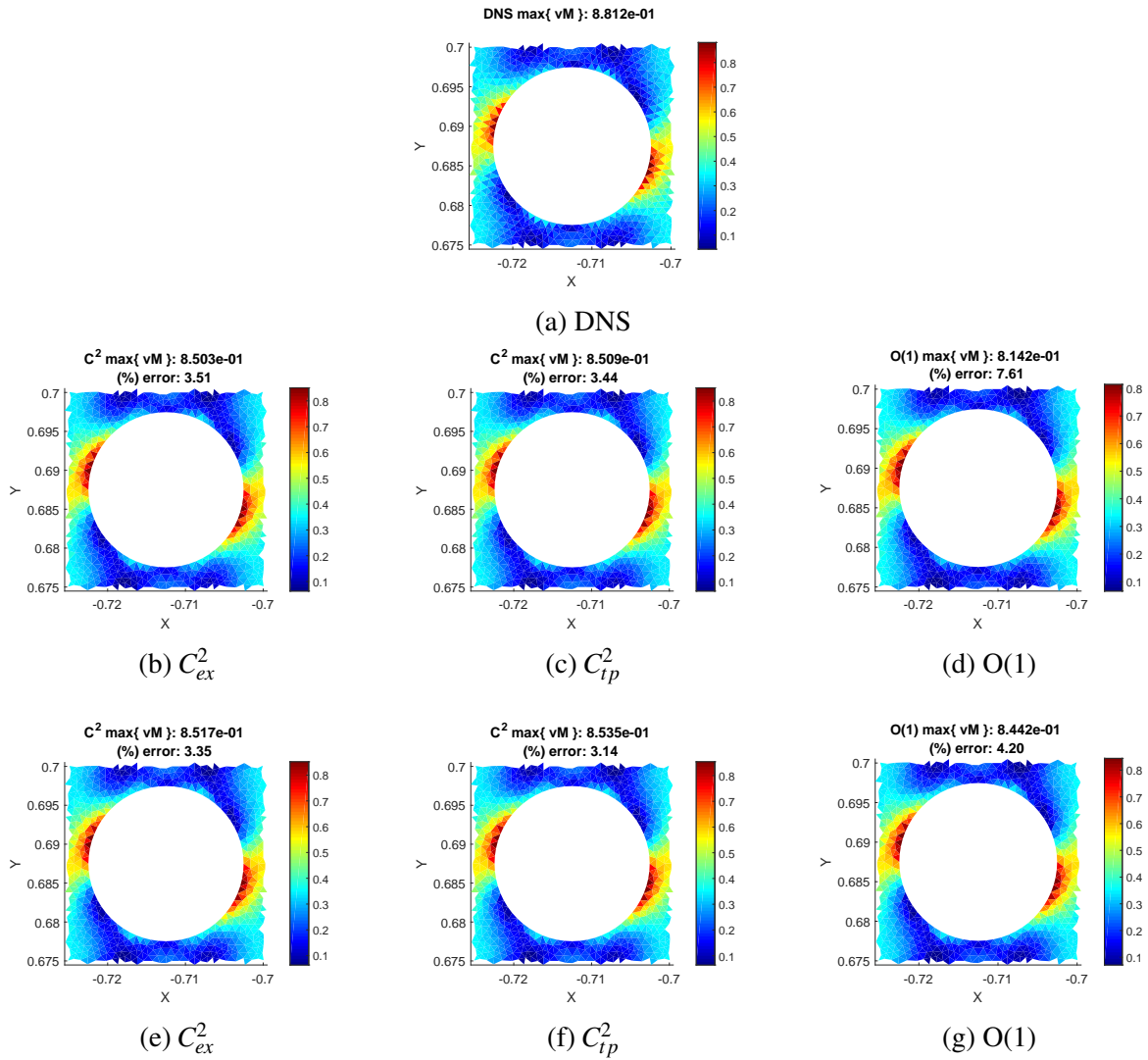


Figure 3.25: Total von Mises stress σ_{vM} on DNS cell 5 for problem A (a); C^2 and O(1) in (b)-(d) for mesh A1 and (e)-(g) for mesh A2.

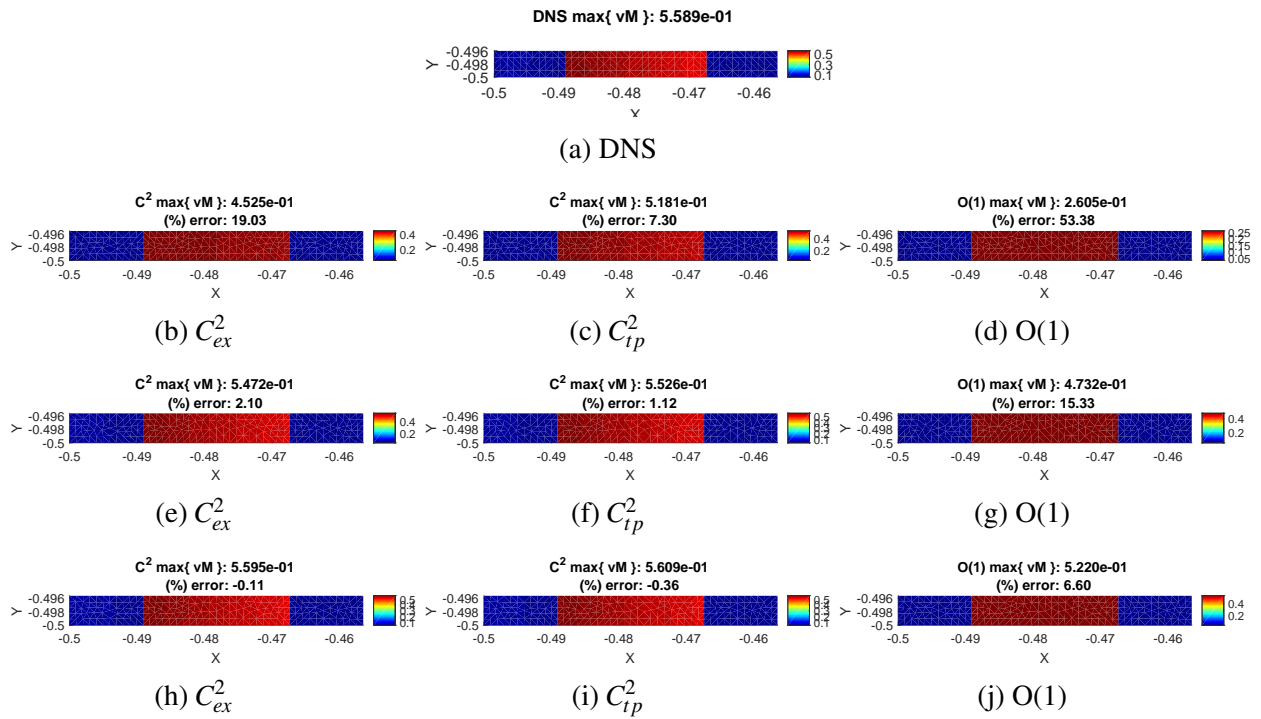


Figure 3.26: Total von Mises stress σ_{vM} on DNS cell 1 for problem B (a); C^2 and O(1) in (b)-(d) for mesh B1, (e)-(g) for mesh B2 and (h)-(j) for mesh B3.

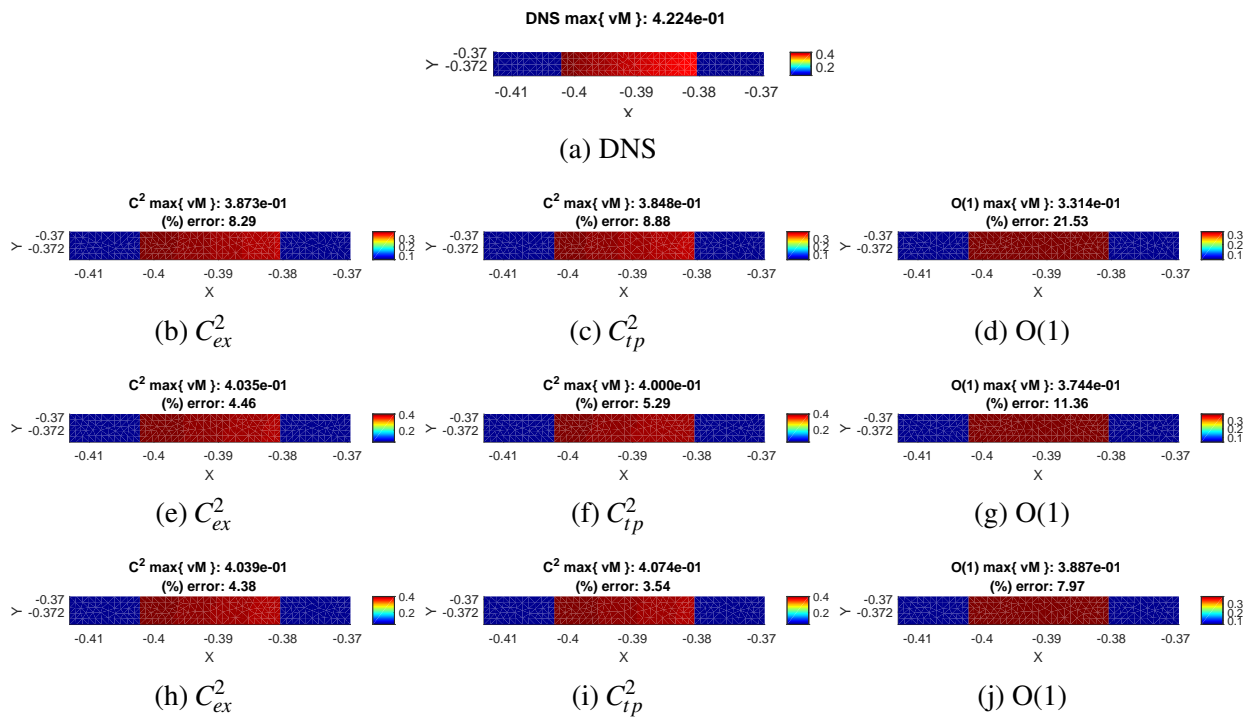


Figure 3.27: Total von Mises stress σ_{vM} on DNS cell 2 for problem B (a); C^2 and $O(1)$ in (b)-(d) for mesh B1, (e)-(g) for mesh B2 and (h)-(j) for mesh B3.

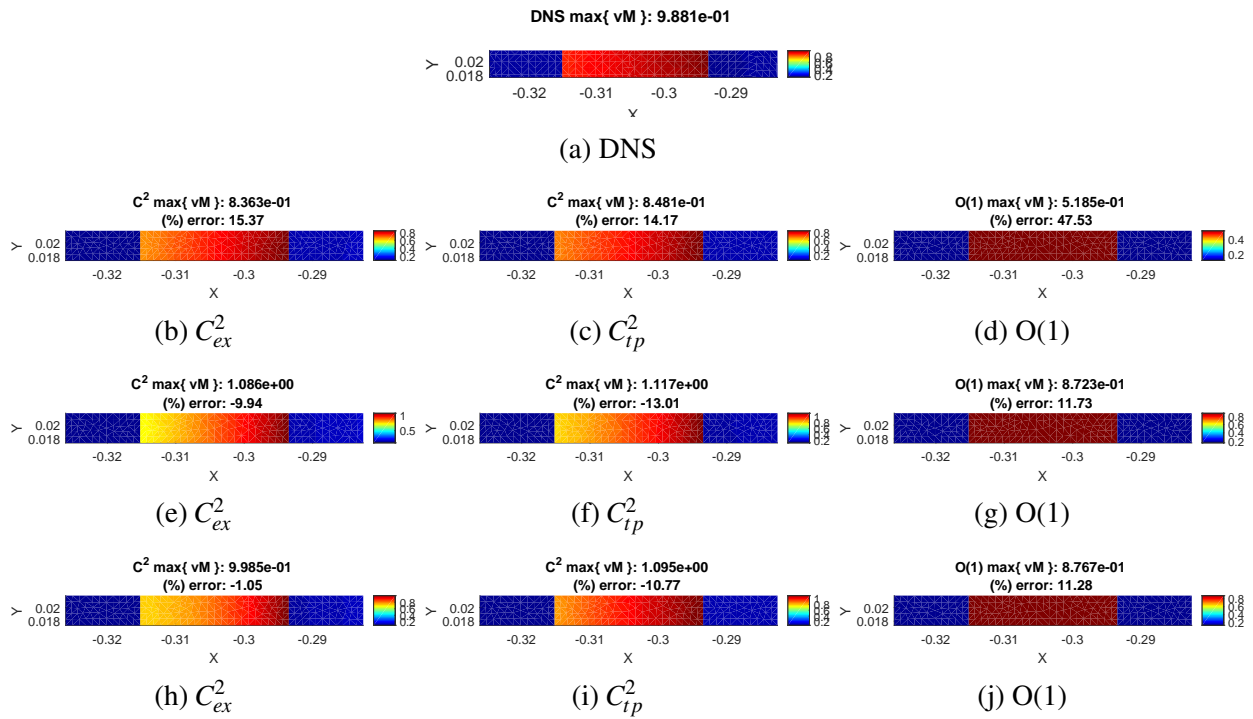


Figure 3.28: Total von Mises stress σ_{vM} on DNS cell 3 for problem B (a); C^2 and O(1) in (b)-(d) for mesh B1, (e)-(g) for mesh B2 and (h)-(j) for mesh B3.

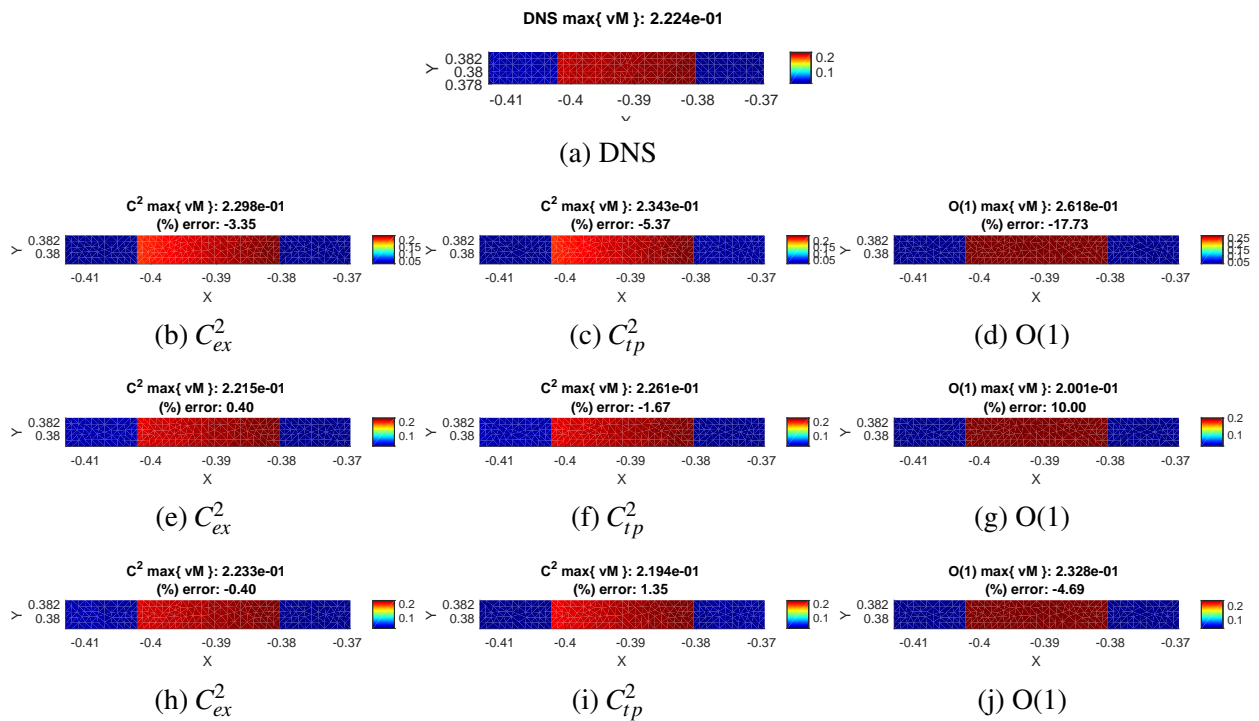


Figure 3.29: Total von Mises stress σ_{vM} on DNS cell 4 for problem B (a); C^2 and O(1) in (b)-(d) for mesh B1, (e)-(g) for mesh B2 and (h)-(j) for mesh B3.

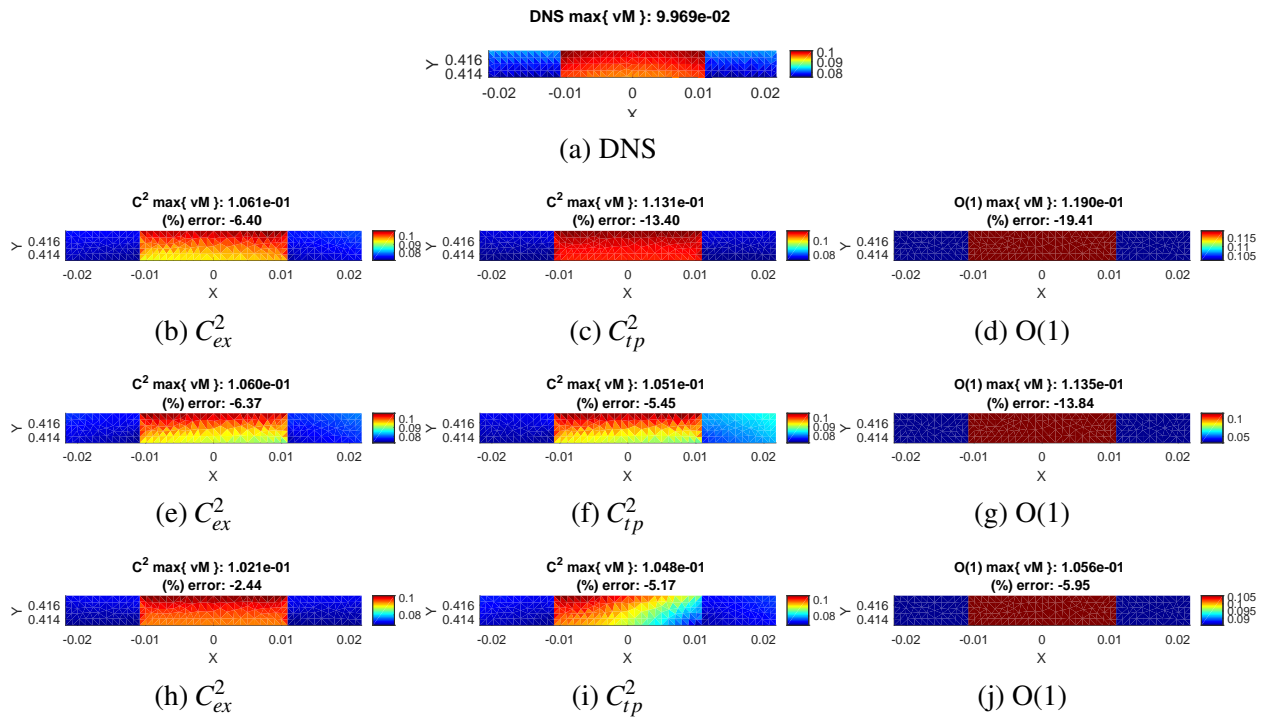


Figure 3.30: Total von Mises stress σ_{vM} on DNS cell 5 for problem B (a); C^2 and O(1) in (b)-(d) for mesh B1, (e)-(g) for mesh B2 and (h)-(j) for mesh B3.

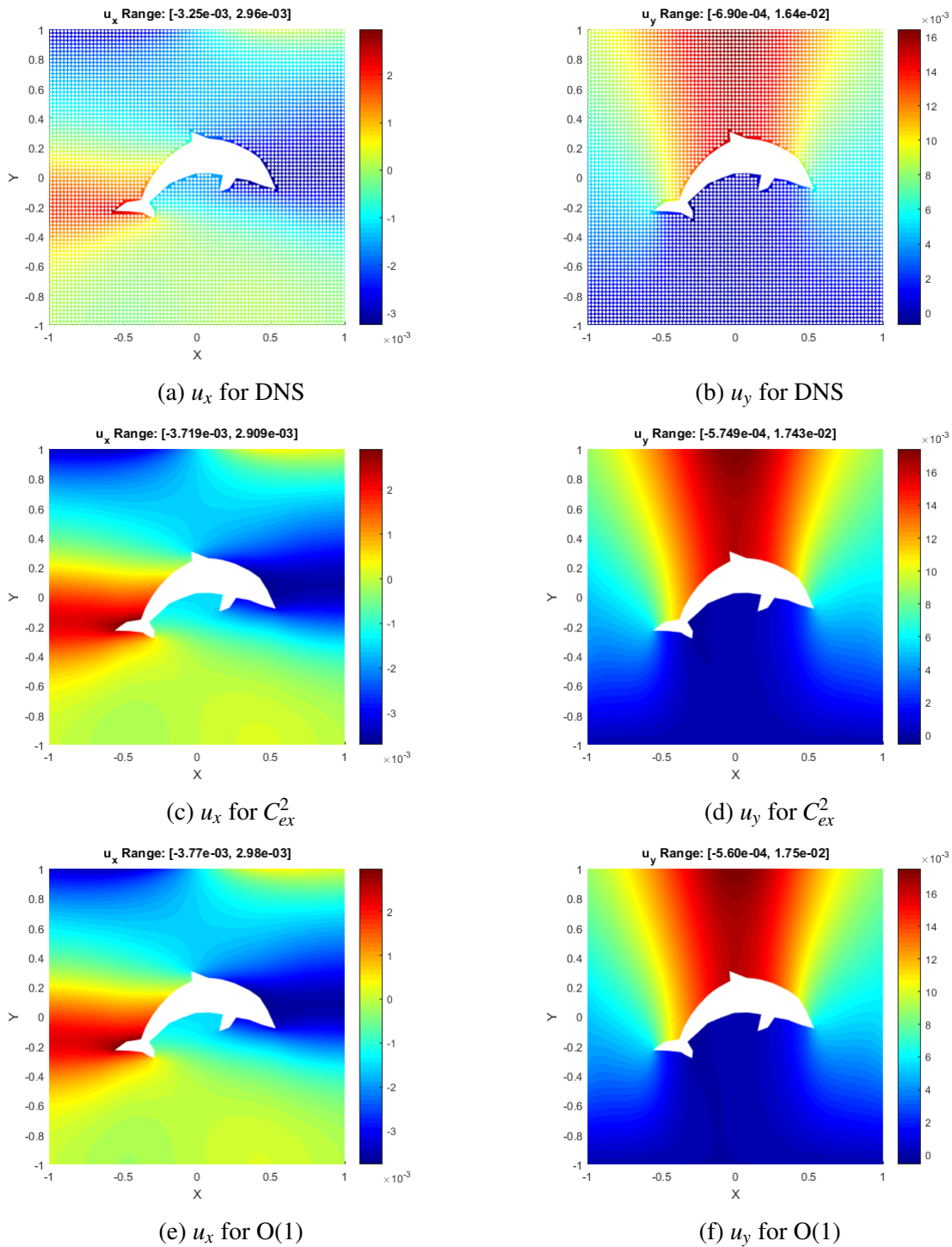


Figure 3.31: Displacement contours for problem A. (a)-(b) for DNS; (c)-(d) for C^2 from exact NLQ, mesh A2; (e)-(f) for O(1) homogenization, mesh A2.

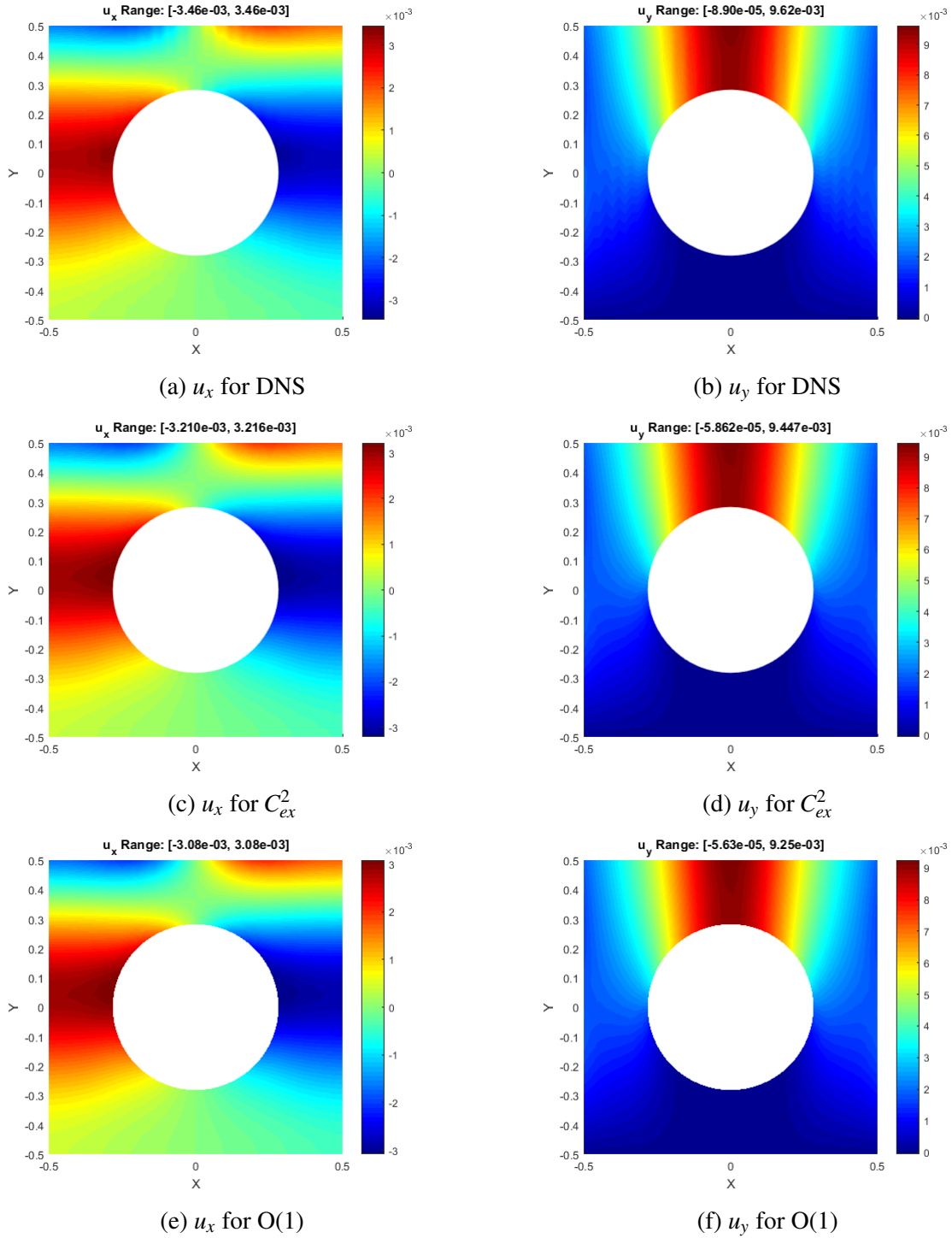


Figure 3.32: Displacement contours for problem B. (a)-(b) for DNS; (c)-(d) for C^2 from exact NLQ, mesh B3; (e)-(f) for O(1) homogenization, mesh B3.

This page intentionally left blank.

Chapter 4

Dispersive Computational Continua and Wave Propagation

4.1 Introduction

This chapter focuses on computational aspects of dispersive computational continua (C^2) formulation [19, 21]. The dispersive C^2 formulation is a multiscale approach that showed strikingly accurate dispersion curves. However, the seemingly theoretical advantage may be inconsequential due to tremendous computational cost involved. Unlike classical dispersive methods pioneered more than a half a century ago where the unit cell is quasi-static and provides effective mechanical and dispersive properties to the coarse-scale problem, the dispersive C^2 gives rise to transient problems at all scales and for all microphases involved. An efficient block time-integration scheme is proposed that takes advantage of the fact that the transient unit cell problems are not coupled to each other, but rather to a single coarse-scale finite element they are positioned in. We show that the computational cost of the method is comparable to the classical dispersive methods for short load durations [19].

4.2 Dispersive Computational Continua

4.2.1 The Initial-Boundary Value Problem

The *strong form* of the initial/boundary value problem is defined as follows:

Given body force \mathbf{b}^ζ , traction $\bar{\mathbf{T}}^\zeta$ on the Neumann boundary $\partial\Omega_X^{\prime\zeta}$, prescribed displacement $\bar{\mathbf{u}}_D^\zeta$ on the Dirichlet boundary $\partial\Omega_X^{\prime\prime\zeta}$, and initial displacement $\bar{\mathbf{u}}_0^\zeta$ and velocity $\dot{\bar{\mathbf{u}}}_0^\zeta$, find $\mathbf{u}^\zeta : \Omega_X^\zeta \times [0, T] \rightarrow \mathbb{R}$ such that:

$$\left\{ \begin{array}{l} \nabla_{\mathbf{X}} \cdot \boldsymbol{\sigma}^\zeta(\mathbf{X}, t) + \mathbf{b}^\zeta(\mathbf{X}, t) = \rho^\zeta \ddot{\mathbf{u}}^\zeta(\mathbf{X}, t), \quad \text{on } \Omega_X^\zeta \times]0, T[\end{array} \right. \quad (4.1a)$$

$$\left\{ \begin{array}{l} \boldsymbol{\varepsilon}^\zeta(\mathbf{X}, t) = \nabla_{\mathbf{X}}^{\text{Sym}} \mathbf{u}^\zeta(\mathbf{X}, t), \quad \text{on } \Omega_X^\zeta \times]0, T[\end{array} \right. \quad (4.1b)$$

$$\left\{ \begin{array}{l} \boldsymbol{\sigma}^\zeta(\mathbf{X}, t) \mathbf{n}^\zeta(\mathbf{X}) = \bar{\mathbf{T}}^\zeta(\mathbf{X}, t), \quad \text{on } \partial\Omega_X^{\prime\zeta} \times]0, T[\end{array} \right. \quad (4.1c)$$

$$\left\{ \begin{array}{l} \mathbf{u}^\zeta(\mathbf{X}, t) = \bar{\mathbf{u}}_D^\zeta(\mathbf{X}, t), \quad \text{on } \partial\Omega_X^{\prime\prime\zeta} \times]0, T[\end{array} \right. \quad (4.1d)$$

$$\left\{ \begin{array}{l} \mathbf{u}^\zeta(\mathbf{X}, 0) = \bar{\mathbf{u}}_0^\zeta(\mathbf{X}), \quad \mathbf{X} \in \Omega \end{array} \right. \quad (4.1e)$$

$$\left\{ \begin{array}{l} \dot{\mathbf{u}}^\zeta(\mathbf{X}, 0) = \dot{\bar{\mathbf{u}}}_0^\zeta(\mathbf{X}), \quad \mathbf{X} \in \Omega \end{array} \right. \quad (4.1f)$$

where $\boldsymbol{\sigma}^\zeta, \boldsymbol{\varepsilon}^\zeta, \mathbf{u}^\zeta, \rho^\zeta$ are the stress, strain, displacement and density, respectively; \mathbf{n}^ζ is the unit normal vector to the boundary; the superscript ζ denotes existence of fine-scale features; t is the time dimension and $T > 0$ is a future time instant; $\nabla_{\mathbf{X}}^{\text{Sym}}$ is the symmetric part of the gradient operator with respect to argument \mathbf{X} .

Following variational multiscale method [35] and the s-version of the finite element method [22], the displacement field \mathbf{u}^ζ in the composite domain is decomposed into a smooth coarse-scale part \mathbf{u}^C and a perturbation $\mathbf{u}^{(1)}$:

$$\mathbf{u}^\zeta(\hat{\mathbf{X}}_I, \chi, t) = \mathbf{u}^C(\hat{\mathbf{X}}_I, \chi, t) + \mathbf{u}^{(1)}(\hat{\mathbf{X}}_I, \chi, t) \quad (4.2)$$

subjected to periodic boundary conditions:

$$\mathbf{u}^{(1)}(\hat{\mathbf{X}}_I, \chi, t) = \mathbf{u}^{(1)}(\hat{\mathbf{X}}_I, \chi + \mathbf{c}, t) \quad (4.3)$$

where \mathbf{c} denotes the period.

Following (4.2), the strain field can be expressed as:

$$\varepsilon^\zeta(\hat{\mathbf{X}}_I, \chi, t) = \varepsilon^C(\hat{\mathbf{X}}_I, \chi, t) + \varepsilon^{(1)}(\hat{\mathbf{X}}_I, \chi, t) \quad (4.4)$$

where ε^C and $\varepsilon^{(1)}$ are the coarse and perturbation strain fields, respectively.

We consider linear elastic microconstituents obeying:

$$\sigma^\zeta(\hat{\mathbf{X}}_I, \chi, t) = L^\zeta(\chi) \varepsilon^\zeta(\hat{\mathbf{X}}_I, \chi, t) \quad (4.5)$$

where $L^\zeta(\chi)$ is the elastic constitutive tensor. Inserting (4.4) into (4.5) yields

$$\begin{aligned} \sigma^\zeta(\hat{\mathbf{X}}_I, \chi, t) &= L^\zeta(\chi) \varepsilon^C(\hat{\mathbf{X}}_I, \chi, t) + L^\zeta(\chi) \varepsilon^{(1)}(\hat{\mathbf{X}}_I, \chi, t) \\ &= \sigma^C(\hat{\mathbf{X}}_I, \chi, t) + \sigma^{(1)}(\hat{\mathbf{X}}_I, \chi, t) \end{aligned} \quad (4.6)$$

where σ^C and $\sigma^{(1)}$ are the coarse and perturbation stresses, respectively.

4.2.2 The weak form of the coarse-scale problem

The weak form of the coarse-scale problem is derived by first multiplying (4.1a) by a *coarse-scale test function* $\mathbf{w}^C(\mathbf{X}, t)$, integrating over the computational unit cell domain Ω_X and making use of the Green-Gauss theorem to obtain:

$$\int_{\Omega_X} (\mathbf{w}^C)^T \rho^\zeta(\chi) \ddot{\mathbf{u}}^\zeta(\mathbf{X}, t) d\Omega + \int_{\Omega_X} (\nabla_X^{\text{Sym}} \mathbf{w}^C)^T \boldsymbol{\sigma}^\zeta(\mathbf{X}, t) d\Omega = \int_{\partial\Omega_X'} (\mathbf{w}^C)^T \bar{\mathbf{T}}^\zeta d\Gamma + \int_{\Omega_X} (\mathbf{w}^C)^T \mathbf{b}^\zeta d\Omega \quad (4.7)$$

Employing the displacement decomposition (4.2) and the nonlocal quadrature scheme (2.4), the weak form of the coarse-scale problem is defined as follows:

Find $\mathbf{u}^C \in W_{\Omega_X}$ such that

$$\sum_{I=1}^{\hat{N}} \hat{\omega}_I \left(\int_{\Theta_{\hat{x}_I}} (\mathbf{w}^C)^T \rho^\zeta(\chi) \ddot{\mathbf{u}}^C(\hat{\mathbf{X}}_I, \chi, t) d\Theta + \int_{\Theta_{\hat{x}_I}} (\mathbf{w}^C)^T \rho^\zeta(\chi) \ddot{\mathbf{u}}^{(1)}(\hat{\mathbf{X}}_I, \chi, t) d\Theta \right. \\ \left. + \int_{\Theta_{\hat{x}_I}} (\nabla_X^{\text{Sym}} \mathbf{w}^C)^T \boldsymbol{\sigma}^\zeta(\hat{\mathbf{X}}_I, \chi, t) d\Theta \right) \quad (4.8) \\ = \int_{\partial\Omega_X'} (\mathbf{w}^C)^T \bar{\mathbf{T}}^\zeta d\Gamma + \int_{\Omega_X} (\mathbf{w}^C)^T \mathbf{b}^\zeta d\Omega$$

$\forall \mathbf{w}^C \in W_{\Omega_X}^0$, where $W_{\Omega_X} = \{ \mathbf{u}^C | \mathbf{u}^C \in H^1, \mathbf{u}^C = \bar{\mathbf{u}}_j^\zeta \text{ on } \partial\Omega_X^u \}$ and

$W_{\Omega_X}^0 = \{ \mathbf{w}^C | \mathbf{w}^C \in H^1, \mathbf{w}^C = \mathbf{0} \text{ on } \partial\Omega_X^u \}$.

4.2.3 The weak form of the fine-scale problem

The weak form of the unit cell problem is derived by first multiplying (4.1a) by a *fine-scale test function* $\mathbf{w}^{(1)}(\chi, t)$, integrating over the composite domain Ω_χ and making use of the Green-Gauss theorem to obtain:

$$\begin{aligned} & \int_{\Theta_{\hat{\chi}_I}} \left(\mathbf{w}^{(1)} \right)^T \rho^\zeta(\chi) \ddot{\mathbf{u}}^\zeta(\mathbf{X}, t) d\Theta + \int_{\Theta_{\hat{\chi}_I}} \left(\nabla_\chi^{\text{Sym}} \mathbf{w}^{(1)} \right)^T \boldsymbol{\sigma}^\zeta(\mathbf{X}, t) d\Theta \\ &= \int_{\partial\Theta_{\hat{\chi}_I}^\mu} \left(\mathbf{w}^{(1)} \right)^T \boldsymbol{\sigma}^\zeta(\mathbf{X}, t) \cdot \mathbf{n}^\Theta d\Gamma^\Theta + \int_{\Theta_{\hat{\chi}_I}} \left(\mathbf{w}^{(1)} \right)^T \mathbf{b}^\zeta d\Theta \end{aligned} \quad (4.9)$$

Due the displacement decomposition (4.2), the periodicity (4.3), and the additional boundary constraint (2.19), and employing (4.4) and (4.6), the weak form of the unit cell problem is defined as follows:

Find $\mathbf{u}^{(1)} \in W_{\Theta_{\hat{\chi}_I}}$ such that

$$\begin{aligned} & \int_{\Theta_{\hat{\chi}_I}} \left(\mathbf{w}^{(1)} \right)^T \rho^\zeta(\chi) \ddot{\mathbf{u}}^C(\hat{\mathbf{X}}_I, \chi, t) d\Theta + \int_{\Theta_{\hat{\chi}_I}} \left(\mathbf{w}^{(1)} \right)^T \rho^\zeta(\chi) \ddot{\mathbf{u}}^{(1)}(\hat{\mathbf{X}}_I, \chi, t) d\Theta \\ &+ \int_{\Theta_{\hat{\chi}_I}} \left(\nabla_\chi^{\text{Sym}} \mathbf{w}^{(1)} \right)^T L^\zeta(\chi) \boldsymbol{\varepsilon}^{(1)}(\hat{\mathbf{X}}_I, \chi, t) d\Theta \\ &= - \int_{\Theta_{\hat{\chi}_I}} \left(\nabla_\chi^{\text{Sym}} \mathbf{w}^{(1)} \right)^T L^\zeta(\chi) \boldsymbol{\varepsilon}^C(\hat{\mathbf{X}}_I, \chi, t) d\Theta + \int_{\Theta_{\hat{\chi}_I}} \left(\mathbf{w}^{(1)} \right)^T \mathbf{b}^\zeta d\Theta \end{aligned} \quad (4.10)$$

$\forall \mathbf{w}^{(1)} \in W_{\Theta_{\hat{\chi}_I}}^0$, where $W_{\Theta_{\hat{\chi}_I}} = \left\{ \mathbf{u}^{(1)} \mid \mathbf{u}^{(1)} \in H^1, \chi\text{-periodic on } \partial\Theta_{\hat{\chi}_I}^\mu \right\}$ and

$$W_{\Theta_{\hat{\chi}_I}}^0 = \left\{ \mathbf{w}^{(1)} \mid \mathbf{w}^{(1)} \in H^1, \int_{\partial\Theta_{\hat{\chi}_I}^j} \mathbf{w}^{(1)} d\Gamma^\Theta = 0 \text{ on } \partial\Theta_{\hat{\chi}_I}^j \right\} \text{ for } j = \{1, \dots, 4\}$$

where $\cup_{j=1}^4 \partial\Theta_{\hat{\mathbf{x}}_I}^j = \partial\Theta_{\hat{\mathbf{x}}_I}$ and $\partial\Theta_{\hat{\mathbf{x}}_I}^i \cap \partial\Theta_{\hat{\mathbf{x}}_I}^j = \emptyset \forall i \neq j$.

4.2.4 Discretization of the coarse-scale and perturbation problems

Galerkin discretization is considered for the trial $\mathbf{u}^{(1)}$ and test $\mathbf{w}^{(1)}$ functions of the perturbation displacement field at the element level

$$\mathbf{u}^{(1)}(\hat{\mathbf{X}}_I, \chi, t) \approx \mathbf{u}_e^{(1)}(\hat{\mathbf{X}}_I, \chi, t) = \mathbf{N}^F(\chi) \mathbf{d}_{I,e}^{(1)}(t) \quad (4.11a)$$

$$\mathbf{w}^{(1)}(\hat{\mathbf{X}}_I, \chi, t) \approx \mathbf{w}_e^{(1)}(\hat{\mathbf{X}}_I, \chi, t) = \mathbf{N}^F(\chi) \mathbf{c}_{I,e}^{(1)}(t) \quad (4.11b)$$

where $\chi \in \Theta_{\hat{\mathbf{x}}_I}^e$, and for conciseness we denote $\mathbf{d}_{I,e}^{(1)}(t) \equiv \mathbf{d}_e^{(1)}(\hat{\mathbf{X}}_I, t)$, $\mathbf{c}_{I,e}^{(1)}(t) \equiv \mathbf{c}_e^{(1)}(\hat{\mathbf{X}}_I, t)$ the nodal values of the trial and test functions, respectively, of the e^{th} element in the I^{th} unit cell. $\mathbf{N}^F(\chi)$ denotes the unit cell shape functions defined on the unit cell domain $\Theta_{\hat{\mathbf{x}}_I}^e$.

Similarly, Galerkin discretization is employed for the trial \mathbf{u}^C and test \mathbf{w}^C functions of the coarse-scale displacement field

$$\mathbf{u}^C(\mathbf{X}, t) \approx \mathbf{u}_e^C(\mathbf{X}, t) = \mathbf{N}^C(\mathbf{X}) \mathbf{d}_e^C(t) \quad (4.12a)$$

$$\mathbf{w}^C(\mathbf{X}, t) \approx \mathbf{w}_e^C(\mathbf{X}, t) = \mathbf{N}^C(\mathbf{X}) \mathbf{c}_e^C(t) \quad (4.12b)$$

where $\mathbf{d}_e^C, \mathbf{c}_e^C$ denote the nodal values of the trial and test functions, respectively, of the e^{th} element in the coarse-scale domain $\Omega_{\hat{\mathbf{x}}_I}^e$, and $\mathbf{N}^C(\mathbf{X})$ denotes the coarse-scale element shape functions.

Discrete fine-scale problem

Substituting the discretizations (4.11a), (4.11b) and (4.12a), and (4.6) into the fine-scale weak form (4.10), and requiring the resulting system to hold for arbitrary coefficients $\mathbf{c}^{(1)}$, the following

matrix form of the unit cell problem is obtained:

$$\mathbf{M}_I^F \ddot{\mathbf{d}}_I^{(1)}(t) + \mathbf{K}_I^F \mathbf{d}_I^{(1)}(t) + \mathbf{M}_I^{FC} \ddot{\mathbf{d}}_e^C(t) + \mathbf{K}_I^{FC} \mathbf{d}_e^C(t) = \mathbf{F}_I^b(t) \quad (4.13)$$

where, $\ddot{\mathbf{d}}_I^{(1)}, \mathbf{d}_I^{(1)}$ are the acceleration and displacement vectors of the I^{th} unit cell and $\ddot{\mathbf{d}}_e^C, \mathbf{d}_e^C$ are the acceleration and displacement vectors of the coarse-scale element e which drive the I^{th} unit cell problem. The matrices in (4.13) are defined over the unit cell domain $\Theta_{\hat{\mathbf{X}}_I}$ and are expressed as follows:

$$\ddot{\mathbf{d}}_I^{(1)}(t) = \mathbb{A}_{e=1}^{n_{el}^{uc}} \ddot{\mathbf{d}}_{I,e}^{(1)}(t); \quad \mathbf{d}_I^{(1)}(t) = \mathbb{A}_{e=1}^{n_{el}^{uc}} \mathbf{d}_{I,e}^{(1)}(t) \quad (4.14)$$

$$\mathbf{M}_I^F = \mathbb{A}_{e=1}^{n_{el}^{uc}} \left(\int_{\Theta_e} (\mathbf{N}^F(\boldsymbol{\chi}))^T \rho^\zeta(\boldsymbol{\chi}) \mathbf{N}^F(\boldsymbol{\chi}) d\Theta \right) \quad (4.15a)$$

$$\mathbf{K}_I^F = \mathbb{A}_{e=1}^{n_{el}^{uc}} \left(\int_{\Theta_e} (\nabla_{\boldsymbol{\chi}}^{\text{Sym}} \mathbf{N}^F(\boldsymbol{\chi}))^T L_e^\zeta(\boldsymbol{\chi}) (\nabla_{\boldsymbol{\chi}}^{\text{Sym}} \mathbf{N}^F(\boldsymbol{\chi})) d\Theta \right) \quad (4.15b)$$

$$\mathbf{M}_I^{FC} = \mathbb{A}_{e=1}^{n_{el}^{uc}} \left(\int_{\Theta_e} (\mathbf{N}^F(\boldsymbol{\chi}))^T \rho^\zeta(\boldsymbol{\chi}) \mathbf{N}^C(\hat{\mathbf{X}}_I, \boldsymbol{\chi}) d\Theta \right) \quad (4.15c)$$

$$\mathbf{K}_I^{FC} = \mathbb{A}_{e=1}^{n_{el}^{uc}} \left(\int_{\Theta_e} (\nabla_{\boldsymbol{\chi}}^{\text{Sym}} \mathbf{N}^F(\boldsymbol{\chi}))^T L_e^\zeta(\boldsymbol{\chi}) (\nabla_{\boldsymbol{\chi}}^{\text{Sym}} \mathbf{N}^C(\hat{\mathbf{X}}_I, \boldsymbol{\chi})) d\Theta \right) \quad (4.15d)$$

$$\mathbf{F}_I^b = \mathbb{A}_{e=1}^{n_{el}^{uc}} \left(\int_{\Theta_e} (\mathbf{N}^F(\boldsymbol{\chi}))^T \mathbf{b}^\zeta d\Theta \right) \quad (4.15e)$$

where \mathbb{A} is the finite element assembly operator, the index e denotes element count in the unit cell mesh and n_{el}^{uc} denotes the total number of elements in the unit cell mesh.

Discrete coarse-scale problem

Inserting (4.12a,4.12b), (4.11a), into the coarse-scale weak form (4.8), using (4.6) and requiring the resulting system to hold for arbitrary coefficients \mathbf{c}^C , yields the discrete coarse-scale problem:

$$\bigg\langle \bigg\langle \sum_{e=1}^{n_{el}} \left\{ \mathbf{M}_e^C \ddot{\mathbf{d}}_e^C(t) + \mathbf{K}_e^C \mathbf{d}_e^C(t) + \mathbf{P}_e^{MCF}(t) + \mathbf{P}_e^{KCF}(t) + \mathbf{F}_e^{\partial C}(t) - \mathbf{F}_{b,e}^C(t) \right\} \bigg\rangle \bigg\rangle = \mathbf{0} \quad (4.16)$$

where n_{el} is the number of coarse-scale elements and the coarse-scale element matrices are defined as follows:

$$\mathbf{M}_e^C = \sum_{I=1}^{\hat{N}_e} \hat{\omega}_I \mathbf{M}_I^C \quad (4.17a)$$

$$\mathbf{M}_I^C = \int_{\Theta_{\hat{\mathbf{x}}_I}} \left(\mathbf{N}^C(\hat{\mathbf{x}}_I, \chi) \right)^T \rho^\zeta(\chi) \mathbf{N}^C(\hat{\mathbf{x}}_I, \chi) d\Theta \quad (4.17b)$$

$$\mathbf{K}_e^C = \sum_{I=1}^{\hat{N}_e} \hat{\omega}_I \mathbf{K}_I^C \quad (4.17c)$$

$$\mathbf{K}_I^C = \int_{\Theta_{\hat{\mathbf{x}}_I}} \left(\nabla_{\chi}^{\text{Sym}} \mathbf{N}^C(\hat{\mathbf{x}}_I, \chi) \right)^T L_e^\zeta(\chi) \left(\nabla_{\chi}^{\text{Sym}} \mathbf{N}^C(\hat{\mathbf{x}}_I, \chi) \right) d\Theta \quad (4.17d)$$

$$\mathbf{P}_e^{MCF}(t) = \sum_{I=1}^{\hat{N}_e} \hat{\omega}_I \mathbf{M}_I^{CF} \ddot{\mathbf{d}}_I^{(1)}(t) \quad (4.17e)$$

$$\mathbf{M}_I^{CF} = \int_{\Theta_{\hat{\mathbf{x}}_I}} \left(\mathbf{N}^C(\hat{\mathbf{x}}_I, \chi) \right)^T \rho^\zeta(\chi) \mathbf{N}^F(\chi) d\Theta \quad (4.17f)$$

$$\mathbf{P}_e^{KCF}(t) = \sum_{I=1}^{\hat{N}_e} \hat{\omega}_I \mathbf{K}_I^{CF} \mathbf{d}_I^{(1)}(t) \quad (4.17g)$$

$$\mathbf{K}_I^{CF} = \int_{\Theta_{\hat{\mathbf{X}}_I}} \left(\nabla_{\chi}^{\text{Sym}} \mathbf{N}^C(\hat{\mathbf{X}}_I, \chi) \right)^T L_e^{\zeta}(\chi) \left(\nabla_{\chi}^{\text{Sym}} \mathbf{N}^F(\chi) \right) d\Theta = \left(\mathbf{K}_I^{FC} \right)^T \quad (4.17h)$$

$$\mathbf{F}_e^{\partial C}(t) = \mathbf{M}_{es}^C \ddot{\mathbf{d}}_e^{\partial C}(t) + \mathbf{K}_{es}^C \mathbf{d}_e^{\partial C}(t) \quad (4.17i)$$

$$\mathbf{F}_{b,e}^C(t) = \int_{\Omega_X^e} \left(\mathbf{N}^C(\mathbf{X}) \right)^T \mathbf{b}^{\zeta} d\Omega^e \quad (4.17j)$$

where \hat{N}_e is the number of unit cells (nonlocal quadrature points) in a coarse-scale element, the index e denotes count of elements in the coarse-scale mesh, $\ddot{\mathbf{d}}_e^{\partial C}$, $\mathbf{d}_e^{\partial C}$ are the acceleration and displacement vectors, respectively, of the degrees-of-freedom (DOFs) corresponding to the Dirichlet boundary conditions (4.1d).

The contributions from the underlying unit cells come from the matrices $\mathbf{M}_I^C, \mathbf{M}_I^{CF}, \mathbf{K}_I^C, \mathbf{K}_I^{CF}$.

4.3 Solution of the coupled transient-transient system

From eq. (4.13) it can be seen that unit cells are uncoupled from each other; their solution depends only on the coarse-scale problem quantities of the coarse-scale element they are associated with. Moreover, it is possible to derive an explicit expression linking kinematic quantities of the coarse-scale problem and those of perturbation problem. This can be accomplished through appropriate time integration and condensation of the perturbation problem on the coarse-scale element level. This procedure is summarized below:

- i Select the time integration schemes for the perturbation and the coarse-scale problems.
- ii Solve the perturbation problem (4.13) at the time instant t_{n+1} .
Express the unit cell acceleration at time instant t_{n+1} in terms of coarse-scale solution at t_{n+1} (see eqs. (4.24), (4.21a) and (4.21b), or 4.25).
- iii Substitute the solution expression of the unit cell problem at t_{n+1} into the coarse-scale problem (4.16).
Express the perturbation and the coarse-scale quantities at time instant t_n .
- iv Solve the coarse-scale problem at time instant t_{n+1}
- v Substitute the solution of the coarse-scale problem into the fine scale problem to obtain the perturbation solution at t_{n+1}

4.3.1 The unit cell problem

For the semi-discretization in time of the perturbation problem, the Newmark time integration scheme [36] is selected

$$\mathbf{d}_{I,n+1}^{(1)} = \tilde{\mathbf{d}}_{I,n+1}^{(1)} + \beta \Delta t^2 \ddot{\mathbf{d}}_{I,n+1}^{(1)} \quad (4.18a)$$

$$\dot{\mathbf{d}}_{I,n+1}^{(1)} = \tilde{\dot{\mathbf{d}}}_{I,n+1}^{(1)} + \gamma \Delta t \ddot{\mathbf{d}}_{I,n+1}^{(1)} \quad (4.18b)$$

where β, γ are model parameters, Δt is the time step and the contributions from the previous time step t_n arising from:

$$\tilde{\mathbf{d}}_{I,n+1}^{(1)} = \mathbf{d}_{I,n}^{(1)} + \Delta t \dot{\mathbf{d}}_{I,n}^{(1)} + \frac{\Delta t^2}{2} (1 - 2\beta) \ddot{\mathbf{d}}_{I,n}^{(1)} \quad (4.19a)$$

$$\tilde{\dot{\mathbf{d}}}_{I,n+1}^{(1)} = \dot{\mathbf{d}}_{I,n}^{(1)} + \Delta t (1 - \gamma) \ddot{\mathbf{d}}_{I,n}^{(1)} \quad (4.19b)$$

At time step $t_{n+1} = t_0 + (n+1)dt$ the unit cell problem (4.13) is defined as follows:

$$\begin{aligned} \mathbf{M}_I^F \ddot{\mathbf{d}}_{I,n+1}^{(1)} + \mathbf{K}_I^F \mathbf{d}_{I,n+1}^{(1)} = & -\mathbf{M}_{free}^{FC,I} \ddot{\mathbf{d}}_{I,n+1}^C - \mathbf{K}_{free}^{FC,I} \mathbf{d}_{I,n+1}^C \\ & -\mathbf{M}_{\partial}^{FC,I} \ddot{\mathbf{d}}_{I,n+1}^{\partial C} - \mathbf{K}_{\partial}^{FC,I} \mathbf{d}_{I,n+1}^{\partial C} \end{aligned} \quad (4.20)$$

where, for conciseness, the following loading quantities are defined:

$$\mathbf{F}_{n+1}^{FC,I} = \mathbf{M}_{free}^{FC,I} \ddot{\mathbf{d}}_{I,n+1}^C + \mathbf{K}_{free}^{FC,I} \mathbf{d}_{I,n+1}^C \quad (4.21a)$$

$$\mathbf{F}_{n+1}^{\partial FC,I} = \mathbf{M}_{\partial}^{FC,I} \ddot{\mathbf{d}}_{I,n+1}^{\partial C} + \mathbf{K}_{\partial}^{FC,I} \mathbf{d}_{I,n+1}^{\partial C} \quad (4.21b)$$

The term $\mathbf{F}_{n+1}^{FC,I}$ refers to the contribution of the free DOFs in the coarse-scale problem to the I^h unit cell problem, while the term $\mathbf{F}_{n+1}^{\partial FC,I}$ refers to contribution of the corresponding boundary conditions.

Substituting (4.18a,4.18b) into (4.20) and rearranging the equation we get:

$$(\mathbf{M}_I^F + \beta \Delta t^2 \mathbf{K}_I^F) \ddot{\mathbf{d}}_{I,n+1}^{(1)} = -\mathbf{K}_I^F \tilde{\mathbf{d}}_{I,n+1}^{(1)} - \mathbf{F}_{n+1}^{FC,I} - \mathbf{F}_{n+1}^{\partial FC,I} \quad (4.22)$$

For conciseness, the following effective mass matrix is defined:

$$\mathbf{M}_{eff}^{F,I} = \mathbf{M}_I^F + \beta \Delta t^2 \mathbf{K}_I^F \quad (4.23)$$

Solving (4.22) for the fine-scale acceleration $\ddot{\mathbf{d}}_{I,n+1}^{(1)}$ yields

$$\ddot{\mathbf{d}}_{I,n+1}^{(1)} = -\mathbf{M}_{eff}^{-F,I} \left(\mathbf{K}_I^F \tilde{\mathbf{d}}_{I,n+1}^{(1)} + \mathbf{F}_{n+1}^{FC,I} + \mathbf{F}_{n+1}^{\partial FC,I} \right) \quad (4.24)$$

and the displacement and velocity vectors are updated according to (4.18a,4.18b).

If the loading terms (4.21a,4.21b) are inserted into (4.24), an alternative form for the unit cell accelerations is obtained:

$$\begin{aligned} \ddot{\mathbf{d}}_{I,n+1}^{(1)} = & -\mathbf{K}_I^{F0} \tilde{\mathbf{d}}_{I,n+1}^{(1)} - \mathbf{M}_I^{F1} \ddot{\mathbf{d}}_{I,n+1}^C - \mathbf{K}_I^{F1} \mathbf{d}_{I,n+1}^C \\ & - \mathbf{M}_I^{F2} \ddot{\mathbf{d}}_{I,n+1}^{\partial C} - \mathbf{K}_I^{F2} \mathbf{d}_{I,n+1}^{\partial C} \end{aligned} \quad (4.25)$$

where:

$$\mathbf{K}_I^{F0} = \mathbf{M}_{eff}^{-F,I} \mathbf{K}_I^F \quad (4.26a)$$

$$\mathbf{M}_I^{F1} = \mathbf{M}_{eff}^{-F,I} \mathbf{M}_{free}^{FC,I} \quad (4.26b)$$

$$\mathbf{K}_I^{F1} = \mathbf{M}_{eff}^{-F,I} \mathbf{K}_{free}^{FC,I} \quad (4.26c)$$

$$\mathbf{M}_I^{F2} = \mathbf{M}_{eff}^{-F,I} \mathbf{M}_{\partial}^{FC,I} \quad (4.26d)$$

$$\mathbf{K}_I^{F2} = \mathbf{M}_{eff}^{-F,I} \mathbf{K}_{\partial}^{FC,I} \quad (4.26e)$$

Relation (4.25) holds for every unit cell and will be inserted into the coarse-scale problem in the next section.

4.3.2 The coarse-scale problem

At the same time step $t_{n+1} = t_0 + (n + 1)dt$ as in the unit cell problem, the coarse-scale transient system (4.16) is defined as follows:

$$\bigtriangleup_{e=1}^{n_{el}} \left\{ \mathbf{M}_e^C \ddot{\mathbf{d}}_{e,n+1}^C + \mathbf{K}_e^C \mathbf{d}_{e,n+1}^C + \mathbf{P}_{e,n+1}^{M_{CF}} + \mathbf{P}_{e,n+1}^{K_{CF}} \right\} = \bigtriangleup_{e=1}^{n_{el}} \mathbf{F}_{b,e,n+1}^C - \bigtriangleup_{e=1}^{n_{el}} \mathbf{F}_{e,n+1}^{\partial C} \quad (4.27)$$

Coupling with the unit cell problem comes from the two terms:

$$\begin{aligned} \mathbf{P}_{e,n+1}^{M_{CF}} + \mathbf{P}_{e,n+1}^{K_{CF}} &= \sum_{I=1}^{\hat{N}_e} \hat{\omega}_I \left[\mathbf{M}_I^{CF} \ddot{\mathbf{d}}_{I,n+1}^{(1)} + \mathbf{K}_I^{CF} \mathbf{d}_{I,n+1}^{(1)} \right] \\ &= \sum_{I=1}^{\hat{N}_e} \hat{\omega}_I \left[\left(\mathbf{M}_I^{CF} + \beta \Delta t^2 \mathbf{K}_I^{CF} \right) \ddot{\mathbf{d}}_{I,n+1}^{(1)} + \mathbf{K}_I^{CF} \tilde{\mathbf{d}}_{I,n+1}^{(1)} \right] \end{aligned} \quad (4.28)$$

resulting from the Newmark time integration scheme (4.18a) for the unit cell problem. For convenience, the following effective matrix is defined

$$\mathbf{M}_{eff}^{CF,I} = \mathbf{M}_I^{CF} + \beta \Delta t^2 \mathbf{K}_I^{CF} \quad (4.29)$$

Finally, inserting the unit cell solution (4.25) into (4.28) and the resulting expression into (4.27) gives the final matrix form of the coarse-scale problem:

$$\begin{aligned}
 & \bigg\{ \sum_{I=1}^{\hat{N}_e} \hat{\omega}_I \left(\mathbf{M}_I^C - \mathbf{M}_{eff}^{CF,I} \mathbf{M}_I^{F1} \right) \ddot{\mathbf{d}}_{e,n+1}^C + \sum_{I=1}^{\hat{N}_e} \hat{\omega}_I \left(\mathbf{K}_I^C - \mathbf{M}_{eff}^{CF,I} \mathbf{K}_I^{F1} \right) \mathbf{d}_{e,n+1}^C \bigg\} \\
 &= - \bigg\{ \sum_{I=1}^{\hat{N}_e} \hat{\omega}_I \left(\mathbf{K}_I^{CF} - \mathbf{M}_{eff}^{CF,I} \mathbf{K}_I^{F0} \right) \tilde{\mathbf{d}}_{I,n+1}^{(1)} \bigg\}_e \\
 & - \bigg\{ \left(\mathbf{M}_{es}^C - \sum_{I=1}^{\hat{N}_e} \hat{\omega}_I \mathbf{M}_{eff}^{CF,I} \mathbf{M}_I^{F2} \right) \ddot{\mathbf{d}}_{e,n+1}^{\partial C} + \left(\mathbf{K}_{es}^C - \sum_{I=1}^{\hat{N}_e} \hat{\omega}_I \mathbf{M}_{eff}^{CF,I} \mathbf{K}_I^{F2} \right) \mathbf{d}_{e,n+1}^{\partial C} \bigg\} \\
 & + \mathbf{F}_{b,n+1}^C
 \end{aligned} \tag{4.30}$$

or in a more compact notation:

$$\tilde{\mathbf{M}}^C \ddot{\mathbf{d}}_{n+1}^C + \tilde{\mathbf{K}}^C \mathbf{d}_{n+1}^C = -\tilde{\mathbf{F}}_{n+1}^{(1)} - \tilde{\mathbf{F}}_{n+1}^{\partial C} + \mathbf{F}_{b,n+1}^C \tag{4.31}$$

where:

$$\tilde{\mathbf{M}}^C = \bigg\bigg\bigg\{ \tilde{\mathbf{M}}_e^C \bigg\}_{e=1}^{n_{el}} \tag{4.32a}$$

$$\tilde{\mathbf{M}}_e^C = \sum_{I=1}^{\hat{N}_e} \hat{\omega}_I \left(\mathbf{M}_I^C - \mathbf{M}_{eff}^{CF,I} \mathbf{M}_I^{F1} \right) \tag{4.32b}$$

$$\tilde{\mathbf{K}}^C = \bigg\bigg\bigg\{ \tilde{\mathbf{K}}_e^C \bigg\}_{e=1}^{n_{el}} \tag{4.32c}$$

$$\tilde{\mathbf{K}}_e^C = \sum_{I=1}^{\hat{N}_e} \hat{\omega}_I \left(\mathbf{K}_I^C - \mathbf{M}_{eff}^{CF,I} \mathbf{K}_I^{F1} \right) \tag{4.32d}$$

$$\tilde{\mathbf{F}}_{n+1}^{(1)} = \bigg\bigg\bigg\{ \tilde{\mathbf{F}}_e^{(1)} \bigg\}_{e=1}^{n_{el}} \tag{4.32e}$$

4.3. SOLUTION OF THE COUPLED TRANSIENT-TRANSIENT SYSTEM

$$\tilde{\mathbf{F}}_e^{(1)} = \sum_{I=1}^{\hat{N}_e} \hat{\omega}_I \left(\mathbf{K}_I^{CF} - \mathbf{M}_{eff}^{CF,I} \mathbf{K}_I^{F0} \right) \tilde{\mathbf{d}}_{I,n+1}^{(1)} \quad (4.32f)$$

$$\tilde{\mathbf{F}}_{n+1}^{\partial C} = \bigtriangleup_{e=1}^{n_{el}} \tilde{\mathbf{F}}_e^{\partial C} \quad (4.32g)$$

$$\tilde{\mathbf{F}}_e^{\partial C} = \mathbf{R}_{es}^M \ddot{\mathbf{d}}_{e,n+1}^{\partial C} + \mathbf{R}_{es}^K \mathbf{d}_{e,n+1}^{\partial C} \quad (4.32h)$$

$$\mathbf{R}_{es}^M = \left(\mathbf{M}_{es}^C - \sum_{I=1}^{\hat{N}_e} \hat{\omega}_I \mathbf{M}_{eff}^{CF,I} \mathbf{M}_I^{F2} \right) \quad (4.32i)$$

$$\mathbf{R}_{es}^K = \left(\mathbf{K}_{es}^C - \sum_{I=1}^{\hat{N}_e} \hat{\omega}_I \mathbf{M}_{eff}^{CF,I} \mathbf{K}_I^{F2} \right) \quad (4.32j)$$

For the coarse-scale problem, the Newmark integration scheme [36] is employed to semi-discretize (4.31) in time:

$$\mathbf{d}_{n+1}^C = \tilde{\mathbf{d}}_{n+1}^C + \beta \Delta t^2 \ddot{\mathbf{d}}_{n+1}^C \quad (4.33a)$$

$$\dot{\mathbf{d}}_{n+1}^C = \tilde{\dot{\mathbf{d}}}_{n+1}^C + \gamma \Delta t \ddot{\mathbf{d}}_{n+1}^C \quad (4.33b)$$

where β, γ are model parameters, Δt the time step, and the contributions from the previous time step t_n come from:

$$\tilde{\mathbf{d}}_{n+1}^C = \mathbf{d}_n^C + \Delta t \dot{\mathbf{d}}_n^C + \frac{\Delta t^2}{2} (1 - 2\beta) \ddot{\mathbf{d}}_n^C \quad (4.34a)$$

$$\tilde{\dot{\mathbf{d}}}_{n+1}^C = \dot{\mathbf{d}}_n^C + \Delta t (1 - \gamma) \ddot{\mathbf{d}}_n^C \quad (4.34b)$$

Inserting (4.33) into (4.31) yields:

$$\left(\tilde{\mathbf{M}}^C + \beta\Delta t^2\tilde{\mathbf{K}}^C\right)\ddot{\mathbf{d}}_{n+1}^C = -\tilde{\mathbf{K}}^C\tilde{\mathbf{d}}_{n+1}^C - \tilde{\mathbf{F}}_{n+1}^{(1)} - \tilde{\mathbf{F}}_{n+1}^{\partial C} + \mathbf{F}_{b,n+1}^C \quad (4.35)$$

The coarse-scale acceleration $\ddot{\mathbf{d}}_{n+1}^C$ at time step $n + 1$ is obtained by solving (4.35):

$$\ddot{\mathbf{d}}_{n+1}^C = -\mathbf{R}_{C1}\tilde{\mathbf{d}}_{n+1}^C - \mathbf{R}_{C2} - \mathbf{R}_{C3} + \mathbf{R}_{C4} \quad (4.36)$$

where:

$$\mathbf{R}_{C1} = \tilde{\mathbf{M}}_{eff}^{-C}\tilde{\mathbf{K}}^C \quad (4.37a)$$

$$\mathbf{R}_{C2} = \tilde{\mathbf{M}}_{eff}^{-C}\tilde{\mathbf{F}}_{n+1}^{(1)} \quad (4.37b)$$

$$\mathbf{R}_{C3} = \tilde{\mathbf{M}}_{eff}^{-C}\tilde{\mathbf{F}}_{n+1}^{\partial C} \quad (4.37c)$$

$$\mathbf{R}_{C4} = \tilde{\mathbf{M}}_{eff}^{-C}\mathbf{F}_{b,n+1}^C \quad (4.37d)$$

$$\tilde{\mathbf{M}}_{eff}^C = \tilde{\mathbf{M}}^C + \beta\Delta t^2\tilde{\mathbf{K}}^C \quad (4.37e)$$

The updated displacement and velocity vectors are computed according to eqs. (4.33). Following the solution for the coarse-scale quantities at time step $n + 1$, the fine-scale quantities have to be post-processed for the same time step. This is accomplished by substituting eqs. (4.36) and (4.33) into fine-scale accelerations (4.25) and then to fine-scale displacements and velocities (4.18a,4.18b).

4.3.3 Computational Cost

In this section we study the computational cost of the method in terms of the floating point operations (FLOPS) in the preprocessing stage and during the wave propagation. For simplicity, all matrices are assumed to be full, and direct solution techniques are used for all operations, such as

matrix-matrix or matrix-vector multiplications, as well as LU - decomposition.

The dispersive C^2 model is compared with the first-order homogenization theory with micro-inertia effects, $O(1) - mi$, [21], and a direct numerical simulation (DNS). The $O(1) - mi$ model belongs to the TSS category as stated in the introduction, formulating a quasi-dynamic unit cell problem. The basic idea of this approach is to first approximate the fine scale acceleration in terms of the spatial gradient of the coarse-scale acceleration and, subsequently, relate the coarse scale acceleration to the divergence of the coarse scale stress. By doing so, the dynamic unit cell problem can be approximated as a quasistatic problem.

For meaningful comparison against DNS and $O(1) - mi$, it is assumed that the unit cell is exactly the same for all three methods.

Let N_{el} be the total number of elements discretizing the coarse-scale domain, n_C^e the number of DOFs in a single coarse-scale element, n_C the total number of free DOFs for all N_{el} coarse-scale elements, and n_∂^e the number of DOFs in the coarse-scale elements with Dirichlet boundary conditions. Also, let n_F be the number of DOFs in a single unit cell, and N_T be the total time steps in a transient simulation.

The computational cost to solve the transient problem (4.25) for all time steps N_T and for all unit cells $N_{el} \times \hat{N}_e$ is:

$$T_F^{C2} = \frac{8}{3}n_F^3 + n_F^2 [1 + 4\hat{N}_e (n_C^e + n_\partial^e)] + N_T N_{el} \hat{N}_e [2n_F^2 + n_F (9 + 4n_C^e + 4n_\partial^e)] \quad (4.38)$$

Accordingly, the computational cost to solve the coarse-scale transient problem (4.36) for all time instances N_T is:

$$\begin{aligned} T_C^{C2} &= \frac{8}{3}n_C^3 + n_C^2 + N_T (6n_C^2 + 8n_C) \\ &+ N_T N_{el} n_C^e [\hat{N}_e (2n_F + 1) - 1] + \hat{N}_e n_C^e (2n_F^2 + n_F) \\ &+ \hat{N}_e n_F n_C^e + 4\hat{N}_e (n_C^e)^2 (1 + n_F) - 2(n_C^e)^2 \end{aligned} \quad (4.39)$$

The total cost for the dispersive C^2 model is obtained by adding the number of operations in eqs. (4.38,4.39).

The computational cost of the $O(1) - mi$ with n_C coarse-scale DOFs is:

$$T^{mi} = \frac{8}{3}n_C^3 + n_C^2 (2 + 4n_\partial^e) + N_T [2n_C^2 + 4n_C (2 + n_\partial^e)] \quad (4.40)$$

The computational cost of the DNS with n_R free DOFs is given by:

$$T^{DNS} = \frac{8}{3}n_R^3 + n_R^2 (1 + 4n_\partial^e) + N_T [2n_R^2 + 4n_R (2 + n_\partial^e)] \quad (4.41)$$

From the preceding analysis it can be seen that the computational cost depends on the n_C and n_F DOFs of the coarse-scale and unit cell domains, respectively, as well as on the total time steps N_T of the simulation. In order to compare the three models in terms of computational cost, it is convenient to consider two scenarios on the order of magnitude of these parameters:

- a. $n_C \sim n_F \sim n \gg 1$ and N_T finite
- b. $n_C \sim n_F \sim n$ and $N_T \gg 1$

Table 4.1 summarizes the prevailing order of computational cost. It can be seen that the computational cost of the dispersive C^2 model lies between that of the DNS and the $O(1) - mi$ for the case b, it is of the same order as $O(1) - mi$ for the case a, both being considerably faster than the DNS. Furthermore, as was shown in [21], the dispersive C^2 method matches perfectly the dispersion characteristic curve of heterogeneous materials with finite microstructure. Moreover, as will be demonstrated in the next section, the dispersive C^2 method is considerably more accurate than the $O(1) - mi$ model.

Table 4.1: Computational cost for scenarios a and b

Scenario	$T_{C2} \sim$	$T_{mi} \sim$	$T_R \sim$
a	$O(n^3)$	$O(n^3)$	$O(n^6)$
b	$O(N_T n^3)$	$O(N_T n^2)$	$O(N_T n^4)$

4.4 Model problem

4.4.1 Accuracy studies

In this section, the accuracy and stability of the dispersive C^2 is studied through a one-dimensional example; a rod of length L is subjected to a sinusoidal pulse $\bar{u}_{\partial L} \equiv u(0, t) = \sin(\omega t)$ at the left end, while the right end is free $u(L, t)$, as shown in Fig. 4.1. The excitation frequency ω corresponds to a wave length that is comparable to the unit cell size, to be discussed below; $t \in [0, T]$ is the simulation time of duration $T \in \mathbb{R}^+$

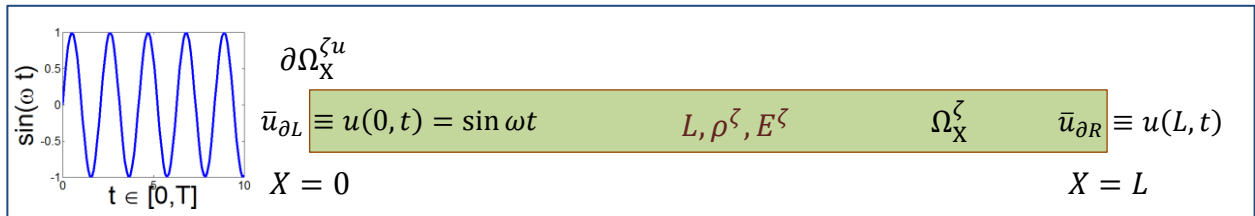


Figure 4.1: Sinusoidal pulse excitation of 1D rod.

The strong form of (4.1a-4.1f) reads:

$$(S) = \begin{cases} \frac{\partial \sigma^\zeta(X,t)}{\partial X} = \rho^\zeta \dot{u}^\zeta(X,t), & \text{on } \Omega_X^\zeta \\ \varepsilon^\zeta = \frac{\partial u^\zeta(X,t)}{\partial X}, & \text{on } \Omega_X^\zeta \\ \sigma^\zeta(L,t)n^\zeta = 0, & \text{on } X = L \\ u(0,t) \equiv \bar{u}_{\partial R} = \sin(\omega_k t), & \text{on } X = 0 \\ u(X,0) = 0, & \text{at } t = 0 \\ \dot{u}(X,0) = 0, & \text{at } t = 0 \end{cases} \quad (4.42)$$

where, zero initial conditions are considered.

The rod is made of periodic unit cell. The unit cell is schematically depicted in Fig. 4.2; it is composed of two different materials; a fiber phase of volume fraction v_f surrounded by a matrix phase of volume fraction v_m . The volume fraction of the matrix phase on the left of the fiber phase is v_{mL} . The density ρ^ζ and Young's modulus L^ζ are considered constant in each material phase, and can be expressed as:

$$\rho^\zeta(\chi) = \begin{cases} \rho_m & \chi \in (-\Theta/2, \chi_f) \\ \rho_f & \chi \in (\chi_f, \chi_m) \\ \rho_m & \chi \in (\chi_m, \Theta/2) \end{cases} \quad (4.43a) \quad L^\zeta(\chi) = \begin{cases} E_m & \chi \in (-\Theta/2, \chi_f) \\ E_f & \chi \in (\chi_f, \chi_m) \\ E_m & \chi \in (\chi_m, \Theta/2) \end{cases} \quad (4.43b)$$

The coarse-scale domain is discretized using N_{el} quadratic elements of length L_e . The non-local quadrature scheme (2.4), [26], consists of two non-local quadrature points (\hat{X}_I, W_I) at which two unit cells of size $\Theta \leq L_e$ are located. The material properties and geometrical parameters used for this example are summarized in Table 4.2.

The unit cell domain is also discretized using quadratic elements.

In order to subject the rod to high frequency excitation, it is necessary to evaluate the natural

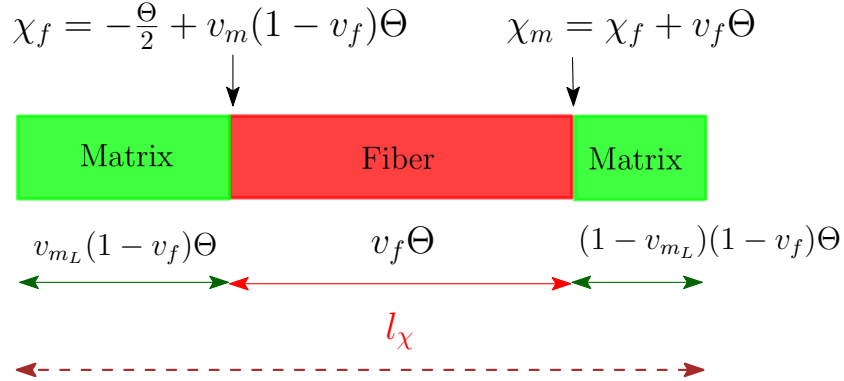


Figure 4.2: Geometry configuration of a unit cell with fiber inclusion.

Table 4.2: Material properties and model parameters for model problem

E_f	E_m	ρ_f	ρ_m	v_f	v_{m_L}	Θ	L_e	N_{el}
100	1	3	1	0.50	0.50	$[0, L_e]$	2.0	50

frequencies of the rod for a given ratio Θ/L_e . We consider the unit cell size equal to the length of the coarse-scale element $\Theta = L_e$, with material properties given in Table 4.2. The dominant natural frequencies are summarized in Table 4.3. The block-matrix form for which modal analysis was conducted is presented in the Appendix.

 Table 4.3: Wave lengths λ , wave numbers k , natural frequencies ω and the wave length to unit cell ratio λ/Θ , for the unit cell described in Table 4.2

λ	k	ω	λ/Θ
200	0.03142	0.0313	100
20	0.31416	0.3097	10
10	0.62832	0.6013	5
8	0.7854	0.7334	4
5	1.25664	1.0279	2.5
4.082	1.53938	1.0922	2.041
4	1.5708	3.1099	2
2	3.14159	3.50632	1

In the present example we consider the case $\Theta = L_e = 2$. Since we employ quadratic coarse-scale elements, two elements are necessary to reasonably approximate the sinusoidal wave, $\lambda =$

$2L_e$. From the results of modal analysis in Table 4.3, the closest sinusoidal wave to meet this ratio within the first frequency band is the one with frequency $\omega = 1.0922Hz$ or $\lambda = 4.082m$, as highlighted in Table 4.3. For more details the interested reader may refer to [21].

We consider the Newmark average acceleration scheme with parameters $\beta = 0.25, \gamma = 0.50$ and time step $\Delta t = 0.015$. The total time of simulation is $T = 200sec$.

The dispersive C^2 model is compared with the $O(1) - mi$, [27], and a direct numerical simulation (DNS). For the $O(1) - mi$ model, the same space discretization was used as for the coarse-scale domain of the C^2 model. For the DNS simulation, a total number of $N_{el} = 50$ unit cells was employed, equal to the number of coarse-scale elements in the dispersive C^2 model.

Figure 4.3 shows the displacement response at various time instances. It can be seen that the dispersive C^2 model is in good agreement with DNS, as opposed to the $O(1) - mi$.

The error in the dispersive C^2 model in comparison to the DNS is primarily due to the error in approximating sinusoidal wave with two quadratic elements.

4.4.2 Stability Analysis

For the solution procedure presented in the previous section, the Newmark time integration scheme is employed for both the unit cell and the coarse-scale problems. It is well known, [36], that the average acceleration scheme of Newmark method is unconditionally stable for values $\beta = 0.25, \gamma = 0.50$ of the model parameters. In this section we study whether this unconditional stability holds for the coupled Transient-Transient framework of the dispersive C^2 method. Towards this study, the formal procedure of stability analysis for second-order dynamical systems is employed, [36], according to which the difference equations is expressed in the form:

$$\mathbf{z}_{n+1} = \mathbf{A}\mathbf{z}_n \tag{4.44}$$

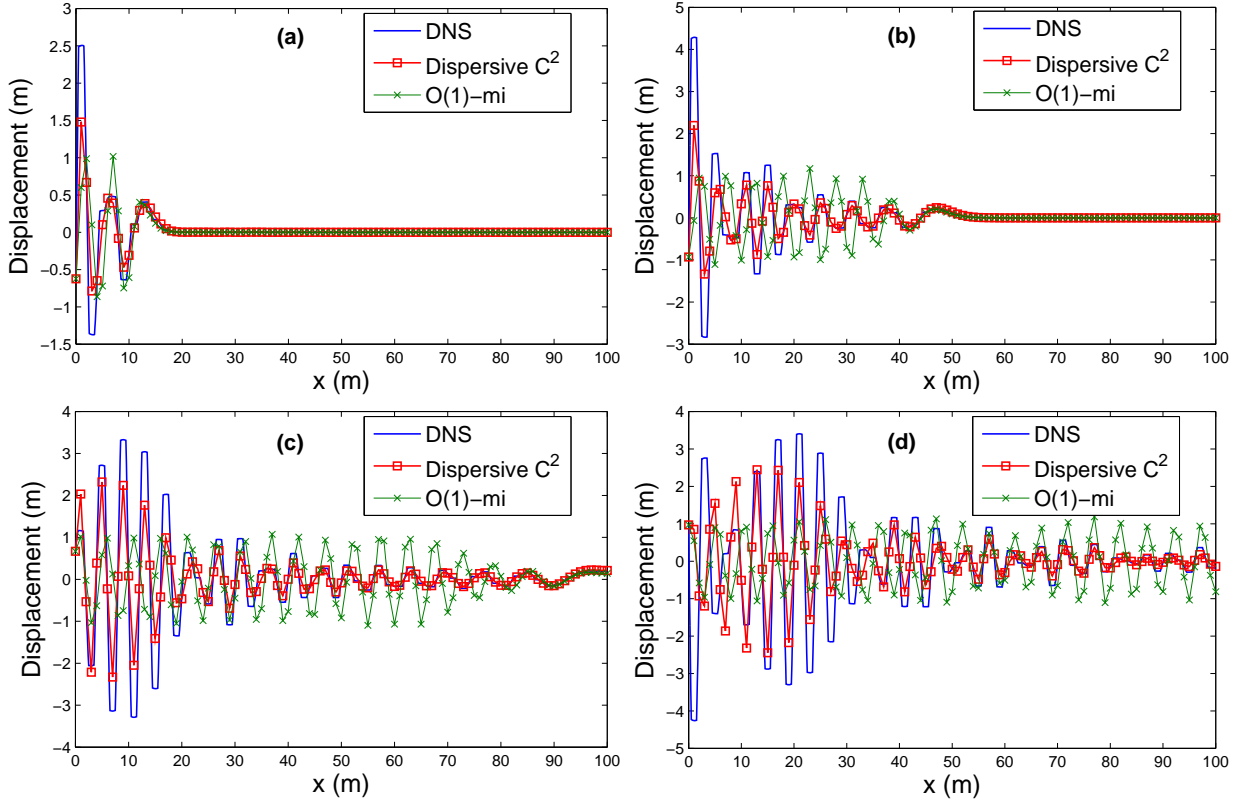


Figure 4.3: Wave propagation of the model problem at various time instances; **a** $t = 15$ sec, **b** $t = 50$ sec, **c** $t = 100$ sec, **d** $t = 180$ sec.

where \mathbf{A} is the amplification matrix to be defined below, and:

$$\mathbf{z}_{n+1} = \left\{ \mathbf{d}_{n+1}^C, \dot{\mathbf{d}}_{n+1}^C, \ddot{\mathbf{d}}_{n+1}^C, \mathbf{d}_{n+1}^{(1)}, \dot{\mathbf{d}}_{n+1}^{(1)}, \ddot{\mathbf{d}}_{n+1}^{(1)} \right\}^T \quad (4.45)$$

The kinematic quantities at time steps $n + 1$ and n are related according to:

$$\mathbf{z}_{n+1} = \boldsymbol{\mu} \mathbf{z}_n \quad (4.46)$$

where $\boldsymbol{\mu}$ are the eigenvalues of the amplification matrix \mathbf{A} :

$$(\mathbf{A} - \boldsymbol{\mu} \mathbf{I}) \mathbf{z}_n = \mathbf{0} \quad (4.47)$$

For stability it is required that:

$$|\mu| \leq 1 \quad (4.48)$$

The amplification matrix \mathbf{A} for the approach considered in Section 4.3, is defined based on eqs. (4.13),(4.31),(4.18),(4.33) as follows:

$$\begin{aligned} \tilde{\mathbf{K}}^C \mathbf{d}_{n+1}^C + \tilde{\mathbf{M}}^C \ddot{\mathbf{d}}_{n+1}^C &= -\hat{\mathbf{F}}^{(1)} \left(\mathbf{d}_n^{(1)} + \Delta t \dot{\mathbf{d}}_n^{(1)} + \Delta t^2 (0.5 - \beta) \ddot{\mathbf{d}}_n^{(1)} \right) \\ \mathbf{K}^{FC} \mathbf{d}_{n+1}^C + \mathbf{M}^{FC} \ddot{\mathbf{d}}_{n+1}^C + \mathbf{K}^F \mathbf{d}_{n+1}^{(1)} + \mathbf{M}^F \ddot{\mathbf{d}}_{n+1}^{(1)} &= \mathbb{O}_F \\ \mathbf{d}_{n+1}^C - \beta \Delta t^2 \ddot{\mathbf{d}}_{n+1}^C &= \mathbf{d}_n^C + \Delta t \dot{\mathbf{d}}_n^C + \frac{\Delta t^2}{2} (1 - 2\beta) \ddot{\mathbf{d}}_n^C \\ \dot{\mathbf{d}}_{n+1}^C - \gamma \Delta t \ddot{\mathbf{d}}_{n+1}^C &= \dot{\mathbf{d}}_n^C + \Delta t (1 - \gamma) \ddot{\mathbf{d}}_n^C \\ \mathbf{d}_{n+1}^{(1)} - \beta \Delta t^2 \ddot{\mathbf{d}}_{n+1}^{(1)} &= \mathbf{d}_n^{(1)} + \Delta t \dot{\mathbf{d}}_n^{(1)} + \frac{\Delta t^2}{2} (1 - 2\beta) \ddot{\mathbf{d}}_n^{(1)} \\ \dot{\mathbf{d}}_{n+1}^{(1)} - \gamma \Delta t \ddot{\mathbf{d}}_{n+1}^{(1)} &= \dot{\mathbf{d}}_n^{(1)} + \Delta t (1 - \gamma) \ddot{\mathbf{d}}_n^{(1)} \end{aligned} \quad (4.49)$$

or in compact notation:

$$\mathbf{A}_1 \mathbf{z}_{n+1} = \mathbf{A}_2 \mathbf{z}_n \quad (4.50a)$$

$$\mathbf{A} = \mathbf{A}_1^{-1} \mathbf{A}_2 \quad (4.50b)$$

where:

$$\mathbf{A}_1 = \begin{bmatrix} \tilde{\mathbf{K}}^C & \mathbb{O}_C & \tilde{\mathbf{M}}^C & \mathbb{O}_{CF} & \mathbb{O}_{CF} & \mathbb{O}_{CF} \\ \mathbf{K}^{FC} & \mathbb{O}_{FC} & \mathbf{M}^{FC} & \mathbf{K}^F & \mathbb{O}_F & \mathbf{M}^F \\ \mathbb{I}_C & \mathbb{O}_C & -\beta \Delta t^2 \mathbb{I}_C & \mathbb{O}_{CF} & \mathbb{O}_{CF} & \mathbb{O}_{CF} \\ \mathbb{O}_C & \mathbb{I}_C & -\gamma \Delta t \mathbb{I}_C & \mathbb{O}_{CF} & \mathbb{O}_{CF} & \mathbb{O}_{CF} \\ \mathbb{O}_{FC} & \mathbb{O}_{FC} & \mathbb{O}_{FC} & \mathbb{I}_F & \mathbb{O}_F & -\beta \Delta t^2 \mathbb{I}_F \\ \mathbb{O}_{FC} & \mathbb{O}_{FC} & \mathbb{O}_{FC} & \mathbb{O}_F & \mathbb{I}_F & -\gamma \Delta t \mathbb{I}_F \end{bmatrix} \quad (4.51a)$$

$$\mathbf{A}_2 = \begin{bmatrix} \mathbb{O}_C & \mathbb{O}_C & \mathbb{O}_C & -\hat{\mathbf{F}}^{(1)} & -\Delta t \hat{\mathbf{F}}^{(1)} & -\Delta t^2 (0.5 - \beta_F) \hat{\mathbf{F}}^{(1)} \\ \mathbb{O}_{FC} & \mathbb{O}_{FC} & \mathbb{O}_{FC} & \mathbb{O}_F & \mathbb{O}_F & \mathbb{O}_F \\ \mathbb{I}_C & \Delta t \mathbb{I}_C & \Delta t^2 (0.5 - \beta) \mathbb{I}_C & \mathbb{O}_{CF} & \mathbb{O}_{CF} & \mathbb{O}_{CF} \\ \mathbb{O}_C & \mathbb{I}_C & \Delta t (1 - \gamma) \mathbb{I}_C & \mathbb{O}_{CF} & \mathbb{O}_{CF} & \mathbb{O}_{CF} \\ \mathbb{O}_{FC} & \mathbb{O}_{FC} & \mathbb{O}_{FC} & \mathbb{I}_F & \Delta t \mathbb{I}_F & \Delta t^2 (0.5 - \beta) \mathbb{I}_F \\ \mathbb{O}_{FC} & \mathbb{O}_{FC} & \mathbb{O}_{FC} & \mathbb{O}_F & \mathbb{I}_F & \Delta t (1 - \gamma) \mathbb{I}_F \end{bmatrix} \quad (4.51b)$$

$$\hat{\mathbf{F}}^{(1)} = \bigtriangleup_{e=1}^{n_{el}} \left\{ \sum_{I=1}^{\hat{N}_e} \hat{\omega}_I \left(\mathbf{K}_I^{CF} - \mathbf{M}_{eff}^{CF,I} \mathbf{K}_I^{F0} \right) \right\} \quad (4.52)$$

$\tilde{\mathbf{K}}^C, \tilde{\mathbf{M}}^C$ are defined in (4.32), $\mathbf{K}^F, \mathbf{M}^F, \mathbf{K}^{FC}, \mathbf{M}^{FC}, \mathbf{d}^C, \mathbf{d}^{(1)}$ are defined in the Appendix, and $\mathbb{O}_C, \mathbb{O}_F, \mathbb{O}_{CF}, \mathbb{O}_{FC}$ are zero matrices and $\mathbb{I}_C, \mathbb{I}_F$ are identity matrices of appropriate dimensions.

As an example, for the 1D rod model using the average Newmark time integration scheme with $\beta = 0.25, \gamma = 0.50$ and $\Delta t = 0.015$, and material parameters in Table 4.2, the magnitude of the eigenvalues of the amplification matrix \mathbf{A} are plotted in Fig. 4.4. It can be seen that the eigenvalues fall within or on the unit circle.

Appendix: Monolithic form of the coupled system

The coupled problem consists of solving at every time step the coarse-scale problem (4.16) and the unit cell problem (4.13) for all the unit cells in the domain. In a monolithic matrix form this can be expressed as follows:

$$\begin{bmatrix} \mathbf{M}^F & \mathbf{M}^{FC} \\ \mathbf{M}^{CF} & \mathbf{M}^C \end{bmatrix} \begin{Bmatrix} \ddot{\mathbf{d}}^{(1)} \\ \ddot{\mathbf{d}}^C \end{Bmatrix} + \begin{bmatrix} \mathbf{K}^F & \mathbf{K}^{FC} \\ \mathbf{K}^{CF} & \mathbf{K}^C \end{bmatrix} \begin{Bmatrix} \mathbf{d}^{(1)} \\ \mathbf{d}^C \end{Bmatrix} = \begin{Bmatrix} \mathbf{F}^{(1)} \\ \mathbf{F}^C \end{Bmatrix} \quad (4.53)$$

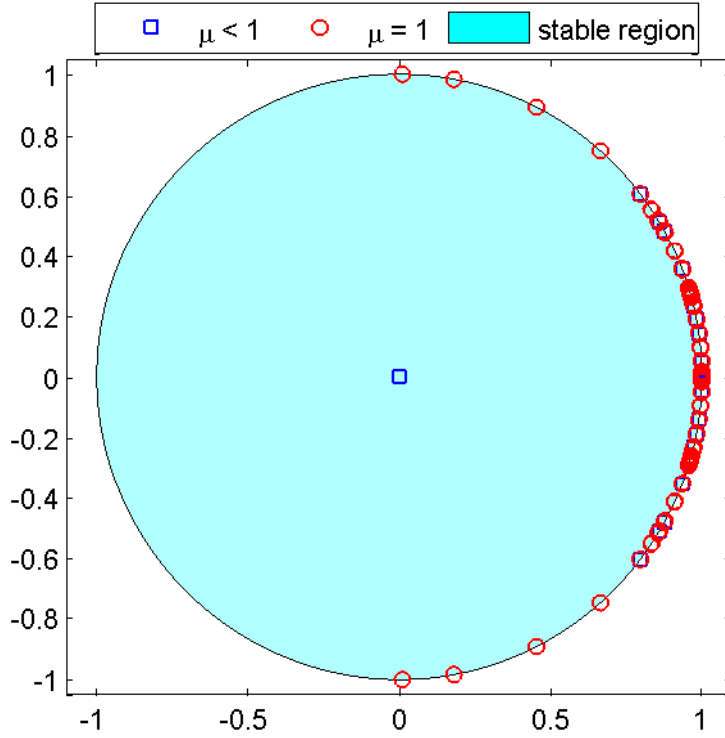


Figure 4.4: Eigenvalues chart for amplification matrix \mathbf{A} , for the model problem.

For simplicity, the following matrices can be defined:

$$\mathbf{M} = \begin{bmatrix} \mathbf{M}^F & \mathbf{M}^{FC} \\ \mathbf{M}^{CF} & \mathbf{M}^C \end{bmatrix} \quad (4.54a)$$

$$\mathbf{d} = \begin{Bmatrix} \mathbf{d}^{(1)} \\ \mathbf{d}^C \end{Bmatrix} \quad (4.54b)$$

$$\mathbf{K} = \begin{bmatrix} \mathbf{K}^F & \mathbf{K}^{FC} \\ \mathbf{K}^{CF} & \mathbf{K}^C \end{bmatrix} \quad (4.54c)$$

$$\mathbf{F} = \begin{Bmatrix} \mathbf{F}^{(1)} \\ \mathbf{F}^C \end{Bmatrix} \quad (4.54d)$$

so that it can be written in a compact monolithic form:

$$\mathbf{M}\ddot{\mathbf{d}} + \mathbf{K}\mathbf{d} = \mathbf{F} \quad (4.55)$$

The assembled matrices are of the following form:

$$\left(\mathbf{d}_{e_i}^{(1)}\right)^T = \bigoplus_{I=1}^{\hat{N}_e} \mathbf{d}_I^{(1)} = \left[\mathbf{d}_1^{(1)} \quad \dots \mathbf{d}_I^{(1)} \dots \quad \mathbf{d}_{\hat{N}_e}^{(1)} \right]_{e_i} \quad (4.56a)$$

$$\left(\mathbf{d}^{(1)}\right)^T = \bigoplus_{i=1}^{n_{el}} \mathbf{d}_{e_i}^{(1)} = \left\{ \left[\mathbf{d}_{e_1}^{(1)} \quad \dots \mathbf{d}_{e_i}^{(1)} \dots \quad \mathbf{d}_{e_{n_{el}}}^{(1)} \right] \right\}^T \quad (4.56b)$$

$$\left(\mathbf{d}^C\right)^T = \bigoplus_{e=1}^{n_{el}} \mathbf{d}^C = \left\{ \left[\mathbf{d}_1^C \quad \dots \mathbf{d}_e^C \dots \quad \mathbf{d}_{n_{el}}^C \right] \right\}^T \quad (4.56c)$$

$$\mathbf{M}^C = \bigoplus_{e=1}^{n_{el}} \mathbf{M}_e^C; \quad \mathbf{K}^C = \bigoplus_{e=1}^{n_{el}} \mathbf{K}_e^C \quad (4.57)$$

$\mathbf{M}_e^C, \mathbf{K}_e^C$ from (4.17).

$$\mathbf{M}^F = \bigoplus_{i=1}^{n_{el}} \mathbf{M}_{e_i}^F = \begin{bmatrix} \mathbf{M}_{e_1}^F & \mathbf{O}_{F\hat{N}_e} & \dots & \mathbf{O}_{F\hat{N}_e} \\ \mathbf{O}_{F\hat{N}_e} & \mathbf{M}_{e_2}^F & \dots & \mathbf{O}_{F\hat{N}_e} \\ \vdots & \vdots & \ddots & \vdots \\ \mathbf{O}_{F\hat{N}_e} & \mathbf{O}_{F\hat{N}_e} & \dots & \mathbf{M}_{e_{n_{el}}}^F \end{bmatrix} \quad (4.58a)$$

$$\mathbf{M}_{e_i}^F = \bigoplus_{I=1}^{\hat{N}_e} \mathbf{M}_I^F = \begin{bmatrix} \mathbf{M}_1^F & \mathbf{O}_F & \dots & \mathbf{O}_F \\ \mathbf{O}_F & \mathbf{M}_2^F & \dots & \mathbf{O}_F \\ \vdots & \vdots & \ddots & \vdots \\ \mathbf{O}_F & \mathbf{O}_F & \dots & \mathbf{M}_{\hat{N}_e}^F \end{bmatrix} \quad (4.58b)$$

$$\mathbf{K}^F = \bigoplus_{i=1}^{n_{el}} \mathbf{K}_{e_i}^F = \begin{bmatrix} \mathbf{K}_{e_1}^F & \mathbf{O}_{F\hat{N}_e} & \dots & \mathbf{O}_{F\hat{N}_e} \\ \mathbf{O}_{F\hat{N}_e} & \mathbf{K}_{e_2}^F & \dots & \mathbf{O}_{F\hat{N}_e} \\ \vdots & \vdots & \ddots & \vdots \\ \mathbf{O}_{F\hat{N}_e} & \mathbf{O}_{F\hat{N}_e} & \dots & \mathbf{K}_{e_{n_{el}}}^F \end{bmatrix} \quad (4.58c)$$

$$\mathbf{K}_{e_i}^F = \mathbb{D}_{I=1}^{\hat{N}_e} \mathbf{M}_I^F = \begin{bmatrix} \mathbf{K}_1^F & \mathbf{O}_F & \cdots & \mathbf{O}_F \\ \mathbf{O}_F & \mathbf{K}_2^F & \cdots & \mathbf{O}_F \\ \vdots & \vdots & \ddots & \vdots \\ \mathbf{O}_F & \mathbf{O}_F & \cdots & \mathbf{K}_{\hat{N}_e}^F \end{bmatrix} \quad (4.58d)$$

$$\mathbf{M}^{CF} = \mathbb{A}_{e=1}^{n_{el}} \mathbf{M}_e^{CF} \quad (4.58e)$$

$$\mathbf{M}_e^{CF} = \begin{bmatrix} \hat{\omega}_1 \mathbf{M}_1^{CF} & \hat{\omega}_2 \mathbf{M}_2^{CF} & \cdots & \hat{\omega}_{\hat{N}_e} \mathbf{M}_{\hat{N}_e}^{CF} \end{bmatrix} \quad (4.58f)$$

$$\mathbf{K}^{CF} = \mathbb{A}_{e=1}^{n_{el}} \mathbf{K}_e^{CF} \quad (4.58g)$$

$$\mathbf{K}_e^{CF} = \begin{bmatrix} \hat{\omega}_1 \mathbf{K}_1^{CF} & \hat{\omega}_2 \mathbf{K}_2^{CF} & \cdots & \hat{\omega}_{\hat{N}_e} \mathbf{K}_{\hat{N}_e}^{CF} \end{bmatrix} \quad (4.58h)$$

where, operator \mathbb{D} constructs block diagonal matrices, and operator \mathbb{A} assembles over the coarse-scale and unit cell DOFs.

Similarly for the coupling matrices $\mathbf{M}^{FC}, \mathbf{K}^{FC}$

$$\mathbf{M}^{FC} = \mathbb{A}_{e=1}^{n_{el}} \mathbf{M}_e^{FC} \quad (4.59a)$$

$$\mathbf{M}_e^{FC} = \begin{bmatrix} \mathbf{M}_1^{FC} \\ \mathbf{M}_2^{FC} \\ \cdots \\ \mathbf{M}_{\hat{N}_e}^{FC} \end{bmatrix} \quad (4.59b)$$

$$\mathbf{K}^{FC} = \mathbb{A}_{e=1}^{n_{el}} \mathbf{K}_e^{FC} \quad (4.59c)$$

$$\mathbf{K}_e^{FC} = \begin{bmatrix} \mathbf{K}_1^{FC} \\ \mathbf{K}_2^{FC} \\ \cdots \\ \mathbf{K}_{\hat{N}_e}^{FC} \end{bmatrix} \quad (4.59d)$$

Remark: It is emphasized that fine-scale matrices $\mathbf{M}_I^F, \mathbf{K}_I^F$ are decoupled to each other. So do fine-scale displacements, which are coupled only to the coarse-scale displacements of the coarse-scale element they belong to. However, coupling matrices $\mathbf{M}_I^{FC}, \mathbf{K}_I^{FC}, \mathbf{M}_I^{CF}, \mathbf{K}_I^{CF}$ of different unit cells are coupled to each other through the common coarse-scale nodes.

This page intentionally left blank.

Chapter 5

Conclusion

5.1 Scope and contribution of the thesis

In this section the contribution and findings of the thesis with respect to (a) the nonlocal quadrature scheme for unstructured finite element meshes and (b) the computational aspects of the dispersive computational continua, are summarized.

(a) **NLQS for unstructured finite element meshes:**

The computational continua (C^2) framework has been generalized to unstructured meshes and demonstrated in two-dimensional linear elasticity problems on several meshes and microstructures. The two main contributions towards this direction are the development of the exact nonlocal quadrature for distorted elements, which matches the two-dimensional monomials of the element, and an approximate tensor-product based nonlocal quadrature that eliminates the need for costly evaluation of the quadrature points for each element. A few key observations can be made based on the performance of the two nonlocal quadrature schemes:

- i. The error in the *overall behavior*, as measured by two different measures (see Section 3.7.1), suggests that the C^2 formulations with either nonlocal quadrature offer 10-20(%)

improvement in the accuracy over the classical $O(1)$ homogenization. This accuracy gain is smaller than in structured meshes [51] where improvement in global measures was noticeably larger.

- ii. The gain in accuracy of local stresses in the unit cells positioned in critical locations is substantial than in the global measures (see Section 3.7.2). This is consistent with the previous observation since the regions of high coarse-scale gradients are limited to relatively small coarse-scale domains.
- iii. The performance of the tensor-product based approximate quadrature was comparable to that of the computationally costly exact nonlocal quadrature in terms of both the global and local error measures making it more attractive.

(b) Dispersive C^2 and wave propagation:

The formulation of the dispersive computational continua has been presented starting with the strong form, followed by the weak form and the discretization in space and time. The resulting algebraic system of equations has a sparse block structure where each unit cell matrix block is coupled to a single coarse-scale element it is positioned in. The unit cell matrix blocks can be statically condensed out to form an algebraic system of equations for the coarse-scale system of equations only. The overhead associated with the static condensation is insignificant compared to the overall computational cost for short load durations. Thus, for short load durations, such as shocks, the computational cost of the methods is comparable to the classical dispersive methods, while offering considerable accuracy gains if the wavelength of propagating signal is comparable to the characteristic size of the microstructure.

5.2 Future Work

In this section the future work within the framework of computational continua is discussed.

I. Unit cell boundary conditions and boundary constraints:

The appropriate boundary conditions on the unit cell problem is still an open issue of research. For the C^2 formulation employed in the present thesis, the boundary of the unit cell domain is subjected to periodicity conditions and additional constraints in a weak form as a result of the approximation of the total stress field by a bilinear form.

For finite size unit cells located in the critical areas of high coarse-scale strain gradients, it is reasonable to consider loosening or even eliminating the periodicity and boundary constraints. One approach to do that is to employ the technique of embedded unit cell domain (EUC) [32], according to which a primary unit cell is considered to be surrounded by complementary unit cells. The periodicity and boundary constraints used in the present thesis can then be applied on the boundary of the extended domain (exterior boundaries of the complementary unit cells). The solution of this extended unit cell problem provides the correct boundary conditions to be applied on the boundary of the primary unit cell.

II. **Numerical analysis:** A numerical analysis of the computational continua formulation within the functional analysis framework would allow to investigate the accuracy, convergence and stability of the method with respect to the number of nonlocal quadrature points, the order of the elements used in the coarse-scale and unit cell domains, the number of coarse-scale and unit cell elements, and also the boundary constraints on the unit cell problem.

III. **Nonlocal quadrature scheme:** In the present thesis the nonlocal quadrature schemes for quadrilateral Q8 and triangular T6 elements were developed requiring the minimum number

of nonlocal quadrature points. The method was demonstrated using Q8 quadrilateral elements. However, other types of elements are also preferred in the engineering practice, such as tetrahedrals and hexahedrals or higher-order elements in both 2D and 3D. As a future work, the derivation of nonlocal quadrature scheme with more than the minimum required points (3x3 for Q8 elements, 3x3x3 for hexahedrals, etc.) and a convergence and accuracy analysis would be of interest.

IV. Dispersive computational continua: The dispersion analysis and numerical investigation presented in [19, 21] has been limited to the one-dimensional domain. The results in [19, 21] were amazingly accurate with respect to the dispersion curve and the wave propagation behavior. An investigation of the dispersive behavior of the C^2 formulation in higher dimensions would be of a greater practical interest. Moreover, exploration of other time-integration schemes using split operators or different time-stepping between the two coupled transient-transient problems (the coarse-scale and the unit cell) would enhance the computational efficiency of the method.

V. Other applications: All the aforementioned theoretical and numerical explorations of the C^2 formulation could be demonstrated in a diverse spectrum of applications including functionally graded materials, nonlinear inelastic materials, propagation of shear bands, fracture mechanics, etc.

Bibliography

- [1] A. ABDULLE, W. E. B. ENGQUIST, AND E. VANDEN-EIJNDEN, *The heterogeneous multiscale method*, Acta Numerica, 21 (2012), pp. 1–87.
- [2] A. ABDULLE, M. GROTE, AND C. STOHRER, *Finite element heterogeneous multiscale method for the wave equation: Long-time effects*, Multiscale Modeling and Simulation, 12 (2014), pp. 1230–1257.
- [3] J. D. ACHENBACH AND G. HERRMANN, *Wave motion in solids with lamellar structuring*, ASME-Dynamics of Structured Solids, (1968), pp. 23–46.
- [4] I. ANDRIANOV, V. BOLSHAKOV, V. DANISHEVS' KYY, AND D. WEICHERT, *Higher order asymptotic homogenization and wave propagation in periodic composite materials*, Proceedings of the Royal Society A: Mathematical, Physical and Engineering Sciences, 464 (2008), pp. 1181–1201.
- [5] J.-L. AURIAULT AND C. BOUTIN, *Long wavelength inner-resonance cut-off frequencies in elastic composite materials*, International Journal of Solids and Structures, 49 (2012), pp. 3269–3281.
- [6] J.-L. AURIAULT, C. BOUTIN, AND C. GEINDREAU, *Homogenization of Coupled Phenomena in Heterogenous Media*, Wiley-ISTE, 2009.
- [7] A. BEDFORD AND M. STERN, *On wave propagation in fiber-reinforced viscoelastic materials*, Journal of Applied Mechanics, Transactions ASME, 37 Ser E (1970), pp. 1190–1192.
- [8] W. CHEN AND J. FISH, *A generalized space-time mathematical homogenization theory for bridging atomistic and continuum scales*, International Journal for Numerical Methods in Engineering, 67 (2006), pp. 253–271.
- [9] ———, *A mathematical homogenization perspective of virial stress*, International Journal for Numerical Methods in Engineering, 67 (2006), pp. 189–207.
- [10] R. CLAUSIUS, *On a mechanical theorem applicable to heat*, Philosophical Magazine, (1870), pp. 122–127.
- [11] E. COSSERAT AND F. COSSERAT, *Sur la mecanique generale*, Comptes Rendus de l'Académie des Sciences Paris, 145 (1907), p. 1139.
- [12] R. CRASTER, J. KAPLUNOV, AND A. PICHUGIN, *High-frequency homogenization for periodic media*, Proceedings of the Royal Society A: Mathematical, Physical and Engineering Sciences, 466 (2010), pp. 2341–2362.
- [13] R. CRASTER, J. KAPLUNOV, AND J. POSTNOVA, *High-frequency asymptotics, homogenisation and localisation for lattices*, Quarterly Journal of Mechanics and Applied Mathematics, 63 (2010), pp. 497–519.
- [14] Y. DING, Z. LIU, C. QIU, AND J. SHI, *Metamaterial with simultaneously negative bulk modulus and mass density*, Physical Review Letters, 99 (2007).
- [15] Y. E. EFENDIEV, J. C. GALVIS, AND T. HOU, *Generalized multiscale finite element methods (gmsfem)*, Journal of Computational Physics, 251 (2013), pp. 116–135.
- [16] A. C. ERINGEN, *Mechanics of Micromorphic Continua*, Springer Berlin Heidelberg, 1968, pp. 18–35.
- [17] J. A. EVANS, T. J. HUGHES, AND G. SANGALLI, *Enforcement of constraints and maximum principles in the*

BIBLIOGRAPHY

- variational multiscale method*, Computer Methods in Applied Mechanics and Engineering, 199 (2009), pp. 61 – 76.
- [18] D. FAFALIS, S. FILOPOULOS, AND G. TSAMASPHYROS, *On the capability of generalized continuum theories to capture dispersion characteristics at the atomic scale*, European Journal of Mechanics - A/Solids, 36 (2012), pp. 25 – 37.
- [19] D. FAFALIS AND J. FISH, *Computational aspects of dispersive computational continua for elastic heterogeneous media*, Computational Mechanics, 56 (2015), pp. 931–946.
- [20] ———, *Computational continua for linear elastic heterogeneous solids on unstructured finite element meshes*, to appear in the International Journal for Numerical Methods in Engineering, (2017).
- [21] V. FILONOVA, D. FAFALIS, AND J. FISH, *Dispersive computational continua*, Computer Methods in Applied Mechanics and Engineering, 298 (2016), pp. 58–79. cited By 3.
- [22] J. FISH, *The s-version of the finite element method*, Computers and Structures, 43 (1992), pp. 539 – 547.
- [23] J. FISH, *Practical Multiscaling*, Wiley, 2013.
- [24] J. FISH AND W. CHEN, *Higher-order homogenization of initial/boundary-value problem*, Journal of Engineering Mechanics, 127 (2001), pp. 1223–1230.
- [25] J. FISH, W. CHEN, AND R. LI, *Generalized mathematical homogenization of atomistic media at finite temperatures in three dimensions*, Computer Methods in Applied Mechanics and Engineering, 196 (2007), pp. 908–922.
- [26] J. FISH, V. FILONOVA, AND D. FAFALIS, *Computational continua revisited*, International Journal for Numerical Methods in Engineering, DOI: 10.1002/nme.4793 (2014).
- [27] J. FISH, V. FILONOVA, AND S. KUZNETSOV, *Micro-inertia effects in nonlinear heterogeneous media*, International Journal for Numerical Methods in Engineering, 91 (2012), pp. 1406–1426.
- [28] J. FISH AND S. KUZNETSOV, *Computational continua*, International Journal for Numerical Methods in Engineering, 84 (2010), pp. 774–802.
- [29] J. FISH, A. LI, AND F. YAVARI, *Adaptive generalized mathematical homogenization framework for nanostructured materials*, International Journal for Numerical Methods in Engineering, 83 (2010), pp. 1133–1154.
- [30] M. GEERS, V. G. KOUZNETSOVA, AND W. A. M. BREKELMANS, *Multiscale first-order and second-order computational homogenization of microstructures towards continua*, International Journal for Multiscale Computational Engineering, 1 (2003).
- [31] P. GERMAIN, *The method of virtual power in continuum mechanics. part 2: Microstructure*, SIAM Journal on Applied Mathematics, 25 (1973), pp. 556–575.
- [32] M. GRIGOROVITCH AND E. GAL, *Homogenization of non-periodic zones in periodic domains using the embedded unit cell approach*, Computers and Structures, 179 (2017), pp. 95 – 108.
- [33] G. HEGEMIER, *Mixture theories with microstructure for wave propagation and diffusion in composite materials.*, Solid Mech Arch, 3 (1978), pp. 33–71.
- [34] T. HOU AND X.-H. WU, *A multiscale finite element method for elliptic problems in composite materials and porous media*, Journal of Computational Physics, 134 (1997), pp. 169–189.
- [35] T. HUGHES, G. FEIJÓO, L. MAZZEI, AND J.-B. QUINCY, *The variational multiscale method - a paradigm for computational mechanics*, Computer Methods in Applied Mechanics and Engineering, 166 (1998), pp. 3–24.
- [36] T. J. R. HUGHES, *The Finite Element Method: Linear Static and Dynamic Finite Element Analysis*, vol. - of Dover Civil and Mechanical Engineering, Dover Publications, 2000.
- [37] T. HUI AND C. OSKAY, *A nonlocal homogenization model for wave dispersion in dissipative composite materials*, International Journal of Solids and Structures, 50 (2013), pp. 38–48.

- [38] ———, *A high order homogenization model for transient dynamics of heterogeneous media including micro-inertia effects*, *Computer Methods in Applied Mechanics and Engineering*, 273 (2014), pp. 181–203.
- [39] ———, *Laplace-domain, high-order homogenization for transient dynamic response of viscoelastic composites*, *International Journal for Numerical Methods in Engineering*, DOI: 10.1002/nme.4793 (2015).
- [40] S. KANAUN AND V. LEVIN, *Self-consistent methods in the problem of axial elastic shear wave propagation through fiber composites*, *Archive of Applied Mechanics*, 73 (2003), pp. 105–130.
- [41] V. KOUZNETSOVA, W. A. M. BREKELMANS, AND F. P. T. BAAIJENS, *An approach to micro-macro modeling of heterogeneous materials*, *Computational Mechanics*, 27 (2001), pp. 37–48.
- [42] A. LI, R. LI, AND J. FISH, *Generalized mathematical homogenization: From theory to practice*, *Computer Methods in Applied Mechanics and Engineering*, 197 (2008), pp. 3225–3248.
- [43] A. LI, H. WAISMAN, AND J. FISH, *A space-time multiscale method for molecular dynamics simulations of biomolecules*, *International Journal for Multiscale Computational Engineering*, 4 (2006), pp. 791–801.
- [44] Z. LIU, X. ZHANG, Y. MAO, Y. ZHU, Z. YANG, C. CHAN, AND P. SHENG, *Locally resonant sonic materials*, *Science*, 289 (2000), pp. 1734–1736.
- [45] K. MATSUI, K. TERADA, AND K. YUGE, *Two-scale finite element analysis of heterogeneous solids with periodic microstructures*, *Computers and Structures*, 82 (2004), pp. 593 – 606.
- [46] G. MAUGIN, *Nonlocal theories or gradient-type theories: A matter of convenience?*, *Archives of Mechanics*, 31 (1979), pp. 15–26.
- [47] J. C. MAXWELL, *van der waals on the continuity of the gaseous and liquid states*, *Nature*, 10 (1874), pp. 477–80.
- [48] C. C. MEI AND B. VERNESCU, *Homogenization methods for multiscale mechanics*, World Scientific, 2010.
- [49] C. MIEHE AND A. KOCH, *Computational micro-to-macro transitions of discretized microstructures undergoing small strains*, *Archive of Applied Mechanics*, 72 (2002), pp. 300–317.
- [50] R. D. MINDLIN, *Micro-structure in linear elasticity*, *Archive for Rational Mechanics and Analysis*, 16 (1964), pp. 51–78.
- [51] A. MOYEDA AND J. FISH, *Towards practical multiscale approach for analysis of reinforced concrete structures*, to appear in *Computational Mechanics*, (2017).
- [52] A. H. NAYFEH AND G. GURTMAN, *Continuum approach to the propagation of shear waves in laminated wave guides.*, ASME Pap, (1973).
- [53] S. NEMAT-NASSER AND A. SRIVASTAVA, *Overall dynamic constitutive relations of layered elastic composites*, *Journal of the Mechanics and Physics of Solids*, 59 (2011), pp. 1953–1965.
- [54] G. NITIN, S., *Practical Finite Element Analysis*, Finite To Infinite, 2008.
- [55] E. NOLDE, R. C. CRASTER, AND J. KAPLUNOV, *High frequency homogenization for structural mechanics*, *Journal of the Mechanics and Physics of Solids*, 59 (2011), pp. 651–671.
- [56] F. OTERO, S. OLLER, AND X. MARTINEZ, *Multiscale computational homogenization: Review and proposal of a new enhanced-first-order method*, *Archives of Computational Methods in Engineering*, (2016).
- [57] K. PHAM, V. KOUZNETSOVA, AND M. GEERS, *Transient computational homogenization for heterogeneous materials under dynamic excitation*, *Journal of the Mechanics and Physics of Solids*, 61 (2013), pp. 2125–2146.
- [58] F. SABINA AND J. WILLIS, *A simple self-consistent analysis of wave propagation in particulate composites*, *Wave Motion*, 10 (1988), pp. 127–142.
- [59] F. SANTOSA AND W. W. SYMES, *A dispersive effective medium for wave propagation in periodic composites*, *SIAM Journal on Applied Mathematics*, 51 (1991), pp. pp. 984–1005.

BIBLIOGRAPHY

- [60] H. WAISMAN AND J. FISH, *A space-time multilevel method for molecular dynamics simulations*, Computer Methods in Applied Mechanics and Engineering, 195 (2006), pp. 6542–6559.
- [61] E. WEINAN, B. ENGQUIST, AND Z. HUANG, *Heterogeneous multiscale method: A general methodology for multiscale modeling*, Physical Review B - Condensed Matter and Materials Physics, 67 (2003), pp. 921011–921014.
- [62] K. L. WING, *Multi-scale finite element methods for structural dynamics*, American Institute of Aeronautics and Astronautics, AIAA-91-1057-CP (1991), pp. 2510–2514.
- [63] WWW, *Altair University, Element Quality and Checks*. http://www.altairuniversity.com/wp-content/uploads/2012/04/Student_Guide_211-233.pdf. Accessed: 2017-08-17.
- [64] —, *MathWoks, MATLAB knnsearch*. http://www.mathworks.com/help/stats/knnsearch.html?searchHighlight=knnsearch&s_tid=doc_srchtittle. Accessed: 2017-08-22.
- [65] —, *MathWoks, MATLAB scatteredInterpolant*. <http://www.mathworks.com/help/matlab/ref/scatteredinterpolant-object.html;jsessionid=a41623904726e01bd8fe3352fb07#btrbne6-14>. Accessed: 2017-08-22.
- [66] T. I. ZOHDI AND P. WRIGGERS, *An Introduction to Computational Micromechanics*, vol. 20 of Lecture Notes in Applied and Computational Mechanics, Springer-Verlag Berlin Heidelberg, 2005.